UNIVERSITÄT PADERBORN
Die Universität der Informationsgesellschaft

Fakultät für Naturwissenschaften - Department Physik

Quantum Dot Emitters in Planar Photonic Crystal Nanocavities

Dem Department Physik der Universität Paderborn zur Erlangung des akademischen Grades eines Doktors der Naturwissenschaften vorgelegte

Dissertation

von **M.Sc. Mohannad Al-Hmoud**

Paderborn, September 2013

Promotionskommission

Prof. Dr. Torsten Meier (Vorsitzender)
Prof. Dr. Artur Zrenner (1. Gutachter)
Prof. Dr. Cedrik Meier (2. Gutachter)
Dr. Thomas Riedl

Datum der mündlichen Prüfung: 03. September 2013

Zusammenfassung

Quantenpunkte (QDs) sind Halbleiter-Nanostrukturen mit atomartigen optischen und halbleiterspezifischen elektronischen Eigenschaften. Die einzigartigen physikalischen Eigenschaften und potentielle Anwendungen, wie etwa in Quanteninformations und Festkörperlaseranwendungen, machen Quantenpunkte seit der vergangen 20 Jahre zum Gegenstand der Forschung. Quantenpunkte in optischen Resonatoren erfahren erhöhte Licht-Materie Wechselwirkung und eignen sich deshalb hervorragend für quantenelektrodynamische Experimente in Festkörpern. Zu den neuen Anwendungsgebieten zählen auch schwellenlose Quantenpunktlaser und Einzelphotonenquellen.

Es wurden viele Mikroresonator-Geometrien vorgeschlagen und untersucht, hierbei stellte sich heraus, dass 2D photonische Kristall-Resonatoren am Erfolg versprechendsten sind. Sie besitzen sowohl sehr hohe Q-Faktoren als auch kleine Modenvolumen im Bereich der Lichtwellenlänge $(\lambda/n)^3$ und lassen sich leicht und kompatibel mit der monolithischen on-chip Integration herstellen.

Die vorliegende Arbeit behandelt das Design, die Herstellung und Charakterisierung photonischer Kristall-Resonatoren mit eingebetteten InGaAs QDs. Der Schwerpunkt liegt auf der Untersuchung der H2 Kavität, die durch Entfernen von sieben Löchern im Zentrum eines hexagonalen 2D photonischen Kristalls gebildet wird. Zusätzlich wurden andere Resonatortypen, wie H1, L3 und L5 behandelt. Zur Optimierung der Güte und Berechnung der Modenverteilung wurde die Finite-Differenzen-Methode im Zeitbereich (FDTD) angewandt. Es konnte bestätigt werden, dass geschicktes Verzerren der Kristallstruktur um den Resonatrodefekt den Q-Faktor sehr stark erhöhen kann.

Die QD-Proben wurden mit Molekularstrahlepitaxie gewachsen. Anschließend wurden photonische Kristalle mit Hilfe von Elektronenstrahllithografie und reaktivem Ionenätzen hergestellt. Der Fertigungsprozess wurde für GaAs photonische Kristall-Resonatoren hoher Qualität entwickelt und optimiert.

Die Proben wurden mit der Photolumineszenz Methode bei kryogenen Temperaturen charakterisiert. Mit Hilfe polarisationsabhängiger Messungen konnten Resonatormoden anhand der Simulation identifiziert werden. Die experimentellen und theoretischen Ergebnisse stimmen gut überein. Abschließend wurden p-Schalen Rabi-Oszillationen am Quantenpunkt im photonischen Kristall-Resonator untersucht.

Abstract

Semiconductor nanostructures, known as *quantum dots*, have been extensively investigated in the last two decades due to their interesting electronic and optical properties. The importance of these systems comes from not only their exciting physics, but also the potential applications in interdisciplinary fields like quantum information processing and solid-state lasers. Incorporation of quantum dots in optical cavities enhances light-matter interaction, and therefore allows for cavity quantum electrodynamics experiments in solid-state systems. It will also possibly lead to new applications as thresholdless lasers and quantum information devices.

So far, many types of cavities have been introduced. Among them, 2D photonic crystal cavities are considered to be the most promising systems. They support high quality factor and very small mode volume, i.e., comparable with the wavelength of light $(\lambda/n)^3$. Moreover, owing to their planar nature, they are easy to fabricate and compatible for monolithic on-chip integration.

This thesis discusses the design, fabrication, and characterization of photonic crystal cavities with embedded InGaAs quantum dots. Cavities with different geometries are investigated, including H1, H2, L3 and L5. The main focus is on H2 type, consisting of a defect formed by omitting seven air holes in the center of a triangular lattice. The design and simulation of the cavities are performed by using the Finite-Difference Time-Domain method. It is found that by engineering the air holes surrounding the cavity, the quality factor can be increased significantly by the gentle mode confinement method.

The quantum dot samples are grown by using molecular beam epitaxy technique. Then, the photonic crystals are produced by using electron beam lithography and etching techniques. The fabrication process is developed and optimized in order to obtain high quality GaAs photonic crystal membranes.

The cavities are characterized by using photoluminescence technique at low temperature. Polarization-dependent measurements are also performed in order to identify the cavity modes. The results are in good agreement with our theoretical calculations. Finally, the p-shell Rabi oscillations of a single quantum dot in a modified H2 photonic crystal cavity are investigated.

Contents

Chapter 1

Introduction

The interest in the study of the physical properties of low-imensional semiconductor structures is driven by their unusual properties that are promising for applications in interdisciplinary fields. In the beginning of 1970s, the progress in the semiconductor technology allowed the production of semiconductor heterostructures, known as *quantum wells* (QWs) [1]. In such structures, the charge carriers are confined in a two-dimensional plane. The confinement results in new fundamental effects, for example the discovery of the integer quantum Hall effect [2]. Nowadays, QWs are widely used in many optoelectronic devices, like diode lasers and infrared photodetectors.

By shrinking the size of crystalline semiconductor in all three dimensions, the charge carriers are completely confined, and we obtain the so-called *quantum dots* (QDs). The most prominent technique for fabricating these systems is self-assembled epitaxial growth. The complete confinement leads to the characteristic δ-like density of states, making QDs interesting from both a basic physics and an application point of view. For fundamental research, QDs are attractive systems since they allow investigation of few-particle interactions. Concerning the application, QDs have been proposed for many applications, like QD-based lasers [3], single photon emitters [4, 5], and quantum information processing, including quantum computing [6], quantum cryptography [7], and quantum teleportation [8].

Owing to the high refractive index of the host material surrounding the QDs, the light extraction efficiency is very low. This in not advantageous because for many applications, like in lasers and single photon emitters, high extraction efficiency is needed. Fortunately, the extraction efficiency can be enhanced by embedding QDs in photonic nanowires [9] or in optical cavities [10] like micropillars [11, 12], microdisks [4], and 2D photonic crystals (PhCs) [13, 14]. Among optical cavities, 2D PhCs are considered as the most attractive systems since they offer very small

mode volumes (V_m) and high quality factors (Q). Moreover, their planar feature enables the fabrication by utilizing the well-established fabrication processes, and make them compatible for monolithic on-chip integration [15–17]. In addition, metal pads can be easily introduced in PhCs for electrical control [18, 19].

Photonic crystals [20–24] are systems in which the dielectric constant is modulated periodically on a length scale of the optical wavelength, resulting in a photonic band gap. The cavity in such systems is formed by perturbing the periodicity of the dielectric material.

The quality factor of PhC cavities can be significantly improved by properly designing the neighborhood of the cavity without inducing a meaningful increase in the mode volume. Consequently, the ratio of Q/V is enhanced [25–31]. In addition to their importance in potential applications, PhC cavities with embedded QDs have allowed the observation of cavity quantum electrodynamics effects in solid-state systems, like the Purcell effect in the weak coupling regime [13] and vacuum Rabi splitting in strong coupling regime [32].

In this thesis, different types of photonic crystal nanocavities with embedded InGaAs quantum dots are investigated. Chapter 2 provides a general overview of quantum dots and the effect of embedding them in optical cavities. The basics of photonic crystal cavities are introduced in Chapter 3. In Chapter 4, the fabrication process of photonic crystal membrane structures is described. Chapter 5 includes the experimental setup used for optical characterization in this work. Chapter 6 is devoted to the discussion of H2 cavity design, improvement of Q-factor and characterization. The simulations for the photonic crystal cavities are performed by using the Finite-Difference Time-Domain method, while photoluminescence technique is used for the characterization. Chapter 7 investigates the p-shell Rabi oscillations of a QD exciton in photonic crystal cavity, where the s-shell is near to resonance with a cavity mode. Finally, Chapter 8 concludes the content of this work and presents an outlook for possible future work.

Chapter 2

Semiconductor Quantum Dots: An Overview

2.1 Introduction

Semiconductor *quantum dots* (QDs) [33–36] are nanostructures which confine charge carriers in all three directions. This confinement results in discrete energy levels, similar to those of single atoms. Therefore QDs are frequently referred to as artificial atoms. Typically, the dimensions of the QDs range from a few to tens of nanometers. QDs are typically based on the use of direct bandgap materials, where the generated electrons and holes are both confined within the dot, like InGaAs/GaAs QDs. This kind of dots is known as type-I QDs. In type-II QDs, either the electron or the hole is confined in the dot, while the other carrier remains in the barrier, like InP/GaAs QDs. In this type, usually the electrons are located in the matrix near the interface to the QD, while the holes are confined in the dot.

In the last three decades many types of QDs have already been developed. The first and the most straightforward method to produce quantum dots was reported by Reed *et al.* [37] in 1986. In this method, electron beam lithography technique was used to define nano-patterns on a quantum well structure followed by reactive ion etching. The advantage of this method is the ability to produce QDs with predefined positions and dimensions. This ability is crucial for QDs device applications. The main disadvantage in the QDs prepared by this method is the relatively small photoluminescence yield. This is due to non-radiative recombination centers introduced in the dot structure during the fabrication process.

Currently, there are various methods to produce QDs such as naturally formed quantum dots [38], colloidal nanocrystals [39], electrically gated QDs [40], and self-assembled quantum dots [41–43]. The latter is considered as the most promising

for technological applications due to the quasi-perfect crystal structure of the obtained QDs and their excellent optical activities. Figure 2.1 shows images of different QD systems. As only self-assembled QDs have been investigated in this thesis, this chapter includes the properties of this type.

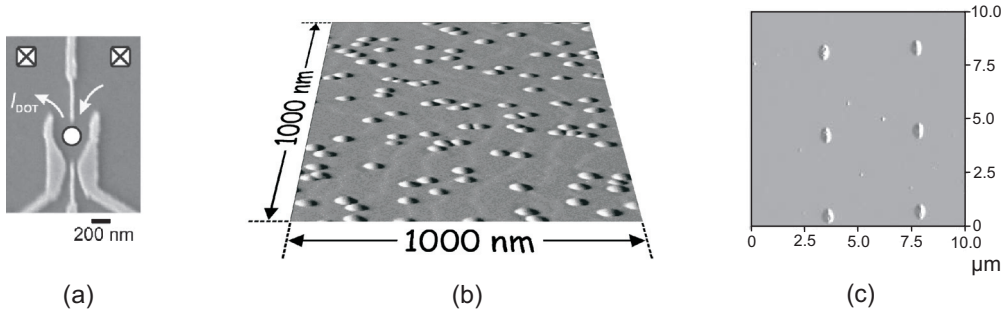

FIGURE 2.1: (a) SEM image of a gate defined QD [40]. (b) AFM micrograph of self-assembled QDs [44]. (c) AFM micrograph of QDs grown epitaxially on a pre-patterned substrate [45].

2.2 Growth of Self-Assembled Quantum Dots

In self-assembled QDs (SAQDs), the dots are formed during Stranski-Krastanov (SK) growth mode [46] of a material on a crystalline substrate. When growing SAQDs, one has to consider the following. The material from which QDs will be produced must have a band gap smaller than that of the host material, while the lattice constant has to be larger.[1] The material deposition is achieved by one of the epitaxial growth techniques, such as molecular beam epitaxy (MBE) or metal-organic chemical vapor deposition (MOCVD).[2] For research intentions, MBE is normally used owing to its flexibility. On the other hand, the MOCVD technique is favored for production purposes due to its faster growth process and the ability to grow uniform films over large substrate areas.

Initially, the lattice constant of the deposited material changes to accommodate to the lattice of the substrate. This introduces a strain in the deposited layer, known also as the *wetting layer*. With increasing the layer thickness, the strain energy increases until a critical thickness is reached, then it becomes favorable to relax the strain by forming three dimensional islands, i.e., quantum dots. Later, the dots are overgrown by the host material to passivate their surfaces and ensure optimal electronic and optical properties. Figure 2.1(b) shows a typical atomic

[1] Usually, the lattice mismatch is a few percent. For example, it is about 7% for InAs/GaAs and 3% for InGaAs/GaAs

[2] In this thesis, the QDs are grown by MBE.

force microscope (AFM) image of self-assembled InGaAs/GaAs QDs grown by MBE technique.

Typical InGaAs dots grown on GaAs via SK growth mode have lateral width of about 25 nm, height of a few nm, and density of $1 \times 10^9 - 1 \times 10^{11}$ per cm^2. The size and density of dots can be controlled by controlling the growth conditions. The most crucial growth parameters are the temperature of the substrate, the layer thickness, the material deposition rate, and the composition. Depending on the growth conditions, SAQDs can be grown into different geometries like pyramids [47], disks [48] and lens-shape [49]. The latter is the most commonly grown geometry.

The small size and high density of the SAQDs, aside from the perfect crystal structure, are the main useful characters of this type of nanostructures. An important advantage of this method is the ease of fabrication, since the growth of the dots is a natural process with no need for additional processing like lithography. The main disadvantages of SAQDs are the inherent fluctuation in the QD size and the random distribution of the dots.

The former results in emission at different energies, and consequently in what is called *inhomogeneous line broadening*. Hence, the full width at half maximum (FWHM) of the photoluminescence spectrum of a QD ensemble gives an indication about the homogeneity of the dots. The more homogeneous the size, the narrower the FWHM. The non-uniformity in the dot size is an unavoidable issue. It is only weakly dependent on the fabrication method of QDs. For a typical SAQD ensemble, the inhomogeneous broadening linewidth is 10-100 meV.

Concerning the random spatial distribution, which is crucial for QD-device applications, various attempts have been devoted to achieve site control of SAQDs. An epitaxial growth on a pre-patterned substrate surface has been shown to be the most promising (see Fig. 2.1(c)) [45]. Another approach is to use a focused ion beam (FIB) to define shallow holes on a substrate followed by epitaxial growth of the dot material [50]. Details of these methods are beyond the scope of this thesis, therefore they will not be discussed here.

2.3 Quantum Confinement

In bulk semiconductor crystals, the charge carriers move freely in all three directions. Their de Broglie wavelength (λ_{de}) is given by

$$\lambda_{de} = h/\sqrt{3m^*_{e,h}k_BT}, \tag{2.1}$$

where h and k_B are the Planck's and Boltzmann's constants, $m^*_{e,h}$ is the effective mass of the charge carriers, and T is the absolute temperature. If one or more of the dimensions of semiconductor crystal is limited to a length scale of the order or less than λ_{de}, the motion in that direction will be quantized. This phenomenon is known as the *quantum confinement*. A one dimensional confinement potential produces quantum well (QW), while quantum wire (QWR) is achieved by two dimensional confinement. The confinement in all directions results in the formation of QDs.

From equation (2.1), it is clear that quantum confinement depends on the effective mass of the charge carriers and temperature. Usually, m^*_e is much smaller than the free electron mass m_e. For example, it is 0.06 m_e in GaAs. Thus, the required length scale to observe quantum confinement effects at room temperature is about 10 nm. Usually, spectroscopic measurements on QDs are performed at low temperature (several K) to avoid the thermal excitation of electrons. At low temperature, the quantization can be observed for a larger length scale (up to 100 nm).

As a consequence of the quantum confinement, the density of states (DOS) is affected to a great extent, as illustrated in Fig. 2.2. The DOS for bulk semiconductor is proportional to $\sqrt{E}$, while it is a step function for QW, and proportional to $1/\sqrt{E}$ for QWR. For QDs, the DOS consists of a series of δ-functions, like those for atoms. This is one of the most attracting peculiarities of QDs. Owing to the discrete nature of the DOS, lasers based on QDs [51] are expected to have weaker temperature dependence in comparison to QW lasers.

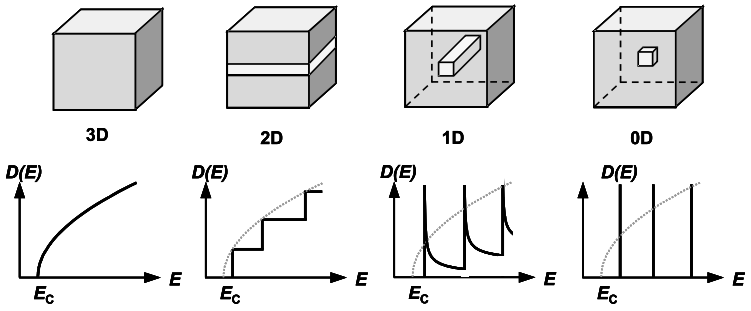

FIGURE 2.2: Schematic representations (top) and density of states in the conduction band (bottom) for semiconductor bulk (3D), quantum well (2D), quantum wire (1D), and quantum dot (0D). After [34].

2.4 Energy States in Self-Assembled Quantum Dots

Along with the advances in the growth of SAQDs, last decades have witnessed development of sophisticated techniques that allow for measurement of the optical and electronic transport properties of these QDs. To understand the physics and to explain the experimental observations in terms of the underlying energy states of the QDs, theoretical models are needed. An exact theoretical calculation of the energy states in SAQDs is a challenge, because slight variations in QD geometry and confinement potential strongly affect these states. Even for the same geometry, the small fluctuations in size and composition affect the confinement potential. So, all of spectroscopic investigations of single QDs suffer from exact comparison with the real parameters. Fortunately, various models succeeded in obtaining results that are in a good agreement with the experimental measurements. As discussed in Section 2.2, SAQDs can be grown in different geometries like pyramids, disks and lens-shape. Only the latter will be discussed here as it is the most common geometry and the only one investigated in this work.

In lens-shaped SAQDs the height in the growth direction z is significantly smaller than the lateral dimension xy, thus the confinement in the z direction is much stronger. Consequently, the quantization energies in z direction are large enough so that only the lowest subband (ground state) needs to be considered, while higher subband (excited states) can be neglected. On the other hand, the lateral confinement of the charge carriers in the in-plane (xy) is much weaker and determines the shell structure of the dot. Thus, SAQDs can be considered as quasi two dimensional systems. It was found that energy states in SAQDs can be understood by considering an effective parabolic potential in the in-plane and a box-like along the growth direction [52, 53].

Considering a general case, with an external magnetic field B applied normal to the plane of the dot, the single-particle levels for electrons correspond to the levels of two-dimensional harmonic oscillators [53][3]:

$$E^e_{mn} = \hbar\left[\Omega^e_+(n+1/2) + \Omega^e_-(m+1/2)\right], \tag{2.2}$$

where m and n are the quantum numbers of the two harmonic oscillators representing the corresponding eigenstates $|mn\rangle$. The frequencies of the oscillators

[3] Here, the potential in the xy plane is assumed to be symmetric, while in reality it is not. This asymmetry leads to the fine structure splitting in the energy levels and equation (2.2) can be written as [54]: $E_{n_x,n_y}(\delta) = \hbar\omega\left[(n+1/2)\sqrt{\delta} + (m+1/2)/\sqrt{\delta}\right]$, where the ratio $\delta = \omega_x/\omega_y$ defines the asymmetry of the lateral confinement potential.

are given by $\Omega^e_{+/-} = (\sqrt{\omega_c^2 + 4\omega_o^2} \pm \omega_c)/2$, where $\omega_c = eB/(m^*c)$ is the cyclotron frequency, B is the external magnetic field, c is the speed of light, m^* and e are the effective mass and the charge of an electron, respectively. In the absence of a magnetic field, where $\Omega^e_+ = \Omega^e_- = \omega_o$ is valid, the energy levels are $2(N+1)$-fold degenerate[4], with the principal quantum number $N = n+m = 0, 1, 2, \ldots$. The factor 2 comes from the spin degeneracy. Thus, fully occupied shells can be reached for occupancies of $2, 6, 12, 20, \ldots$, where the s-shell is filled with two electrons (spin up and spin down), p-shell with four electrons, and so on.

Similarly, the energy levels of the holes can be obtained by replacing the electron frequencies Ω^e_+ with the hole frequencies Ω^h_+ (ignoring the semiconductor gap) in equation (2.2). The angular momentum is given by: $L_{mn} = \pm(m-n)$, where the plus and minus signs are for electrons and holes, respectively. In analogy to atomic physics, levels with total angular momentum $L = |m-n| = 0, 1, 2, \ldots$ are labeled as s, p, d, ... shells, respectively. The optical interband transitions are allowed only for electrons and holes with the same quantum numbers n and m, as illustrated in Fig. 2.3.

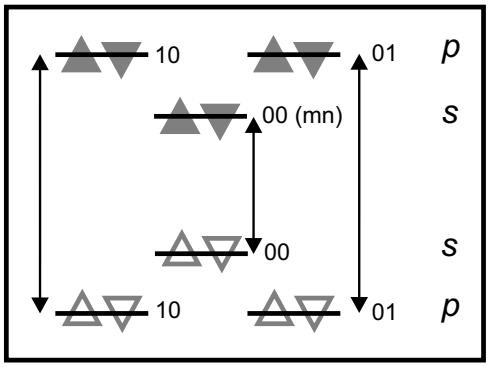

FIGURE 2.3: Scheme of the s- and p-shell in a QD. The vertical arrows indicate the allowed interband transitions.

2.5 Few Particle States in Self-assembled Quantum Dots

As discussed in the last section, QDs have energy levels (shells) analogous to real atoms. Depending on the given confinement potential, different numbers of shells are observable in the QD. In all InGaAs/GaAs QD samples studied in this work, the confinement potential is weak due to the relatively low band gap offset between

[4] For a strong magnetic field ($\omega_c >> \omega_o$), the degeneracy breaks and the energy levels are separated by the cyclotron energy $\hbar\omega_c \approx \hbar\Omega^e_+$.

the QD and host material. Thus, usually only s- and p-shell are present. Owing to the compressive strain in the dot structure of SAQDs, the heavy and light holes (HH and LH) are splitted at the Γ-point ($k = 0$) by several tens of meV. Thus, only HH states are relevant for the lowest energy levels of a QD, while LH states lie in the continuum and can be neglected within the scope of this work.

Normally, QDs are unoccupied (empty) at low temperature, i.e., there are no electrons in the conduction band shells. Charge carriers can be generated in the dot for example by photoinduced process or by charge injection.

The most basic occupancy is the ground state exciton (X).[5] It is the lowest possible energy state formed by an electron-hole pair in the s-shell of the conduction and valence bands, as illustrated in Fig. 2.4(a). In comparison with bulk, the exciton binding energy in a QD is significantly enhanced (up to five times larger as reported in M. Bayer *et al.* [55]) due to the stronger Coulomb interaction of the electron-hole pair. Excitons in QDs are of great interest as they can be treated as two-level systems, whose state can be set by resonant optical pulses [56].

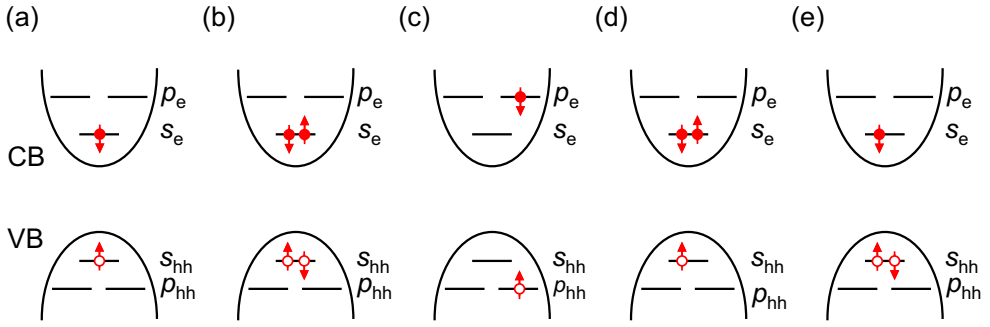

FIGURE 2.4: Schematic illustration of different QD occupations: (a) exciton (X), (b) biexciton ($2X$), (c) p-shell exciton (X_p), (d) negatively charged exciton (X^-) and (e) positively charged exciton (X^+).

An exciton can also be created in the excited states by resonant excitation, for instance in the p-shell (Fig. 2.4(c)). In this case, the exciton will rapidly relax into the ground state (X) on a ps time scale, before it recombines and emits a photon. Thus, it can be utilized as a single photon source [57]. This case will be discussed in Chapter 7.

If two excitons are captured in the dot, we get a biexciton ($2X$) (Fig. 2.4(b)). The biexciton emission energy is red shifted with respect to the exciton emission by the biexciton binding energy. This is generally true, but in some cases biexcitons are unbound and their energy are larger than that of the exciton [58]. Typical values for the biexciton binding energy in InGaAs QDs are 2-3 meV. The emission intensity of the biexciton transition exhibits a quadratic dependence on

[5] For simplicity, the ground state exciton is abbreviated to exciton.

the excitation power, whereas the emission intensity of the exciton recombination depends linearly.

Besides neutral excitons (X and $2X$), charged excitons can also be present in QDs. Figures 2.4(d) and (e) show illustrations of a single negatively and positively charged excitons, respectively. In comparison with ground state exciton, the former has a lower transition energy ($\sim$ 5 meV), while the latter has a higher energy ($\sim$ 3 meV). This shift is due to the modified few-particle Coulomb interactions (e-e repulsion and e-h attraction).

For above band gap excitation, the number of the created excitons in the dot can be controlled by the optical excitation density (P). For weak optical excitation ($P = 0.1\, W/cm^2$), each QD captures at maximum one exciton at a time (each exciton recombines before the capture of the next one). Since the relaxation times to the ground state (s-shell) are much shorter than the radiative time, almost all excitons relax to the s-shell before the recombination, and a single peak is observed in the PL spectrum. For high excitation power ($100P$), more excitons are captured in the dot and thus higher shells (p, d, f) are filled. Consequently, besides the ground state emission, peaks with higher energy appear in the PL spectrum.

For optical dipole transitions, the selection rule is given by $\Delta l = \pm 1$. The total angular momentum for the heavy hole band and conduction band are $j = 3/2$ ($m_j = \pm 3/2$) and $j = 1/2$ ($m_j = \pm 1/2$), respectively [58]. The optical interband transitions are only allowed between levels with the same angular momentum ($\Delta m = \Delta n = 0$), as illustrated in Fig. 2.3. Considering the electron and hole spin, the transition is optically allowed only for configurations where the resulting total spin of the electron and hole is ± 1, while it is forbidden for total spin of ± 2. The former is called *bright exciton* and can be generated by circular polarized light, while the later is referred to as *dark exciton* as it cannot couple to light.

2.6 Electric Field Effects: Quantum Confined Stark Effect

The response of the eigenstates of low dimensional semiconductor structures to a static electric fields is described by what is called *quantum confined Stark effect* (QCSE). This is a well-known effect in quantum wells [59, 60], quantum wires [61, 62], as well as quantum dots [63–65]. Here, we consider only the effect of electric field on QDs.

The energy shift is dependent on the orientation of the electric field. As mentioned above in Section 2.4, the dot height in SAQDs is much smaller than its

lateral extension. Hence, the response of the eigenstates to lateral electric fields is expected to be much higher than vertical ones. However, the electric field is usually applied in the vertical direction due to simplicity. Here, only the influence of electric fields applied in the vertical direction (z) of the QDs is discussed.

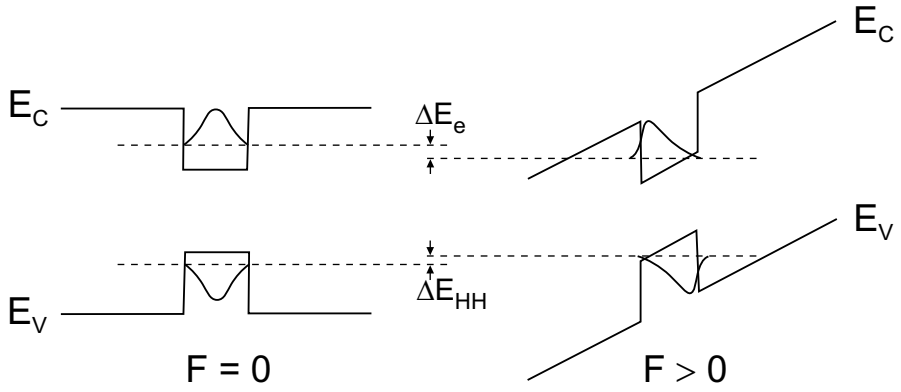

FIGURE 2.5: Schematic presentation of the quantum confined Stark effect (QCSE). The transition energy of the exciton is decreased and the overlap between the electron and wave function is reduced.

For low electric fields, the energy shift ΔE of the QD eigenstates exhibits a quadratic dependence on the applied electric field F:

$$\Delta E = \mu_{el} F + \alpha F^2, \tag{2.3}$$

where μ_{el} and α are the permanent dipole moment and the polarizability, respectively [66]. For high electric fields, the displacement of the dipole moment is limited by the size of the QD. Therefore, the energy shift shows a linear behavior with increasing electric field. Despite being simple, this approximation (equation (2.3)) describes the behavior of the QCSE very well. For a more accurate description, the reduction of the Coulomb interaction (due to the increased electron-hole separation) and the change of the quantization energy have to be considered.

The QCSE allows for a fine and very accurate tuning of the transition energy with an accuracy better than 1 μeV. This kind of tuning is important for example to bring the exciton transition energy into resonance with a cavity mode [18].

At low electric fields ($\sim 30\ kV/cm$ for InGaAs used in our group), the optical recombination processes are dominant so that the QCSE can be observed by the photoluminescence measurements. At higher fields, the photoluminescence signal vanishes since the tunneling probability of the charge carriers out of the dot increases. Alternatively, the transition energy of the exciton can be measured then by photocurrent spectroscopy [67].

2.7 Quantum Dot Spectroscopy

2.7.1 Photoluminescence Spectroscopy

Photoluminescence (PL) spectroscopy is the most common technique used to characterize QDs. Since the PL spectra give a wealth of information, especially when performing measurements at different temperatures or with different excitation intensities, this is the first step in the studies of QDs. In a PL experiment, a laser of an appropriate energy generates electron-hole pairs above the bandgap of the host material surrounding the QDs. Subsequently, these pairs relax into the discrete levels in the QD within a ps time scale, and then recombine radiatively by spontaneous emission with a typical lifetime of about 1 ns.

As discussed in Section 2.2, the small fluctuation (inhomogeneity) in the size and compositions of SAQDs give rise to inhomogeneous broadening. Thus, QD ensembles always exhibit relatively broad PL spectra. Typically, the full width at half maximum (FWHM) of the optical emission of the ground state transitions of an InGaAs QD ensemble is about 100 meV.[6] Figure 2.6(a) shows a photoluminescence spectrum of an InGaAs ensemble measured at 4.2 K with FWHM of about 50 meV. Usually, PL measurements are performed at low temperature to avoid thermal excitation.

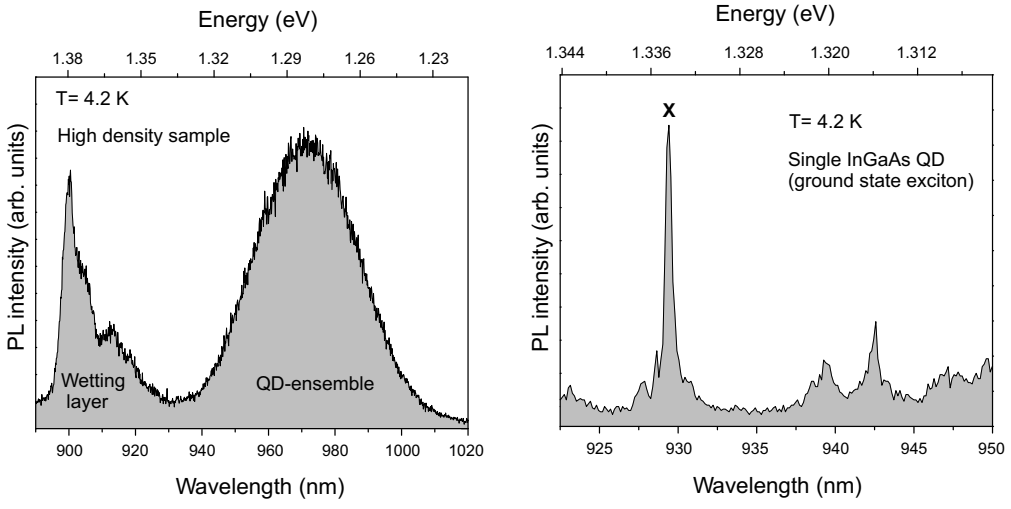

FIGURE 2.6: Photoluminescence spectrum of (a) an InGaAs QD ensemble, and (b) a single InGaAs QD.

[6] Narrower inhomogeneous linewidth down to 18.4 meV have been achieved for InGaAs QDs [68].

The PL spectra of single QDs consist of very sharp lines associated with each dot, with typical linewidths of a few μeV. These lines are attributed to the ground state exciton and higher occupied states as discussed in Section 2.5.

The PL technique has also some drawbacks. For example, as it relies on off-resonant excitaion, it cannot be used for coherent experiments. Moreover, due to the fast relaxation process into the ground state, the luminescence of an excited state of a single QD can be observed only if the ground state is occupied. Instead, higher energy states can be investigated by using absorption techniques like *photoluminescence excitation* (PLE) and *photocurrent spectroscopy*. In these experiments, the bare energy levels of an empty QD can be determined without renormalization of the energy levels due to few particle interactions [69].

In the PLE technique, the luminescence intensity is detected at the exciton ground state, while the energy of the excitation laser is scanned through the excited states. When the laser energy is on resonance with a higher exciton state, an exciton will be generated and then relaxes into the ground state where it recombines.

2.7.2 Photocurrent Spectroscopy

Photocurrent (PC) spectroscopy is an absorption technique used to characterize QDs. The high resolution and the coupling of the QD states to electrical signal are the main advantages of this method. Moreover, resonant optical excitation can be used to investigate the ground state because the detection in the PC experiments is done electrically, and thus stray light problems can be avoided (see Section 5.2). Owing to the technological difficulties to have an electrical access to single QDs, the earliest photocurrent experiments on SAQDs have been performed only on ensembles [70, 71]. Later, single QDs have been investigated via PC method [67, 72].

For PC measurements, two contacts above and below the QD layer are needed. This can be achieved by incorporating the QD into a photodiode structure (frequently either an *n*-*i*-Schottky diode or a *p*-*i*-*n* diode). This allows for applying an electric field and tuning of the transition energy via the QCSE, as well as PC detection.

Figure 2.7 shows the band structure of an *n*-*i*-Schottky diode under reverse bias.[7] The QDs embedded in the intrinsic region above the highly *n*-doped back contact. The AlGaAs barrier in the intrinsic region above the QDs is introduced to prevent current flow and leakage in forward direction.

[7] A reverse bias is used to ensure that no electrons tunnel from the back contact into the QD.

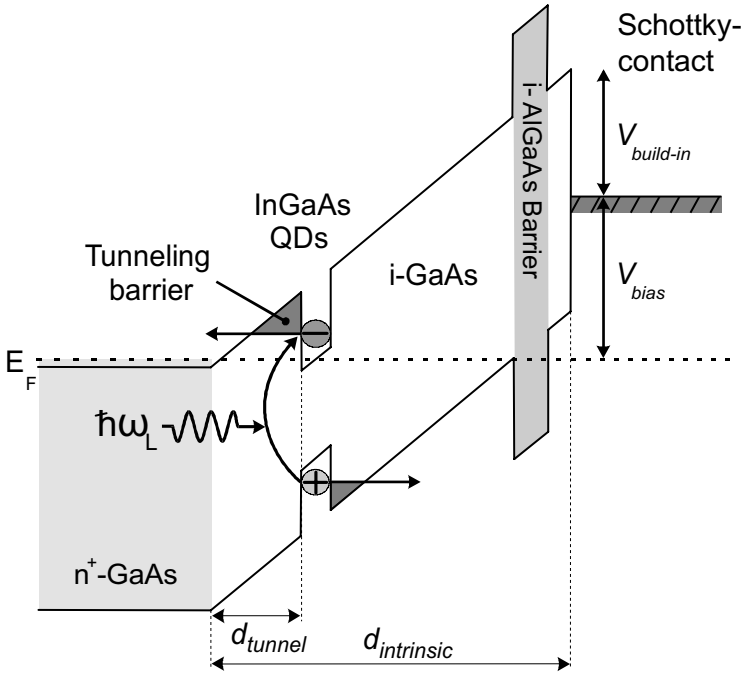

FIGURE 2.7: Band structure of an n-i-Schottky diode with QDs embedded in the intrinsic region under reverse bias. Figure is modified from reference [44].

In PC measurements, the energy of a tunable laser is tuned to an energy slightly lower (due to the QCSE) than the exciton transition energy which is already measured by PL. The resonance condition is achieved by applying an appropriate reverse bias voltage (electric field) and an electron-hole pair is created in the QD. Depending on the strength of the applied field, the exciton can decay by either radiative recombination or tunneling. At low electric fields, the radiative life time is shorter than the tunneling time of the charge carriers out of the QD and hence radiative recombination is the dominant decay mechanism. By increasing the field strength, the confinement energy is reduced and the tunneling probability increases. At a certain field ($\sim$ 30 kV for InGaAs QDs), the tunneling time becomes shorter than the radiative time and the tunneling decay is dominant. Thus, each resonance of the laser energy with a QD level results in tunneling of electron out of the dot, and subsequently an absorption peak appears in the PC spectrum. The PC is detected by using a high resolution current measurements.

For an n-i-Schottky diode with a highly doped contact, the electric field can be approximated to be linear as

$$F = \frac{V_{build-in} + V_{bias}}{d_{intrinsic}}, \tag{2.4}$$

where $d_{intrinsic}$ is the length of the intrinsic region and $V_{build-in}$ and V_{bias} are the build-in and bias voltage, respectively. For a GaAs Schottky diode $V_{build-in}$ is

typically in the range of ~ 0.8 V and only weakly dependent on the metal used for the contact. Electric fields $|F| > 150$ kV/cm can be applied before electrical breakdown occurs in the reverse direction [44].

2.8 Quantum Dot as Two Level System

Two-level system is the most basic approximation used to investigate the interaction between light and QDs. Despite its simplicity, it can be used to explain many of the quantum effects in QDs, like excitonic Rabi oscillations, single photon emission, and cavity effects like vacuum Rabi plitting. If the investigaed system includes many possible energy levels, only a specific transition is considered in two-level approximation, while other possible transitions are neglected. In QDs, usually the ground state exciton is treated as two-level system. Also, the p-shell excitons can be treated as two-level systems, as the relaxation time to the s-shell is extremely small (see Chapter 7).

The Schrödinger equation can only describe the pure states (no interaction with environment), but in reality two-level system interacts with the environment. The interaction leads to some effects like dephasing, which cannot be included in the Schrödinger equation. The density matrix formalism allows for treating open quantum systems (interact with environment) and describing the quantum state of two-level systems.

The density matrix of a two-level system is a 2×2 Hermitian matrix with a unit trace

$$\boldsymbol{\rho} = \begin{pmatrix} \rho_{00} & \rho_{01} \\ \rho_{10} & \rho_{11} \end{pmatrix}. \tag{2.5}$$

The diagonal terms ρ_{00} and ρ_{11} represent the population of the lower and upper levels of the system, respectively. They are clearly real and satisfy $\rho_{00} + \rho_{11} = 1$. The off-diagonal terms ρ_{01} and ρ_{10} define the coherence of the system; therefore they are usually referred to as the *coherence elements*. They have non-zero values only when the system is in coherent superposition states. These terms become zero when the phase between the two-level system and the light field is lost. They are generally complex and satisfy the relation $\rho_{01} = \rho_{10}^*$.

The density matrix of a two-level system can be represented by Bloch sphere (Fig. 2.8). The Bloch vector $\mathbf{R} = (u, v, w)$ can be written in terms of the matrix density elements as:

$$u = \rho_{01} + \rho_{10} \quad = 2Re\left(\rho_{10}\right), \tag{2.6a}$$

$$v = i\left(\rho_{10} - \rho_{01}\right) = 2Im\left(\rho_{10}\right), \tag{2.6b}$$

$$w = \rho_{11} - \rho_{00}\,, \tag{2.6c}$$

where w corresponds to the population inversion of the system, u and v are the dispersive and absorptive components of the dipole moment, respectively. For pure states, the Bloch vector remains on the surface of the sphere with radius equal to unity: $u^2 + v^2 + w^2 = 1$, whereas it lies inside the sphere when damping processes are present (mixed states).

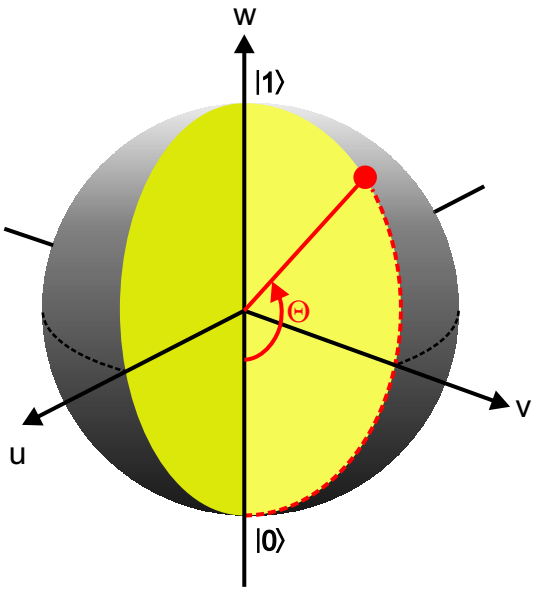

FIGURE 2.8: Bloch sphere representation of two-level system. The Bloch vector can span the whole sphere by an appropriate pulse area Θ and detuning δ. Points on the surface of the sphere correspond to pure states, while points inside the sphere represent mixed states.

In the interaction picture, the time evolution equation of the density matrix is given by the quantum *Liouville equation*

$$i\hbar\frac{\partial}{\partial t}\rho\left(t\right) = \left[H\left(t\right), \rho\left(t\right)\right]. \tag{2.7}$$

Solving this equation for all terms of the density matrix by using dipole and rotating-wave approximations, one obtains the so called *optical Bloch equations* in terms of Bloch vector components [73]:

$$\dot{u} = -\delta v \,, \tag{2.8a}$$

$$\dot{v} = \delta u + \Omega_0 (t)\, w \,, \tag{2.8b}$$

$$\dot{w} = -\Omega_0 (t)\, v \,, \tag{2.8c}$$

with $\Omega_0(t)$ being the *Rabi frequency* which is given by

$$\Omega_0 (t) = \frac{\mu E (t)}{\hbar}. \tag{2.9}$$

As the Rabi frequency directly proportional to the electric field strength, the QD exciton in optical cavities is expected to show a higher Rabi frequency in comparison to bulk QD excitons.

At resonance ($\delta = 0$), the probability to find an electron in the upper level of a two-level system (or equivalently forming an exciton in a QD), is obtained by solving the optical Bloch equations as[8]

$$\rho_{11} = \sin^2 (\Omega_0 t/2) = \sin^2 (\Theta/2) \,. \tag{2.10}$$

Here, Θ is the pulse area representing the angle by which Bloch vector $\mathbf{R}$ is rotated under application of an external field. Usually, pulsed lasers are used in coherent experiments, therefore the electric field amplitude is time dependent and Θ is defined as:

$$\Theta = \int_0^t \Omega(t) dt. \tag{2.11}$$

For example, an exciton in a single QD can be prepared by a π-pulse, while a 2π-pulse returns the system into the ground state. To observe Rabi oscillations, we need a control over the pulse area. The pulse area can be manipulated by changing either the pulse length continuously or the intensity of the pulse. The latter is usually preferred as it is much easier (see Chapter 7).

When the frequency of the laser is close to resonance ($\delta \neq 0$), the transition probability is modified to

$$\rho_{11} = \frac{\Omega_0^2}{\Omega^2} \sin^2 (\Omega t/2) \,, \tag{2.12}$$

where $\Omega^2 = \Omega_0^2 + \delta\omega^2$.

[8] For the derivation see references [74, 75].

Figure 2.9(a) shows Rabi oscillations for different values of detuning calculated by using equation (2.12). It is obvious that the frequency of the oscillations increases, while the amplitude decreases with increasing the detuning.

So far, we considered only an ideal case where the two-level system exhibits no relaxation. In reality, two-level system is not isolated. It interacts with its surrounding. The interaction leads to a disturbance in the phase coherence of the system. These interactions can be classified into processes with energy relaxation and phase relaxation. The former includes processes resulting in a change in the population occupancy of the system, like optical recombination and phonon emission (or absorption), and is characterized by the longitudinal lifetime (T_1). The latter corresponds to processes that change the phase of the induced dipole moment of the system without changing its occupation, like elastic scattering with phonons and charge carriers, and is characterized by the transverse lifetime (T_2).

For SAQDs, the decay rate is dominant over the non-radiative decay due to the quasi-perfect crystal structure of the dots. Thus, the latter can be ignored and the decay rate is given accordingly by $\gamma_{rad} = 1/T_1$. For coherent phenomena like Rabi oscillations, the damping processes disturb the coherence of the system manifested in a damped oscillation behavior. Even the population decay leads to loss of the phase coherence since it undergoes a relaxation. Therefore, the total dephasing rate can be written as

$$\frac{1}{T_2} = \frac{1}{2T_1} + \frac{1}{T_2^*}, \tag{2.13}$$

where T_2^* is called the pure dephasing that corresponds to the phase decoherence without changing the population. At low temperatures (a few K), there is no pure dephasing for the QD exciton. Consequently, the last equation is reduced to

$$\frac{1}{T_2} = \frac{1}{2T_1}, \tag{2.14}$$

The homogeneous linewidth of the QD exciton transition can be written in terms of T_2 as

$$\Gamma = 2\hbar/T_2. \tag{2.15}$$

Typical values for T_2 are some hundreds of ps. Thus, to observe coherent phenomena in QDs, like Rabi oscillations, a laser with pulse width much smaller than the T_2 is needed. Usually, ps lasers are used for this purpose. The lifetime constant T_2 can be measured by some techniques like quantum beat experiments [76, 77] and four-wave mixing [78]. On the other hand, the ground state QD exciton

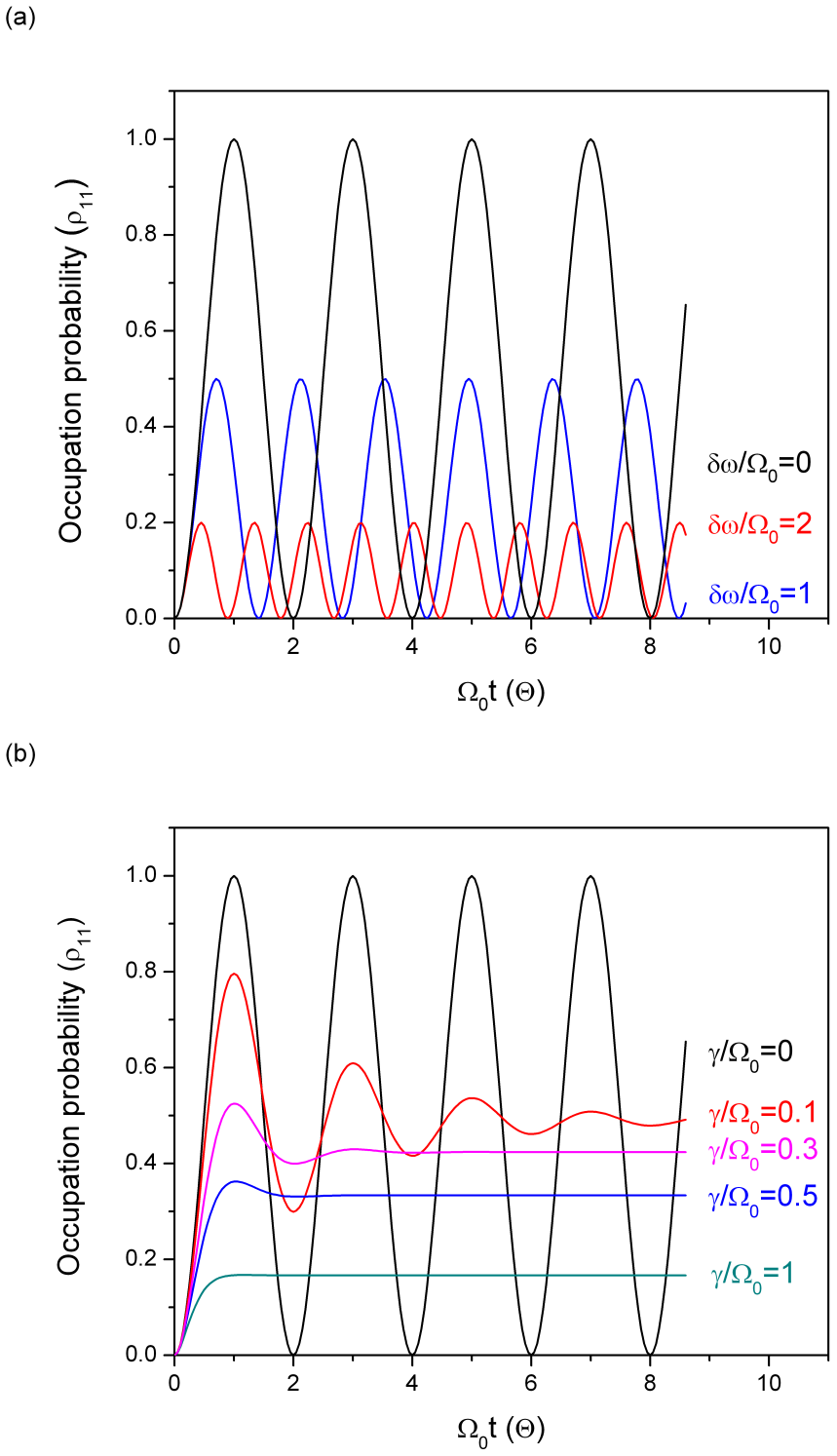

FIGURE 2.9: Time evolution of the occupation probability of the upper level ρ_{11} for (a) different values of detuning in terms of Rabi frequency (without damping), and for (b) different damping rates (without detuning).

has a typical value of T_1 of ~ 1 ns, which corresponds to a linewidth on the order of μeV. The T_1 lifetime can be measured by time-resolved PL measurements.

In order to see the effect of damping on the dynamics of two level system, the relaxation terms T_1 and T_2 have to be included in the optical Bloch equations:

$$\dot{u} = -\delta v - \frac{u}{T_2}, \tag{2.16a}$$

$$\dot{v} = \delta u + \Omega_0(t)\, w - \frac{v}{T_2}, \tag{2.16b}$$

$$\dot{w} = -\Omega_0(t)\, v - \frac{w - w_0}{T_1}. \tag{2.16c}$$

In this case, the occupation probability for the upper level is given by [74]:

$$\rho_{11} = \frac{1}{2(1+2\xi^2)} \left\{ 1 - \left(\cos \Omega t + \frac{3\xi}{(4-\xi^2)^{1/2}} \sin \Omega t \right) e^{-\frac{3\gamma t}{2}} \right\}, \tag{2.17}$$

where $\xi = \gamma/\Omega_0$ and $\Omega = \Omega_0\sqrt{1-\xi^2/4}$.

Figure 2.9(b) shows Rabi oscillations for a two-level system in the presence of damping according to equation (2.17). For weak damping ($\gamma/\Omega_0 = 0.1$), a few damped oscillations are observed before reaching a limit where the probabilities for the upper and lower levels are equal at high excitation intensities ($\rho_{00} = \rho_{11} = 0.5$). For strong damping ($\gamma/\Omega_0 = 1$), Rabi oscillations are not observed anymore as the coherence of the system is totally lost.

Please note that equation (2.17) is valid only when the electric field is assumed to be time independent. In our experiments, the laser has a hyperbolic secant envelope, and thus for an accurate description this has to be included in the calculation.

2.9 Quantum Dots in Optical Cavities

Due to the large refractive index contrast between III-V semiconductors and air, the extraction efficiency of light from QDs is very small. For example, the theoretical calculations show that the extraction efficiency of QDs in GaAs is about 2% [79]. The experimentally measured efficiency was shown to be even much lower, only 0.01% [9]. This could hinder experiments on QDs or at least make it become more difficult. Also, this limits potential applications that require high output intensity like light emitting diodes (LEDs). Fortunately, embedding QDs in optical

cavities can significantly increase the light extraction efficiency by forcing directional emission [29]. Also, this can find applications in low the threshold lasers as the spontaneous emission which is not coupled to the cavity mode is strongly suppressed [80]. Moreover, embedding single QDs in cavities allows the observation of important cavity quantum electrodynamics (cQED) effects, like tailoring the spontaneous emission rate (Purcell effect) in the weak coupling regime, and vacuum Rabi splitting in the strong coupling regime. These effects will be discussed briefly in this section.

When studying the interaction between a QD exciton and the cavity field, there are important time-scale parameters determining the strength of the QD-cavity interaction to be considered. This includes the non-resonant decay rate of the QD dipole γ, the cavity decay rate γ_{cav}, and the coupling rate g. The decay rate in a cavity gives rise to a finite linewidth of the cavity mode ($\gamma_{cav} = \Delta\omega = 1/\tau_{cav}$), which can be expressed in terms of quality factor $\gamma_{cav} = \omega/Q$. The exciton-photon coupling constant g is given by:

$$g = \frac{1}{\hbar} \left| \langle \mathbf{d} \cdot \mathbf{E} \rangle \right|, \tag{2.18}$$

where $\mathbf{d}$ is the electric dipole moment of the QD and $\mathbf{E}$ is the magnitude of the electric field at the dot position in the cavity [81]. By assuming that the QD is located at the field maximum, we can express the coupling constant in terms of the oscillator strength[9] f as [82]:

$$g = \sqrt{\frac{1}{4\pi\epsilon_r\epsilon_0} \frac{\pi e^2 f}{m_0 V_m}}, \tag{2.19}$$

with ϵ_r and ϵ_0 being the relative and vacuum permittivity, e the electron charge, m_0 the free electron mass, and V_m the effective mode volume. From this equation, it is clear that the interaction strength has larger values for small mode volumes. Therefore, PhCs are ideal systems for light-matter interaction as they provide very small mode volumes which is comparable with the wavelength of light $(\lambda/n)^3$.

Depending on the ratio between the coupling factor g and the decay rates of the QD-cavity system (γ_{cav} and γ), the interaction in cQED can be classified into *weak* and *strong coupling regimes*.

2.9.1 Weak Coupling Regime

Weak coupling occurs when the QD-cavity coupling rate g is smaller than any of the loss rate in the system, i.e., $g < \gamma_{cav}$ or γ. In this case, the photons leakage rate

[9] The oscillator strength of an electric dipole is $f = \frac{2m\Omega_0 d^2}{e^2\hbar}$ [82].

out of the cavity is larger than the characteristic interaction time between the dot and the cavity. Therefore, the spontaneous emission (SE) process is irreversible. In comparison with vacuum, the photon density of states (DOS) is increased for the cavity resonances and decreased for other frequency ranges away from the cavity modes. As a consequence of the DOS modification, the SE rate of a QD is enhanced on-resonance with a cavity mode and suppressed for the off-resonance case.[10] This phenomenon is called *Purcell effect*. The enhancement of the SE rate (reduction of the life time) results in a higher single photon pulse repetition rate, i.e., single photon emitters working at higher frequency.

Due to the broad spectra of solid-state emitters (like bulk semiconductors and quantum wells), it has not been possible to observe Purcell effect in these systems. However, the first demonstration of the Purcell effect in solid-state system was achieved in QD ensemble embedded in micropillar cavities [11]. After that, the Purcell effect has been observed for single QDs in microdisks [83], micropillars [84], and photonic crystal [13].

To show the effect of the cavity on the SE, we compare the SE rate of a QD transition in a homogeneous surrounding medium and in a cavity. The transition rate for SE of an electric dipole is given by the Fermi's golden rule:

$$\gamma_{SE} = \frac{1}{\tau_{SE}} = \frac{2\pi}{\hbar^2}\rho\left(\omega_e\right)\left|\langle \mathbf{d}\cdot\mathbf{E}\rangle\right|^2, \tag{2.20}$$

where $\rho\left(\omega_e\right)$ is the photon density of states at the energy $\hbar\omega_e$ of the emitter, and $\langle \mathbf{d}\cdot\mathbf{E}\rangle$ is the transition matrix element. In a homogeneous medium with a refractive index n, the photon density of states (DOS) is given by:

$$\rho_0\left(\omega\right) = \frac{\omega^2 V n^3}{\pi^2 c^3}, \tag{2.21}$$

where V is a normalization volume.

As mentioned earlier, the local DOS in a cavity will be increased at the resonance frequencies and will be suppressed elsewhere. In this case, the DOS have a normalized Lorentzian function [81]:

$$\rho_{cav} = \frac{2}{\pi\Delta\omega_{cav}}\frac{\Delta\omega_{cav}^2}{4\left(\omega_e-\omega_{cav}\right)^2+\omega_{cav}^2}. \tag{2.22}$$

By using the Fermi's golden rule and taking the ratio of equations (2.21) and (2.22), we obtain the so-called *Purcell factor*. It describes the amount of enhancement or suppression of the SE rate of an emitter in a cavity in comparison with

[10] The suppression for the off-resonance case is due to the absence of the photon modes as a result of the photonic band gap.

its vacuum value:

$$F_P = \frac{\gamma_{cav}}{\gamma_0} = \frac{3Q\left(\lambda_{cav}/n\right)^3}{4\pi^2 V_m} \frac{\Delta\omega_{cav}^2}{4\left(\omega_e - \omega_{cav}\right)^2 + \omega_{cav}^2} \frac{\left|\mathbf{E}\left(\mathbf{r}\right)\right|^2}{\left|\mathbf{E}_{max}\right|^2} \left(\frac{\mathbf{d}\cdot\mathbf{E}\left(\mathbf{r}\right)}{dE}\right)^2. \quad (2.23)$$

The first term includes the cavity parameters Q and V_m. The second term considers the spectral overlap between the emission of the emitter and the cavity mode. The third term gives the magnitude of the electric field at the location of the emitter relative to the maximum field in the cavity. The last term describes the orientation matching between the dipole and the field in the cavity. A maximum value of F_P can be achieved for the resonance case with the dipole orientated along the cavity field direction and located at the electric field maximum. In this case, F_P is given by:

$$F_P = \frac{3Q\left(\lambda_{cav}/n\right)^3}{4\pi^2 V_m}. \quad (2.24)$$

From this equation, it is clear why it is important to realize cavities with maximized figure of merit Q/V_m. PhCs support both high Q-factor and very small mode volume V_m, which leads to a large Purcell factor and significantly enhances light-matter interaction.

The Purcell factor is a characteristic parameter for the cavity: SE rate enhancement occurs when $F_P > 1$, while suppression of the SE rate is observed for $F_P < 1$. Another parameter used to characterize the cavity is the SE coupling factor β, which is defined as the fraction of the total SE that is coupled into a single cavity mode [74]:

$$\beta = \frac{F_P}{1 + F_P}. \quad (2.25)$$

This is typically below 10^{-5} in bulk laser, but it can approach unity in optimized cavities [13, 85].

2.9.2 Strong Coupling Regime

In contrast to the weak coupling, the dissipation of energy is strongly reduced in the strong coupling regime. The strong coupling can be observed only when the exciton-photon coupling rate is larger than other loss rates in the system ($g > \gamma_{cav}, \gamma$). This can be understood as follows: by increasing the Q of the cavity, the lifetime of the dot is decreased according to Purcell effect, while the cavity photon lifetime is increased. When we reach a case where both of these time-scales are approximately equal, the photon emitted by the dot can be reabsorbed. In

this case, the SE is a reversible process, and the QD and the cavity exchange the energy forth and back coherently with a rate known as Rabi frequency (Ω), and the system is said to be strongly coupled. In this case, the exciton-photon system can be considered as a quasi-particle, known as cavity *polariton*.

In this limit, equation (2.24) is not applicable anymore. Further increase in Q will not decrease the dot lifetime. Instead the coupling strength (Rabi frequency) is increased. In this regime, the QD-cavity system is characterized by one lifetime which is set by the Q, and by Rabi frequency Ω. In practice, high-Q cavities are not perfect, thus QD-cavity coupling sustains for a finite amount of time and a damping of the Rabi oscillations is observed.

Strong coupling was demonstrated in quantum wells [86] and even in wavelength-thickness layers of bulk semiconductors [87]. For single QDs, strong coupling to a cavity mode has been realized in optical cavities like microdisks [94], micropillars [88], as well as photonic crystals [32, 89].

At the resonance condition, the QD-cavity system exhibits an anti-crossing behavior, known as *vacuum Rabi splitting*. According to the coupled harmonic oscillators model [90], the energy difference between the QD exciton and the cavity mode at resonance is given by:

$$\Delta E = 2\hbar\Omega = 2\hbar\sqrt{g^2 - \frac{(\gamma_{cav} - \gamma_X)^2}{16}}, \tag{2.26}$$

where Ω is the Rabi frequency. According to this equation, a splitting occurs only if the square root has a real value. Thus, the strong coupling can be observed only when

$$g^2 > \frac{(\gamma_{cav} - \gamma_X)^2}{16}. \tag{2.27}$$

Typically, the linewidth of a QD exciton is on the order of a few μeV at low temperatures, whereas it is considerably larger for high-Q cavities ($\sim$ 100 μeV) [91]. Therefore, the condition in equation (2.27) can be approximated to

$$g > \frac{\gamma_{cav}}{4}. \tag{2.28}$$

This equation represents the threshold condition for observing strong coupling. By considering equation (2.19) and using $Q = E_{cav}/\gamma_{cav}$, we note that the figure of merit $Q\sqrt{f/V_m}$ has to be maximized to observe strong coupling [92].

2.10 Types of Cavities

Incorporation of low dimensional semiconductor nanostructures, especially QDs, in cavities is of great interest not only for basic research, but also for possible applications like lasers or single photon sources. So far, several kinds of cavities like planar distributed Brag reflectors, micropillars, microdisks and two-dimensional photonic crystals have been utilized for these purposes. A brief description for each type will be given here.

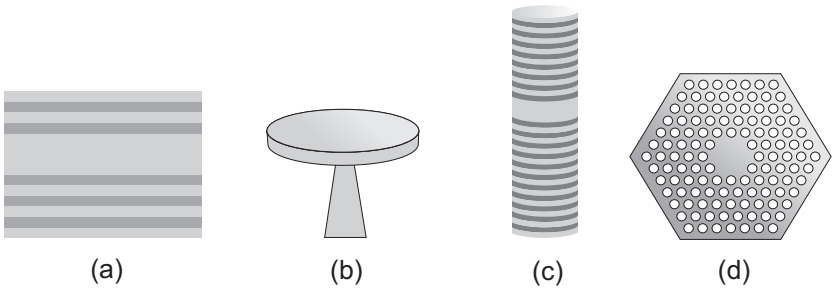

FIGURE 2.10: Schematic illustration of (a) planar distributed Brag reflector (DBR) cavity (b) microdisk, (c) micropillar, and (d) two-dimensional photonic crystal cavity.

Planar distributed Brag reflector (DBR) cavities: The cavity is build up by two Bragg mirrors, which are formed by thin layers of dielectrics with high refractive index contrast, as depicted in Fig. 2.10(a). DBR cavity is also called one-dimensional photonic band gap cavity as the optical confinement exists only in one dimension (perpendicular to the DBRs). The highest achievable reflectivity with Bragg mirrors is obtained for layer thickness of $\lambda/4$. Usually the bottom Bragg mirror is thicker than the top one, in order to couple the light out. This type of cavities can be produced easily by using epitaxial growth of the Bragg reflectors. High Q-factors, up to 10 000, have been realized [93] whereas the mode volume is relatively large.

Microdisks: The microdisk cavity consists of a thin semiconductor disk of high refractive index on a post structure, as illustrafted in Fig. 2.10(b). The fabrication process is usually a combination of reactive ion etching, which etches the layer forming the disk, and selective wet etching of a sacrificial layer underneath. The cavity modes, called *whispering gallery modes* (WGM), are usually present at the circumference of the disk. The light is confined in the disk by the total internal reflection at the interfaces. High Q-factors up to 100 000 and small mode volume $\sim 6(\lambda_0/n)^3$ can be obtained [94]. The main disadvantage of microdisks that they do not provide directional emission.

Micropillars: Dry etching of a planar DBR cavity results in what is called micropillar (Fig. 2.10(c)). The optical confinement in the vertical direction is

achieved by the DBR mirrors, and in the plane direction via total internal reflection due to the high refractive index contrast between the semiconductor and air. Micropillars offer relatively high Q and small cavity volume on the order of a few cubic wavelengths. Q-factors up to 165 000 have been achieved for micropillars with diameters of 4 μm by increasing the number of mirror pairs in the DBR and an optimized etching process [95].

This kind of cavities provides highly directional emission in the vertical direction, and therefore high extraction efficiency [12]. Thus, they are interesting for single photon source experiments.

Two-dimensional photonic crystal cavities: This type of cavities is produced by introducing a defect at the center of photonic crystal structure, as illustrated in Fig. 2.10(d). Light is trapped in the in-plane direction via the photonic band gap, due to multiple reflections at the sidewalls-air interfaces, and in the vertical direction by the total internal reflection. Photonic crystal cavities support both high Q-factors and extremely small mode volume comparable to, or even smaller than, $(\lambda/n)^3$. For example, H1 cavity with Q-factor up to 50 000 and mode volume of $\sim 0.43(\lambda/n)^3$ was reported by Y. Ota *et al.* [96].

Among the types of cavities mentioned above, photonic crystal cavities are the most promising for potential applications, for example they are compatible for on-chip integration [97]. A detailed description of the basic properties of two-dimensional photonic crystal cavities will be discussed in the next chapter.

Chapter 3

Basics of Photonic Crystlas

3.1 Light Propagation in Photonic Crystals

All of macroscopic electromagnetism, including the propagation of light in a photonic crystal, is governed by the Maxwell's equations.[1] Under the assumptions of linear, isotropic, low-loss, nondispersive, non-magnetic medium, and with the absence of free charges and electric current, the Maxwell's equations are given by:

$$\nabla \cdot [\epsilon(\mathbf{r})\mathbf{E}(\mathbf{r},t)] = 0, \tag{3.1a}$$

$$\nabla \cdot \mathbf{H}(\mathbf{r},t) = 0, \tag{3.1b}$$

$$\nabla \times \mathbf{E}\,(\mathbf{r},t) = -\mu_0 \frac{\partial}{\partial t}\mathbf{H}\,(\mathbf{r},t), \tag{3.1c}$$

$$\nabla \times \mathbf{H}\,(\mathbf{r},t) = \epsilon\epsilon_0 \frac{\partial}{\partial t}\mathbf{E}\,(\mathbf{r},t), \tag{3.1d}$$

where $\mathbf{E}$ and $\mathbf{H}$ are the harmonic complex electric and magnetic fields, respectively. By assuming an infinite periodic structure and using Bloch theorem, it can be shown that the Maxwell's equations are simplified to an eigenvalue problem [22], known in literature as the *master equation*:

$$\left[(i\mathbf{k}+\nabla)\times\frac{1}{\epsilon\,(\mathbf{r})}\,(i\mathbf{k}+\nabla)\times\right]\mathbf{u}_\mathbf{k}\,(\mathbf{r}) = \left(\frac{\omega\,(\mathbf{k})}{c}\right)^2\mathbf{u}_\mathbf{k}\,(\mathbf{r})\,, \tag{3.2}$$

with $\mathbf{u_k(r)}$ being the periodic Bloch function of the magnetic field $\mathbf{H_k} = \mathbf{u_k(r)}e^{i\mathbf{k}.\mathbf{r}}$. This method is called *plane wave approximation.*

In general, photonic crystals exhibit discrete translational symmetries. This means that the structure (dielectic) is invariant for only a multiple of a certain vector. This discrete symmetry implies that $\mathbf{u_k(r)} = \mathbf{u_k(r+R)}$ and $\epsilon\,(\mathbf{r}) = \epsilon\,(\mathbf{r}+\mathbf{R})$,

[1] Major part of this chapter is based on reference [22].

where $\mathbf{R}$ is an integer multiple of the lattice constant a ($\mathbf{R} = n\boldsymbol{a}$). Therefore, only the magnetic field in the unit cell needs to be determined. As in solid state physics, a unit cell in photonic crystal can be defined by the primitive lattice vectors $\boldsymbol{a}_1$, $\boldsymbol{a}_2$, and $\boldsymbol{a}_3$. To plot the dispersion relation of the light propagation in periodic structure, the reciprocal space is used. The primitive reciprocal lattice vectors are given by:

$$\mathbf{b}_1 = \frac{2\pi(\boldsymbol{a}_2 \times \boldsymbol{a}_3)}{\boldsymbol{a}_1 \cdot (\boldsymbol{a}_2 \times \boldsymbol{a}_3)}, \quad \mathbf{b}_2 = \frac{2\pi(\boldsymbol{a}_3 \times \boldsymbol{a}_1)}{\boldsymbol{a}_1 \cdot (\boldsymbol{a}_2 \times \boldsymbol{a}_3)}, \quad \mathbf{b}_3 = \frac{2\pi(\boldsymbol{a}_1 \times \boldsymbol{a}_2)}{\boldsymbol{a}_1 \cdot (\boldsymbol{a}_2 \times \boldsymbol{a}_3)}. \tag{3.3}$$

The reciprocal lattice vector $\mathbf{G}$ is defined as: $\mathbf{G} = l_1\mathbf{b}_1 + l_2\mathbf{b}_2 + l_3\mathbf{b}_3$. The unit cell in the reciprocal lattice, the *first Brillouin zone*, is a subset of wave vectors $\mathbf{k}$ and it contains all information about the dispersion relation. Since the dispersion relation is periodic, there is no need to examine the wave vectors $\mathbf{k}$ which are outside the Brillouin zone.

By solving equation (3.2) numerically as a function of $\mathbf{k}$, we obtain the band structure of the system. Also, the magnetic field distribution for a given frequency can be obtained by solving this equation. Once the modes $\mathbf{H}_\mathbf{k}$ are known for a given frequency, the electric field distribution $\mathbf{E}_\mathbf{k}$ can be obtained directly from the Maxwell's equations.

This method is applicable for only an infinite periodic structure, therefore it is not suitable for calculations of PhC cavities. It is also inapplicable for complicated structures and dynamic characteristics. Therefore, other methods such as the Finite-Difference Time-Domain method are usually used for PhC cavities calculations (see Section 3.7). This method allows the simulation of electromagnetic field distribution of complicated structures, as well as many other properties like transmission and reflection coefficients.

3.2 One-Dimensional Photonic Crystals

The one-dimensional (1D) PhC consists of periodic layers of two materials with different dielectric constant ϵ. The system exhibits periodic modulation in one direction (z) with period determined by the lattice constant a, whereas it is homogeneous in the xy plane. Thus, the structure has a discrete translational symmetry in the z-direction. According to Bloch theorem, the mode solution can be written in the form:

$$\mathbf{H}_{n,k_z,\mathbf{k}_\parallel}(\mathbf{r}) = e^{i\mathbf{k}_\parallel \cdot \boldsymbol{\rho}} e^{ik_z z} \mathbf{u}_{n,k_z,\mathbf{k}_\parallel}(z), \tag{3.4}$$

where n is the band number, $\boldsymbol{\rho}$ represents a vector in the xy plane, $\mathbf{k}_{\|}$ and k_z are the wave vectors in the plane and in the z-direction, respectively. The function $\mathbf{u}(z)$ is periodic in z: $\mathbf{u}(z) = \mathbf{u}(z+R)$, where R is an integer multiple of the lattice constant a. Due to the continuous translational symmetry in the plane, the wave vector $\mathbf{k}_{\|}$ may have any value. On the other hand, since the system has discrete translational symmetry in the z-direction, the Bloch state with k_z and $k_z + \mathbf{G}$ are identical and therefore the mode frequency must be the same: $\omega(k_z) = \omega(k_z + \mathbf{G})$. Here, the reciprocal lattice vector is defined as $\mathbf{G} = m\mathbf{b}$, where m is an integer and $\mathbf{b} = 2\pi/a$ is the primitive lattice vector. Because of this periodicity, it is sufficient to plot the dispersion relation (band diagram) only for wave vectors in the Brillouin zone, i.e., $-\pi/a < k_z < \pi/a$.

Origin of the Photonic Band Gap: The origin of the PBG in 1D PhC structures can be understood by investigating the propagation of light in the z-direction ($\mathbf{k}_{\|} = 0$) at three different cases. In the first case, the system consists of layers of the same material; the medium is homogeneous in all three directions. The dispersion relation of light propagating in a homogeneous medium exhibits a linear behavior:

$$\omega(k) = \frac{ck}{\sqrt{\epsilon}}. \tag{3.5}$$

Since k repeats itself outside the Brillouin zone, the *light line* folds back into the zone by the reciprocal lattice vector when it reaches an edge, as depicted in Fig. 3.1(a). In the second case (Fig. 3.1(b)), alternating layers with a small dielectric constant contrast is introduced. The photonic band structure is similar to that for homogeneous medium, except that a frequency gap appears between the upper and lower branches of the lines. This gap is called *photonic band gap* (BPG), in which no modes are allowed to propagate in the system (i.e., there are no Bloch wave solutions). The PBG shows a significant widening for high dielectric contrast medium, as illustrated in Fig. 3.1(c).

To explain why the PBG appears, we have to consider the electric field mode profiles at the folding points for the states above and below the gap. The gap occurs at the edge of the Brillouin zone (π/a). At the edge of the Brillouin zone (π/a), the modes are standing waves with a wavelength of $2a$. Due to the symmetry of the system, there are only two possible distributions for such modes; the nodes can be positioned either in low-ϵ layers or in high-ϵ layers.

According to electromagnetic variational theorem, the low-frequency modes concentrate their energy in the high-ϵ regions (pulling its frequency down below the bulk value), whereas the high-frequency modes tend to concentrate their energy in the low-ϵ regions (pushing its frequency above the bulk value). Thus,

a PBG appears due to the frequency difference between the two cases. The low-frequency mode, just under the gap, concentrates most of its energy in the GaAs layer ($\epsilon = 13$), while energy of the high-frequency mode above the gap is mostly concentrated in the GaAlAs layer ($\epsilon = 12$).

Since the low-ϵ region is often air, especially in two-dimensional PhC, the band above the PBG is called the *air band*, while the band below the *dielectric band*. Even though there are no extended states in the PBG, when a light wave with a frequency in the PBG is incident at the face of the crystal from outside, it will exponentially decay into the crystal. In this case, the wave vector is complex and the modes are *evanescent*. We should note that a PBG appears as far as the light is propagating in z-direction. When a light in other directions is considered, no band gap appears since there are no periodic regions.[2]

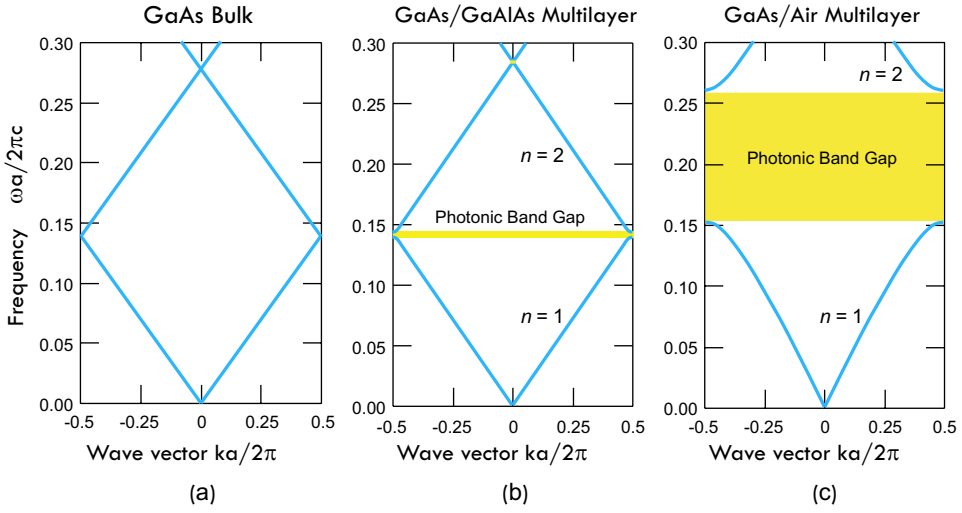

FIGURE 3.1: Photonic band structures for light propagation in the z-direction of three different structures. (a) Homogeneous GaAs (no dielectric contrast). (b) Periodic $a/2$ thick layers of GaAs ($\epsilon = 13$) and GaAlAs ($\epsilon = 12$). A band gap is formed when the dielectric contrast is introduced. (c) Alternating $a/2$ thick layers of GaAs and air. The band gap increases with the dielectric contrast. After [22].

3.3 Two-Dimensional Photonic Crystals

In 2D PhC, the dielectric constant varies periodically in two directions while it is homogeneous in the third, giving rise to a PBG in the plane of periodicity. The general aspects of the light propagation in 1D structure, like Bloch states and the formation of band structure, are applied well for the 2D case, but with more

[2] An exception of this is the omnidirectional multilayer mirror, as it reflects plane waves from any angle.

complexity. A variety of lattice symmetries are available for 2D crystals, the most common are the square and the triangular lattice of air holes in dielectric medium. The latter is usually preferred as it exhibits a much wider band gap.[3] This can be attributed to the greater symmetry and smoother Brillouin zone compared to square lattice structure.

The real space lattice is defined by the two lattice vectors $\boldsymbol{a}_1$ and $\boldsymbol{a}_2$, whereas the lattice in reciprocal space is set by the reciprocal space vectors $\boldsymbol{b}_1$ and $\boldsymbol{b}_2$, as illustrated in Fig. 3.2. The 2D system exhibits discrete translational symmetry in the xy plane: $\epsilon(\mathbf{r}) = \epsilon(\mathbf{r}+\mathbf{R})$, where $\mathbf{R}$ is any linear combination of $\boldsymbol{a}_1$ and $\boldsymbol{a}_2$. As in the 1D case, the Bloch states (solutions) can be written in the form:

$$\mathbf{H}_{n,k_z,\mathbf{k}_\parallel}(\mathbf{r}) = e^{i\mathbf{k}_\parallel\cdot\boldsymbol{\rho}} e^{ik_z z} \mathbf{u}_{n,k_z,\mathbf{k}_\parallel}(\boldsymbol{\rho}), \tag{3.6}$$

where $\boldsymbol{\rho}$ denotes a vector in the xy plane and $\mathbf{u}(\boldsymbol{\rho})$ is a periodic function: $\mathbf{u}(\boldsymbol{\rho}) = \mathbf{u}(\boldsymbol{\rho}+\mathbf{R})$.

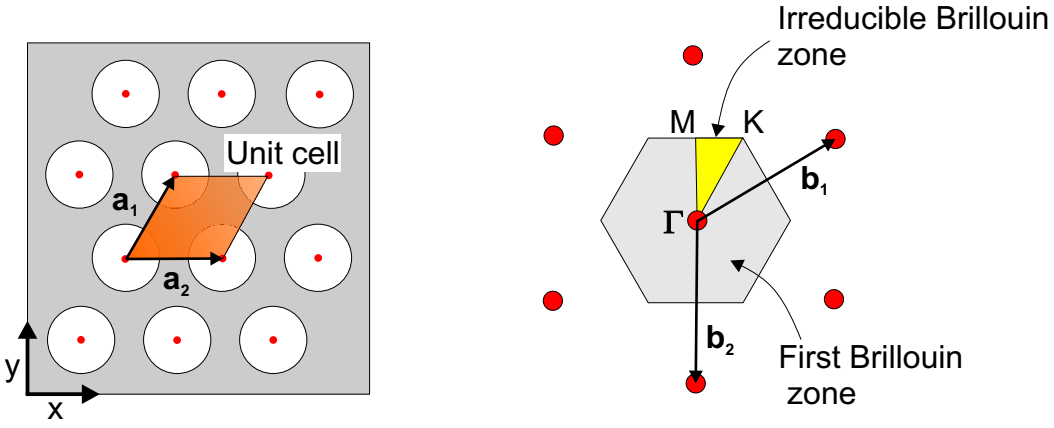

FIGURE 3.2: A triangular 2D photonic crystal lattice. (Left) Real space representation showing the unit cell. (Right) First (gray) and irreducible (yellow) Brillouin zones in the reciprocal space.

We restrict ourselves to modes that propagate only in parallel to the xy plane ($k_z = 0$). In this case, due to the mirror symmetry the modes in 2D PhC can be classified into two distinct polarizations: transverse electric (TE), in which the electric field is parallel to the plane, and transverse magnetic (TM), in which the magnetic field is parallel to the plane. These polarizations have different band structures, and therefore their band gaps do not overlap except for carefully chosen lattice dimensions. For example, as shown in Fig. 3.3, a 2D PhC with triangular

[3] For some applications, like in narrow-band filters, narrow bandgaps are preferred.

lattice of air holes in dielectric has a complete PBG[4] for both TE and TM modes, while a square lattice of dielectric columns in air has a PBG only for the TM polarization.

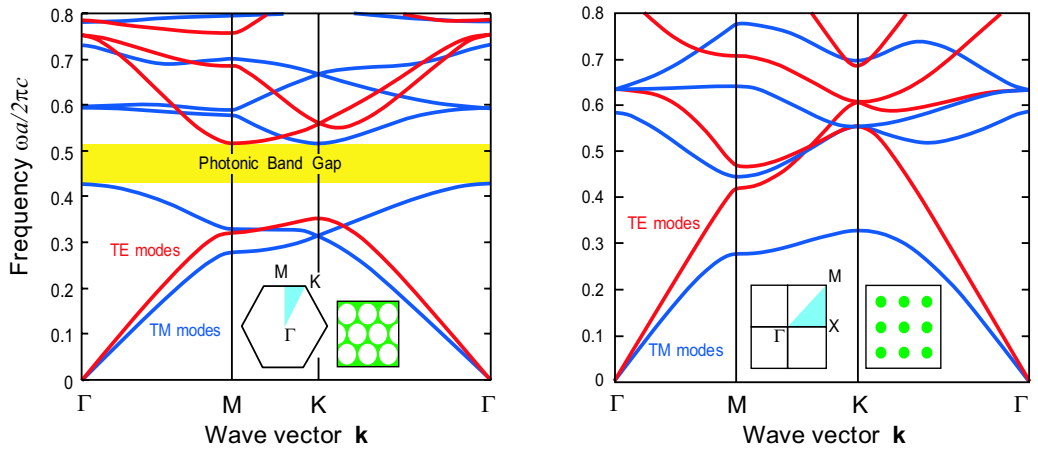

FIGURE 3.3: Photonic band structure for the eigenmodes of a 2D photonic crystal with (a) triangular lattice of air holes in a dielectric material (ϵ=13 and $r = 0.48a$), and (b) square lattice of dielectric in air ($r = 0.2a$). After [22].

Since the dispersion relation in PhC is periodic, $\omega(\mathbf{k}) = \omega(\mathbf{k}+\mathbf{G})$, it is sufficient to calculate the band diagram only for wave vectors in the Brillouin zone. However, the presence of rotation and mirror symmetry in 2D triangular lattice allows for restricting the calculation to a smaller region, the *irreducible Brillouin zone*. Note that the wave vectors $\mathbf{k}$ in the band diagram are plotted only along the boundaries of this zone. This is due to the fact that the band minima and the maxima mostly occur along the boundaries of the irreducible zone.[5]

As discussed in the last section, a PBG arises when a refractive index (dielectric) contrast is introduced. However, in 2D PhC the refractive index contrast should be high. For example, a complete PBG in triangular lattice of air holes in dielectric requires a minimum index contrast of 2.63 [22]. The *filling factor*, which determines the spectral position and the width of the PBG, is a crucial parameter to realize a complete 2D band gap. A complete PBG can be achieved only for a specific range of filling factors, which are determined by the r/a ratio.

For the out-of-plane propagation, $k_z > 0$, there are no band gaps for propagation in z-direction due to the homogeneity of the PhC in that direction. Moreover, since the mirror symmetry is broken for $k_z \neq 0$, a distinct decoupling of the TE and TM polarizations is no longer possible.

[4] Note that the TE mode has a wider band gap than the TM mode. The band gaps of the two polarizations are partly overlapping. A complete photonic band gap (yellow area) is the overlap of the gap for both polarizations.

[5] Although this is not guranteed for all structures, it is true in the case of triangular lattice.

The bands near to the Brillouin zone edges become flatter, as shown in Fig. 3.3. Hence, the group velocity, which is given by the slope of the dispersion curve: $v_g = \partial\omega/\partial\mathbf{k}$, goes to zero at the band edges. These band edges modes are used, for instance, in low threshold photonic band-edge lasers [98].

3.4 Photonic Crystal Slabs

In 2D PhC, the system has infinite length in the z-direction. In practice, however, this is not always suitable or possible to achieve. For most applications, it is required to confine the light in the third direction. The only exceptions are the PhC fibers in which the light propagates almost parallel to the z-direction. A PhC slab is made of a thin dielectric material clad in a lower index material, which is usually air. These slabs impose periodicity in two dimensions, whereas the third has a finite height which is usually on the order of half a wavelength [99]. This value is chosen to be thick enough for the fundamental mode to be well confined, while simultaneously thin enough to prevent existence of high-order modes within the slab. In slab structures, the confinement of light in the vertical direction is achieved by the means of total internal reflection (TIR), whereas the in-plane propagation is similar to that in a 2D PhC. Only PhC slabs with a triangular lattice will be discussed here.

Owing to lack of translational symmetry in the vertical direction, the guided modes are no longer pure TE and TM as in 2D case. Instead, the modes can be classified into even (TE-like) and odd (TM-like) modes with respect to reflection through the mirror symmetry plane of the slab [99]. The electric field in the TE-like mode is mostly parallel to the mirror plane, whereas the magnetic in the TM-like mode is mostly parallel to the mirror plane.

The band structure of a PhC slab with air hole radius $r = 0.2\ a$ and slab thickness $0.6\ a$ is shown in Fig. 3.4. Each point in the red (blue) curves represents a TE-like (TM-like) mode propagating along the plane of the slab. Unlike the 2D case where a band gap appears for both polarizations, the slab structure exhibits a band gap only for the guided (TE-like) modes.

A key feature that distinguishes the band structure of slabs from that of 2D crystals is the *light cone*, which is a continuum of states indicated by the violet shaded region in Fig. 3.4. The boundary between the guided and radiated modes is described by the light line, $\omega = c\left|\mathbf{k}_{\parallel}\right|$.

To understand this band diagram we consider the photonic modes in the slab and in the surrounding free space. The dispersion relation of a plane-wave in air is given by $\omega = c\left|\mathbf{k}\right| = c\sqrt{\mathbf{k}_{\parallel}^2 + k_z^2}$.

Outside the slab $k_z^2 > 0$, then there is a continuum of extended states propagating in air for $\omega > c\left|\mathbf{k}_{\|}\right|$, which referred to as *leaky modes* or *radiative modes*. These continuum states form what is called the *light cone*, and are correspond to the main radiation losses in the slab. On the other hand, when $\omega < c\left|\mathbf{k}_{\|}\right|$, then k_z is imaginary and light decays exponentially away from the slab. Thus, modes cannot couple to vertical radiation and are guided within the slab. The boundary between the leaky and guided modes is given by the light line, $\omega = c\left|\mathbf{k}_{\|}\right|$.

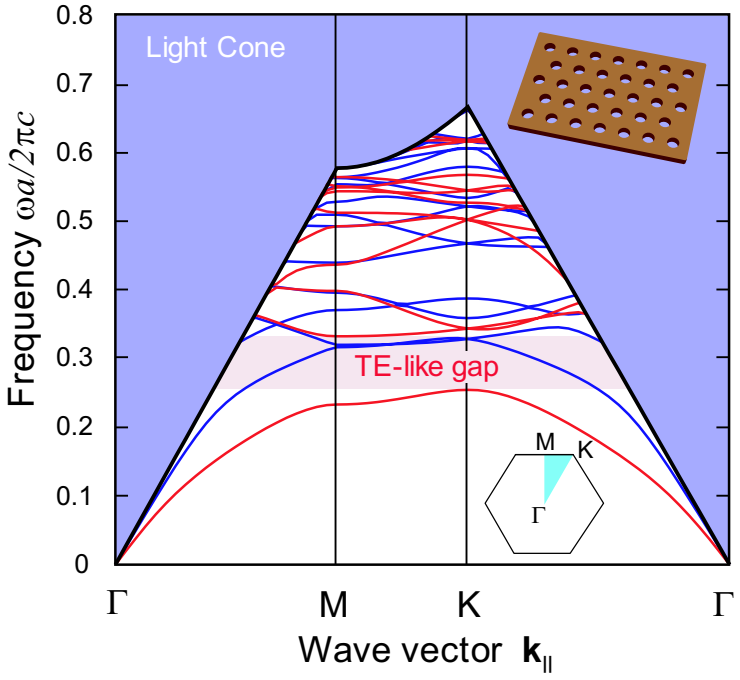

FIGURE 3.4: Photonic band structure for the eigenmodes of a GaAs PhC slab suspended in air with hole radius $r = 0.2a$ and thickness $0.6a$. The light cone is presented by the violet shaded region above the light line (solid black line), in which all of the extended modes propagating in air. The guided bands localized in the slab appear below the light cone. The blue bands represent TM-like modes whereas the red bands represent TE-like modes. A band gap exist only for TE-like modes (shaded rose region). The insets show the PhC geometry and the irreducible Brillouin zone (blue). After [22].

3.5 Nanocavities in Photonic Crystal Slabs

Point defects, usually known as *microcavities* or *nanocavities*, can be formed in PhC slabs via disrupting the symmetry of the photonic lattice by adding or removing an amount of dielectric material. These cavities allow for one or more localized

modes whose spectral positions lie in the PBG of the unperturbed PhC. The localized states, standing waves formed in the cavity, are confined to the defect region and decay exponentially into the PhC walls.

In general, the cavity modes can be classified into donor and acceptor type modes [100]. The former results from the addition of dielectric material into a PhC unit cell, and behaves like a donor level in semiconductors. This kind of modes exists close to the air band of the PhC. The latter is formed in close to the dielectric band when removing dielectric material from a unit cell, and it is similar to an acceptor level in semiconductors.

In an ideal PhC cavity free of any structural imperfections, light leakage is restricted to the vertical direction. A cavity mode of a given frequency can couple to radiative (leaky) modes in the light cone with the same frequency. For practical applications, like lasers and QED experiments, it is necessary to minimize these losses. This can be achieved by carefully designing the cavity to minimize the coupling to the light cone [25, 27, 101]. The figure of merit for characterization optical losses in cavities, the quality factor Q, can be expressed as the decay rate of the electromagnetic field energy stored in the cavity in units of the optical period T [102]:

$$Q \equiv 2\pi \frac{\tau_{ph}}{T}, \tag{3.7}$$

where τ_{ph} is the time in which the energy decays to $1/e$ of its initial value. A more convenient definition of Q is given by the relative width of the resonance:

$$Q = \frac{\omega_0}{\Delta\omega}, \tag{3.8}$$

where ω_0 is the resonant frequency and $\Delta\omega = 1/\tau_{ph}$ is the full width at half maximum (FWHM).

The quality factor Q of a cavity can be separated into two parts according to in-plane ($Q_\parallel$) and out-of-plane ($Q_\perp$) losses: $1/Q = 1/Q_\parallel + 1/Q_\perp$. As the number of the PhC layers surrounding the cavity is increased, the lateral leakage can be minimized to a value where $Q_\parallel$ saturates, and therefore the Q factor is limited by $Q_\perp$ [26].

The simplest PhC cavities like H1, formed by omitting one air hole, result in a relatively low Q values in the range of a few hundred. To improve the Q-factor, usually either the position or the size (or even both) of the air holes surrounding the cavity have to be modified (see Section 6.2).

3.6 The Finite-Difference Time-Domain Method

In Section 3.1, it was shown that the plane wave method can be used to calculate the eigenmodes for infinite periodic structures. This method also allows the calculation of the corresponding field distributions of these modes. However, this method is inapplicable in complicated structures or for dynamic characteristic investigation. Nevertheless, it is a very useful for PBG calculations of periodic structure. Other methods can be used in case of complicated PhCs to investigate the field distribution as well as other properties like transmission and reflection spectra. Among those, the Finite-Difference Time-Domain (FDTD) method is the most commonly used one due to its flexibility to treat almost all problem with high accuracy. The main disadvantage of this method is the long computational time and the need for a large memory capacity.

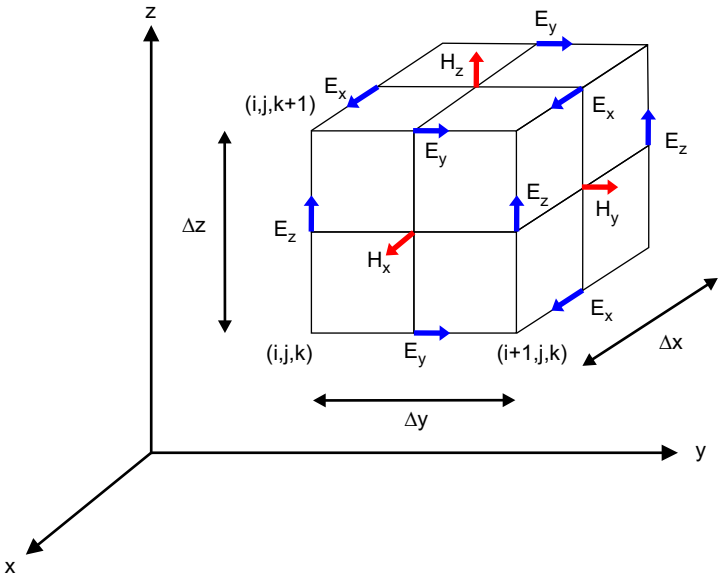

FIGURE 3.5: Positions of the electric (red) and magnetic (blue) field components in the Yee cell.

The Finite-Difference Time-Domain (FDTD)[6] simulation is the most common computational method used in designing PhC structures. It exploits the fact that in the Maxwell's equations the temporal change in the electric field $\boldsymbol{E}$ depends on the spatial variation of the magnetic field $\boldsymbol{H}$, and vice versa. In the FDTD method, the simulation space is discretized into a grid, with a grid points with spatial dimensions of Δx, Δy, and Δz. In this method, the Maxwell's curl equations (3.1c) and (3.1d) are solved by replacing the temporal and spatial derivatives by

[6] Here, the FDTD method is briefly discussed. For more detail discussion see reference [104].

finite differences. The electric and magnetic components are calculated at each grid point on the Yee cell (cube), as depicted in Fig. 3.5 [103].

The discretization in time is done by a *leap frog* scheme, where the **E**-fields at time t are calculated from the **E**-fields at $t - \Delta t$ together with the **H**-fields at $t - \Delta t/2$, and vice versa for **H**-fields at $t + \Delta t/2$, where Δt is the discretization step in time.

To obtain accurate simulation results, the spatial grid must be small enough to resolve the smallest feature of the simulated field, and the time step is estimated from the *Courant condition*:

$$c\Delta t \leq \frac{1}{\sqrt{1/(\Delta x)^2 + 1/(\Delta y)^2 + 1/(\Delta z)^2}} \tag{3.9}$$

The FDTD method gives results in the time domain which are usually Fourier transformed into the frequency domain to get information about the response of the system as a function of frequency. Thus, a wide frequency range is obtained in a single simulation run.

In addition to discretization in FDTD method, boundary conditions are applied at the boundary of the computation region. For PhC simulations, usually the perfect matched layer (PML) is utilized. The incident electromagnetic fields decay exponentially in this layer. Therefore, if the absorption coefficient is set correctly, no radiation reflected to the computation region.

Chapter 4

Fabrication Basics of Two-Dimensional Photonic Crystals

To produce high quality photonic crystal (PhC) nanocavities, some issues have to be considered like the verticality and smoothness of the sidewalls of the air holes. Imperfections in the PhC structure can lead to a significant reduction of the quality factor of the cavity [105]. For example, non-vertical sidewalls leads to coupling to radiative modes (see ref. [106]), and rough sidewalls lead to optical scattering at the surfaces. Therefore, a considerable time was spent to obtain and improve the process conditions. This chapter provides an overview of the fabrication procedure of PhC cavities with embedded quantum dots. Section 4.1 gives a brief view about the InGaAs QD samples grown by molecular beam epitaxy technique, including the growth conditions and the layer structure. A detail description of the fabrication process of PhC cavities is provided in Section 4.2.

4.1 Growth of InGaAs Quantum Dot Samples

In this work, the InGaAs QDs samples were grown by molecular beam epitaxy (MBE) using Stranski-Krastanov growth mode.[1] All samples have been grown on (100)n^+-GaAs substrates. Figure 4.1(a) shows a schematic presentation of the layer sequence. First, GaAs buffer layer of 50 nm is grown on the GaAs substrate, followed by a 450 nm sacrificial layer of $Al_{0.95}Ga_{0.05}As$. The QDs are embedded in a 180 nm ($\lambda/2$) thick layer which is composed of GaAs and two layers of $Al_{0.25}Ga_{0.75}As$. The two 20 nm thick layers of $Al_{0.25}Ga_{0.75}As$ are introduced above and below the QD layer to confine the charge carriers in the active region.

[1] The samples were grown by Prof. Dr. Dirk Reuter at Ruhr-Universität Bochum (RUB).

The growth temperature was 520 °C for the QDs, while it was 600 °C for the other layers. The diameter of the obtained QDs is ∼ 30 nm with a height of ∼ 5 nm. Figures 4.1(b)-(d) show SEM images of a grown sample before capping the QDs by GaAs.

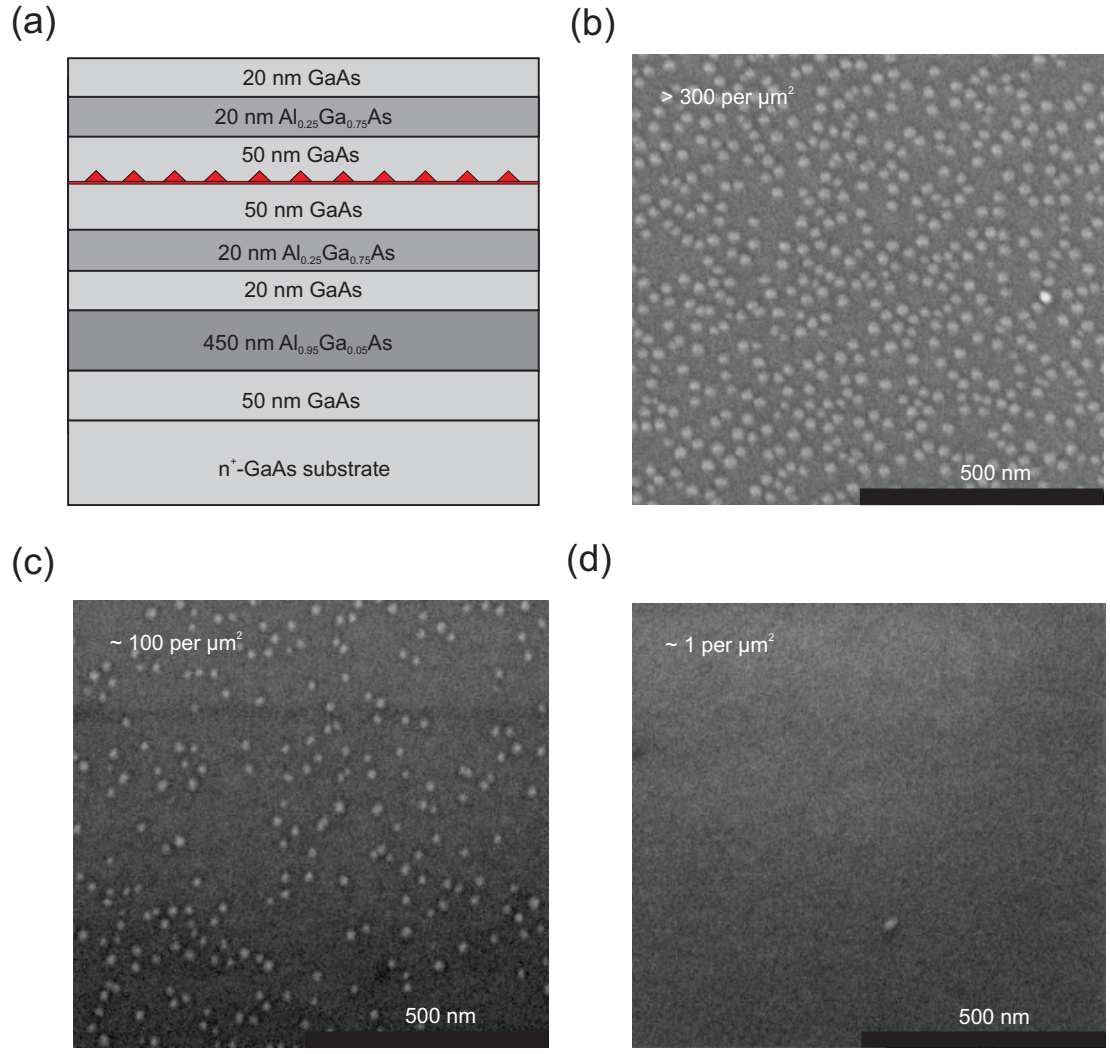

FIGURE 4.1: (a) Scheme diagram of the MBE grown layer sequence with embedded QDs (red triangles). (b)-(d) SEM images of InGaAs QD samples with different QD density. The SEM images have been provided by Ashish K. Rai from Ruhr-Universität Bochum (RUB).

Owing to the geometry of the MBE chamber, usually there is a gradient[2] of the In-atoms reach the wafer, and this leads to a gradient in the QD density in the grown sample. For characterization of PhC cavity modes, we need a sample with a high QD density like that in Fig. 4.1(b), where it provides a broad emission bandwidth. Also, a sample with such density is suitable for experiments where

[2] To achieve quasi-uniform density (high), the wafer is rotated during the growth process.

high optical gain is required, like quantum-dot based laser. A sample with low density, like Fig. 4.1(d) or even little higher, is needed for example for single photon source experiments, as well as coherent experiments like excitonic Rabi flopping in a cavity (see Chapter 7).

4.2 Fabrication of Photonic Crystal Nanocavities

Key fabrication steps for PhC consist of electron beam lithography, dry etching and wet etching. A schematic overview of the fabrication procedures are shown in Fig. 4.2. The fabrication process starts with deposition of a thin layer of SiO_2 (50 nm) on the top of the wafer depicted Fig. 4.1(a). This SiO_2 layer will serve as a hard etch-mask during etching the GaAs slab. This is followed by a layer of a PMMA resist. The PhC structure is then patterned in the PMMA using electron beam lithography technique. Next, the patterned structure is transferred into the SiO_2 layer and subsequently into the GaAs layer by dry etching. Finally, wet chemical etching is used to remove the AlGaAs layer and form a free standing membrane structure. In this section, the fabrication procedure is described in detail.

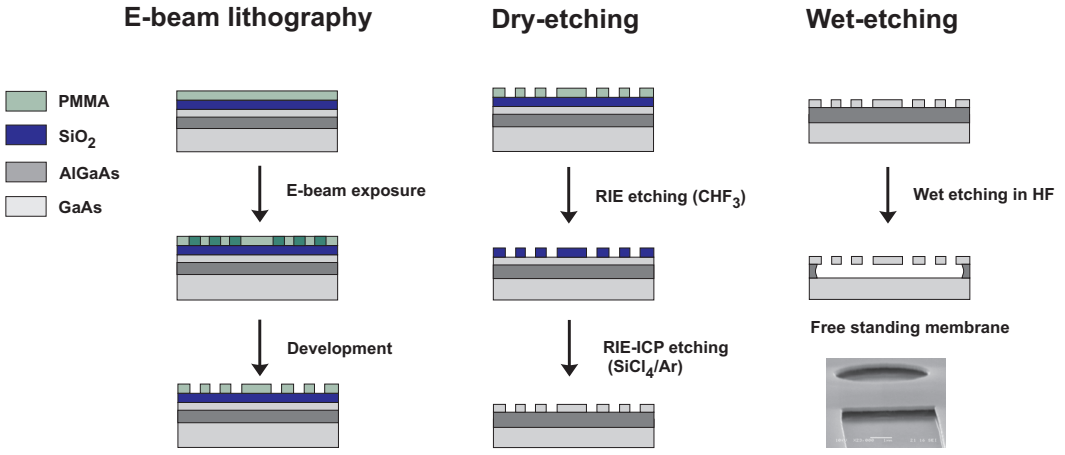

FIGURE 4.2: Schematic representation of the fabrication process of GaAs PhC membrane structures. The SEM image at the right down corner shows a free standing GaAs membrane.

4.2.1 Preparation of SiO_2 Hard Mask

As the selectivity of PMMA over GaAs is high, an additional hard-mask is usually used. Silicon based materials, like SiO_2 (see reference [107]), are excellent mask

materials when using Chlorine based gas in etching. This enables us to have more flexibility in the fabrication process as the hard masks have much lower selectivity over GaAs.

In this work, a hard-mask of about 50 nm of SiO_2 has been deposited by plasma enhanced chemical vapor deposition technique (PECVD) in an Oxford PECVD 80 System. The thickness of the mask was optimized to not etch away during etching in the GaAs. A gas mixture of (2 % SiH_4 and 98% Ar) and (N_2O) was used in this process. The deposition recipe is as follows: SiH_4/Ar flow = 400 sccm, N_2O flow = 400 sccm, process pressure = 1 Torr, RF power = 20 W, substrate temperature = 300 °C. For these conditions, the deposition rate is 75 nm/min.[3]

4.2.2 Electron Beam Lithography

The first step in fabricating PhCs is to define the PhC pattern by using electron beam lithography (EBL). The surface of sample was cleaned using Acetone and Isopropanol solvents, then rinsed using distilled water and baked on a hotplate for dehydration of the surface. In this work, a positive resist (PMMA with molecular weight of 950 K) was spun on the sample at 5000 rpm for 60 seconds, providing about 100 nm thick layer. The sample was then pre-baked on a hotplate at 192 °C for 90 seconds. Then, the PhC patterns have been defined in the resist using electron-beam writing in an SEM (JEOL JSM 5610LV) with 25 kV accelerating voltage and 1.5 pA beam current. Finally, the resist was developed by a 1:3 mixture of Methylisobutylketone (MIBK): Isopropanol for 35 seconds, then rinsed in Isopropanol to stop the developing process.

After the lithography step, the sample was post-baked at 100 °C for 60 seconds, to improve the adhesion of the resist to the sample. To make the PMMA harder, it was blank-exposed to an electron beam with accelerating voltage of 2 kV and about 10 nA beam current. The magnification of the SEM was set to 700X to cover the whole field of PhCs, which is about 200 μm $\times$ 200 μm. It is also important to mention that the electron beam was defocused to ensure the exposure of the area between the scanning lines of the SEM.

A main limiting factor for EBL accuracy is the *proximity effect*. It is caused by secondary electrons that are produced in the resist layer (forward scattering) and the substrate (backscattering). These electrons expose the vicinity of the desired pattern. In the case of PhC structures, the holes at the center receive a higher dose than the holes at the edge, because they have more surrounding holes, i.e., more build up dose. Although it is unavoidable effect, there are several ways to

[3] The thickness was measured by using an elipsometer.

reduce the proximity effect, like dose modulation and pattern biasing. Usually, the former is used in case of PhC pattering where the e-beam dose is gradually increased from the center to the edge of the PhC. Another simple and fairly rapid method to reduce the proximity effect was introduced by K. Hennessy *et al.* [108]. In their work, they wrote extra structures around the PhC pattern to increase the electron dose there, and hence increasing the size of the outermost holes. We have noticed that increasing the PhC lattice periods results in negligible variation in the size of the nearest hole periods around the cavity, which have more effect on the cavity characteristics. In our case, we have increased the number of lattice periods around the cavity, as seen in Fig. 4.3.

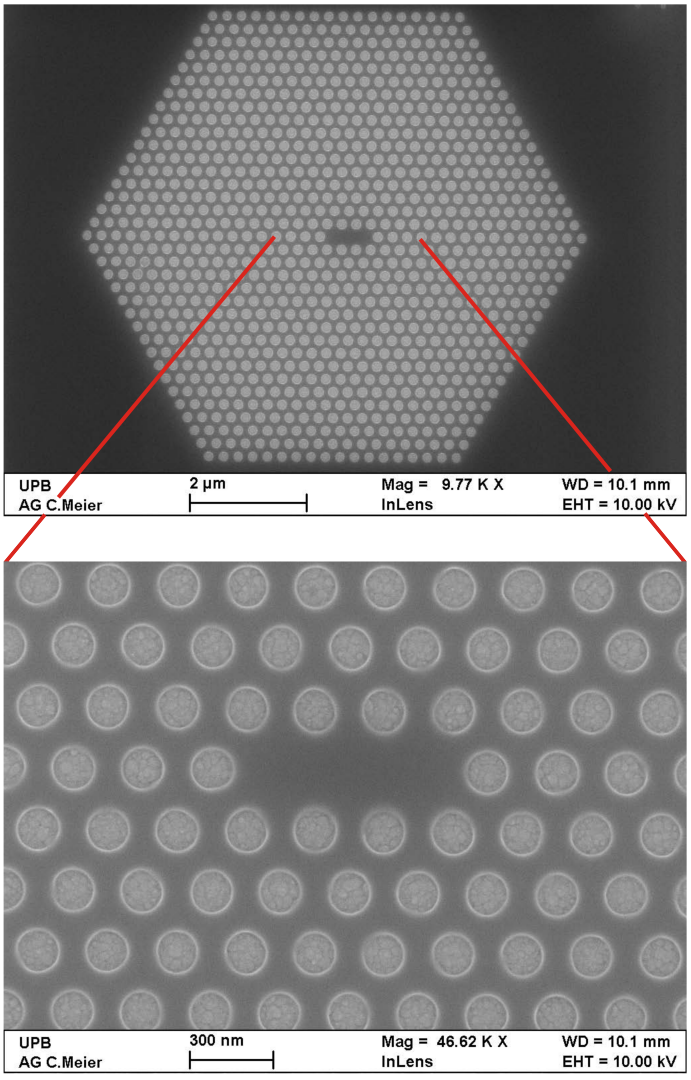

FIGURE 4.3: An SEM image of photonic crystal structure defined in PMMA resist.

The EBL step is of great importance, since it has a major influence on the pattern transfer into the GaAs slab. So, any error will be transferred into the next layers. Figure 4.3 shows an SEM image of patterned PMMA resist after the

EBL step. The PhC structures were defined with high quality. The PMMA resist serves now as a mask for etching the hard-mask SiO_2.

4.2.3 Dry Etching

After defining the PhC patterns in the PMMA resist, reactive ion etching (RIE) was used to transfer these structures into the underlining SiO_2 etch-mask.[4] RIE is one of the most common plasma etching techniques used in semiconductor microfabrication. It is a combination of physical and chemical processes (chemical reaction and physical ion sputtering). Typical configuration of RIE system is shown in Fig. 4.4(a). An RF voltage is applied between two electrodes where one is powered and the other is grounded, which is usually the entire chamber wall. The sample is sit on the RF powered electrode, which operates at a frequency of 13.56 MHz. The RF field ionizes the feeding gas molecules in the chamber, forming a plasma.

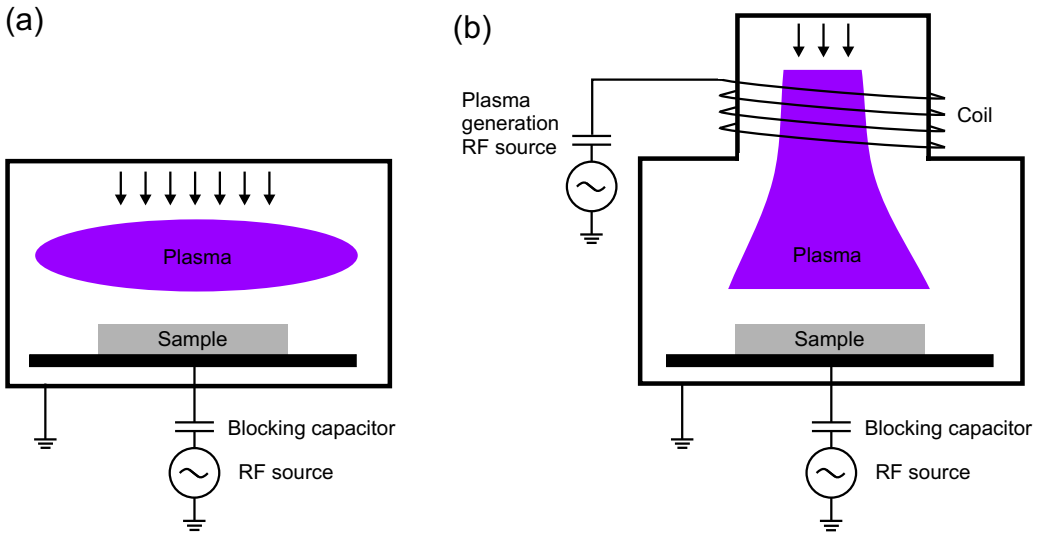

FIGURE 4.4: Schematic illustrations of the operation of (a) reactive ion etching (RIE) and (b) inductively coupled plasma (ICP). The black arrows represent the input of the gases.

The plasma consists of ions, free electrons, free radicals and neutral molecules. In contrast to the ions and the other contents, free electrons are much lighter and can easily follow the AC voltage. In each cycle of the RF field, free electrons are accelerated up and down in the chamber. The electrons which are absorbed by the chamber wall are fed out to ground, since the chamber is earthed. On the other hand, the electrons which are absorbed by the electrode are kept there, because it

[4] The dry etching has been done by using the RIE-ICP system of the group of Prof. Dr. Cedrik Meier.

is coupled to a capacitor, and build up a negative charge. The heavy ions are not able to follow the high frequency field, so the plasma has a higher concentration of positive ions compared to free electrons and hence a positive charge. Owing to the voltage difference between the plasma and the electrode, ions are accelerated toward the electrode where they collide with the sample and sputter the material of the surface (physical etching). Also, the free radicals react chemically with the materials on the surface forming volatile compounds (chemical etching). Mostly, reactive ions follow a vertical path when impinge the sample, providing a highly anisotropic etch profile for optimized etch conditions.

An Oxford Plasmalab 100 Inductively Coupled Plasma Reactive Ion Etching (RIE-ICP) system was used in the RIE process. Etching of SiO_2 is usually done by using fluorocarbon type gases like CF_4 or CHF_3. In this work, we have chosen CHF_3 gas because it provides high selectivity between PMMA and the SiO_2 mask, and the ability to achieve highly directional etching [109]. To enhance the etching process and to get straight sidewalls, Argon gas has been added. Also, the chamber pressure was kept low (3 mTorr) during the etching process in order to achieve anisotropic etch profile. At low pressure, collisions between gas molecules and ions are fewer and thus resulting in a more directional movement of ions toward the sample. Moreover, the volatile products from the surface are moved away quickly, because of the higher pumping speed, and hence improves the etching rate.

In the etching process, some parameters have to be optimized to obtain the desired etch profile (which is normally vertical sidewalls), selectivity and etching rates. The most critical parameters include the gas flow, the chamber pressure, and the RF power. The etching parameters were optimized in our system and the etching recipe is as follows: CHF_3 flow = 8 sccm, Ar flow = 8 sccm, process pressure = 3 mTorr, RF power = 75 W. The SiO_2 mask and the PMMA have roughly the same etch rate 20 nm/min (selectivity 1:1). Following this step, residual PMMA was removed by oxygen plasma cleaning. This step is important because during the etching process polymer can settle on the SiO_2 mask and distort the process and even the etching in GaAs. After etching the PhC structure in the SiO_2 layer, this layer serves as a mask in the GaAs etching step.

Next, etching in GaAs was performed by RIE-ICP process. Here, an RF coil is introduced to produce the plasma, as shown in Fig. 4.4(b). An advantage of ICP in comparison with conventional RIE is the higher plasma density, hence increase the etch rate. In ICP, the ion density is controlled by the RF power applied to the coil, while the ion energy is controlled by the RF power applied to the electrode.

This independent control of the ions energy and density allows for using high ICP-power, while keeping the RF-power relatively low. Consequently, less aggressive etch, high etch rate, and anisotropy are expected.

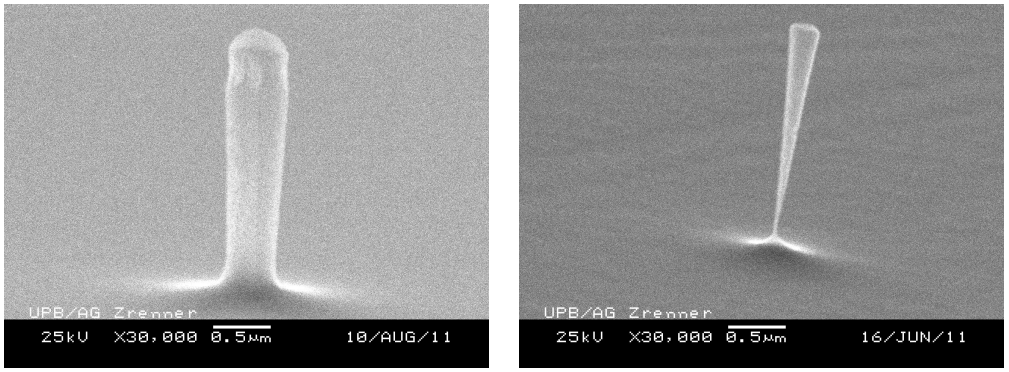

(a) (b)

FIGURE 4.5: SEM images of pillar structures etched by RIE-ICP process (a) with our optimized recipe, and (b) reduced RF power (23 W).

Etching of GaAs is usually carried out by using chlorine-based gases like $SiCl_4$ and Cl_2. However, it has been found that the $SiCl_4$/Ar provide smoother and more anisotropic surfaces [110]. In this work, we have used $SiCl_4$/Ar for pattern transfer into GaAs. The optimal conditions for etching through GaAs slab are: $SiCl_4$ flow = 4.5 sccm, Ar flow = 4.5 sccm, process pressure = 3 mTorr, RF power = 150 W, ICP power = 60 W. The etch rate of GaAs is 575 nm/min, while it is 25 nm/min for SiO_2 (selectivity 23:1).

Different etching profiles can be set by adjusting the etch parameters as shown in Fig. 4.5. Figure 4.5(a) shows pillar structure etched in GaAs with our optimized recipe. The etched profile is highly anisotropic. In Fig. 4.5(b), the RF power was reduced to 23 W, resulting in isotropic etching. This is because the chemical process becomes more dominant at low RF power.

Figure 4.6 shows an SEM micrograph of an H2 PhC microcavity after RIE-ICP etching in GaAs. The PhC pattern is transferred with high quality and the air holes are circular.

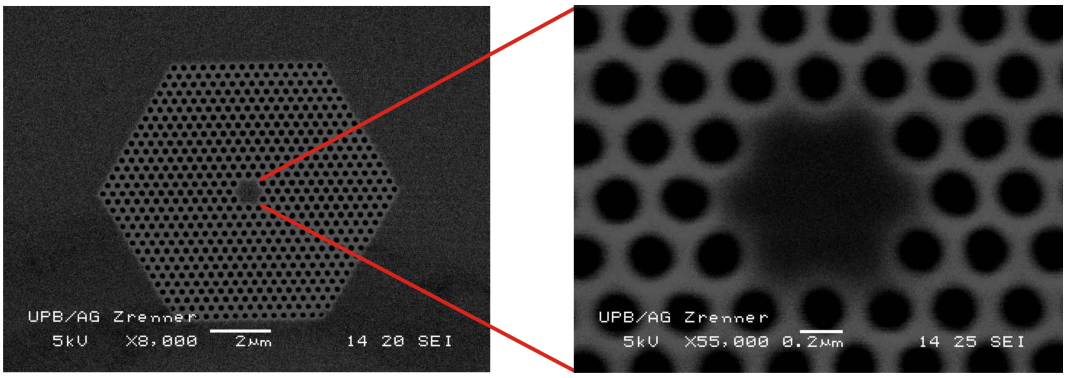

FIGURE 4.6: An SEM image of an H2 PhC cavity with 14 lattice periods etched in GaAs by $SiCl_4$/Ar using RIE-ICP technique.

4.2.4 Selective Wet Etching

The last step in fabricating PhC cavities is to achieve free standing membrane structure. This is done by selectively wet etch the underneath $Al_{0.95}Ga_{0.05}As$ sacrificial layer. Initially, diluted HCl was used to etch the AlGaAs layer. However, we have found that etching in HCl results in non-smooth surface, as shown in Fig. 4.7(b). This reduces the Q-factor of the cavity modes as it introduces optical scattering at the GaAs surface.

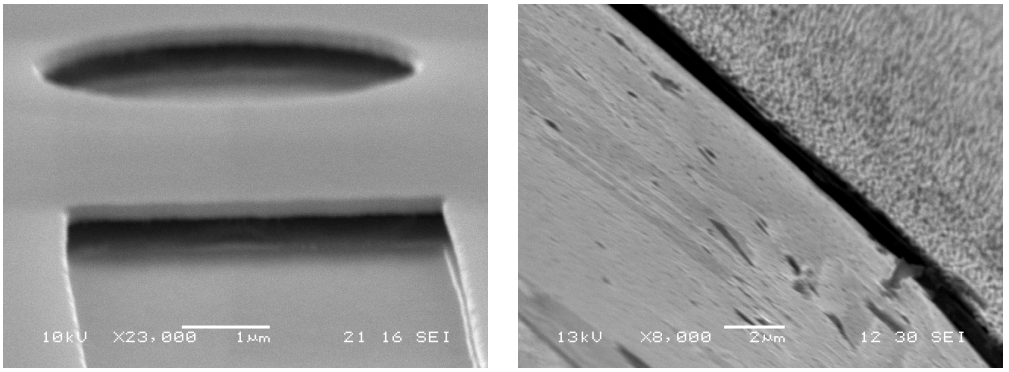

(a) (b)

FIGURE 4.7: (a) An SEM image of a free standing GaAs membrane structure etched in HF. (b) Sample wet-eched in HCl. Note the non-smooth surface in the case of HCl.

Other chemical etchants, like H_3PO_4 and buffered HF, have shown much better results. The latter is usually used to selectively wet etch AlGaAs over GaAs. HF wet etch the AlGaAs layer as well as the residual of the SiO_2 mask, while the GaAs remains unaffected [111]. Figure 4.7(a) shows a sample that was wet etched in diluted HF solution (1%). In contrast to etching in HCl, the surface of GaAs is clearly clean and smooth. The lateral etching rate was estimated to be about 1 μm/min.

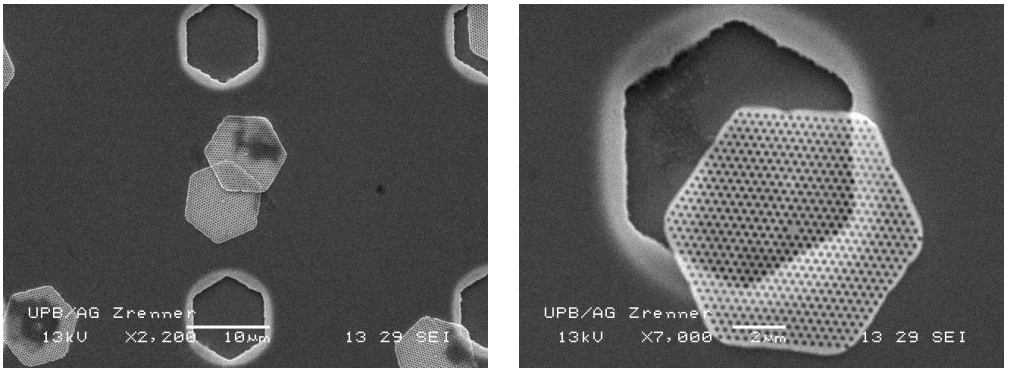

FIGURE 4.8: Sample wet etched in HF acid, showing destroyed PhCs due to the high Al content.

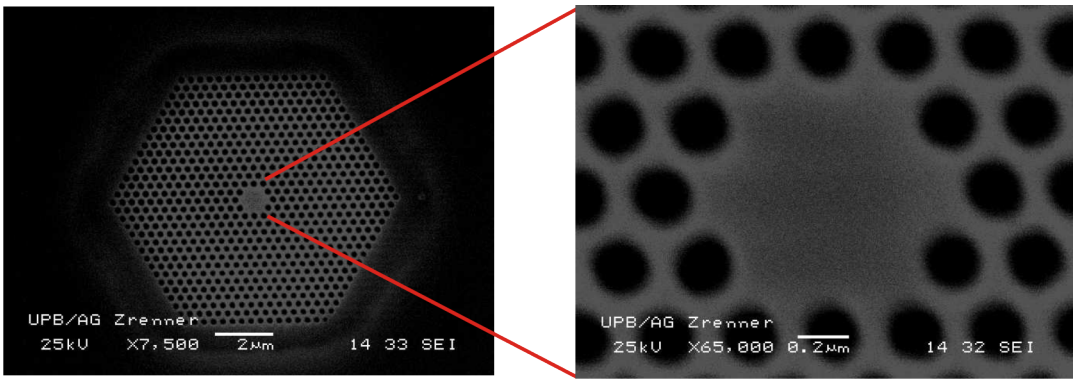

(a)

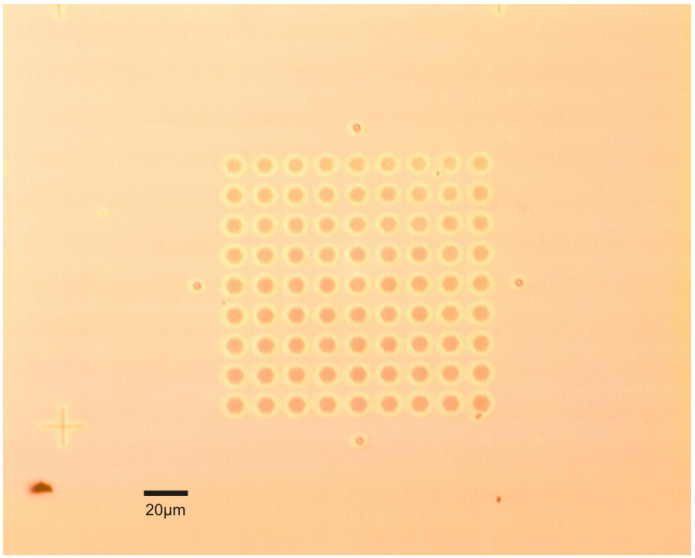

(b)

FIGURE 4.9: (a) SEM micrographs of a fully processed PhC cavity. (b) Microscope image of a field of PhC cavities. The lattice constant a is kept fixed, while r/a ratio is changed in the vertical direction by increasing the exposure time. The bright color (light color) around the structures represents the wet etched areas.

In the wet etching process, most of the PhCs have been collapsed. Figure 4.8 shows a sample after wet etching for 90 seconds, where PhCs are destroyed. Considerable time was spent to solve this issue. We believe that the high Al contents (95%) in the sacrificial layer is probably the reason of this damage. Fortunately, it has been found that we can get rid of this problem by immersing the sample for 10 seconds in HF followed by 30 seconds in DI water. The second step is necessary since it helps to remove the product of the reaction. This cycle was repeated six times to obtain a fully released PhC membrane, and all of the PhCs were survived (not destroyed), as seen in Fig. 4.9(b). The bright color surrounding the PhCs indicate the boundaries of the removed sacrificial layer. Finally, SEM images of a 2D photonic crystal is shown in Fig. 4.9(a), where a precise pattern transfer into GaAs is clearly seen.

Chapter 5

Experimental setup

5.1 Micro-Photoluminescence Setup

All measurements in this work were performed in a liquid helium dewar (4.2 K). The objective lens and the nanopositioner, which together form the low temperature microscope, are enclosed in a stainless steel tube. Before inserting the tube into the dewar, we evacuate it to avoid air condensation. Also, a small quantity of He gas is inserted into the tube to ensure better heat transfer between the low temperature microscope and the liquid He.

The optical characterization of the QD samples and the PhC cavities with embedded QDs has been performed by a micro-photoluminescence (μ-PL) setup. A schematic drawing of our setup is shown in Fig. 5.1. For first characterization, we need a laser with energy above the bandgap of the GaAs in order to investigate the QD states as well as the wetting layer. In our experiments, a HeNe laser ($\lambda = 632.8$ nm, $E = 1.96$ eV) was used for this purpose. For resonant excitations and PLE measurements, a tunable Ti:Sa laser was used (see Section 5.2).

In order to align the laser spot onto the cavity center, the sample was illuminated via the objective lens by a white LED light, whereas the image is monitored by a CCD camera. The sample was mounted at 4.2 K on the top of an XYZ translational stage (nanopositioner), which can operate at low temperatures with an accuracy as high as 250 nm.

The incident laser beam is divided into two parts at the beam splitter. The reflected beam is directed to the sample, whereas the transmitted beam is exploited to record the laser power by a power meter. The laser is focused on the sample by means of a 100X microscope objective lens with a numerical aperture (NA) of 0.75. The spot light has an area of 1 μm^2. The PL signal from the sample was collected by the same objective lens and focused on the entrance slit of the spectrometer[1],

[1] Acton SpectraPro-2500i.

where it dispersed and detected by liquid nitrogen (LN) cooled Si-CCD detector.[2] Also, the PL signal can be coupled into the spectrometer by an optical fiber. This could be suitable for first characterization measurements as it is much easier, but for high resolution, polarization, and PLE measurements the free beam bath is preferred. Besides the PL emission from the sample, the reflected laser from the sample follows the same path. Therefore, a filter is inserted before the spectrometer to block the laser and to avoid high intensity into the spectrometer, which could damage the CCD detector.

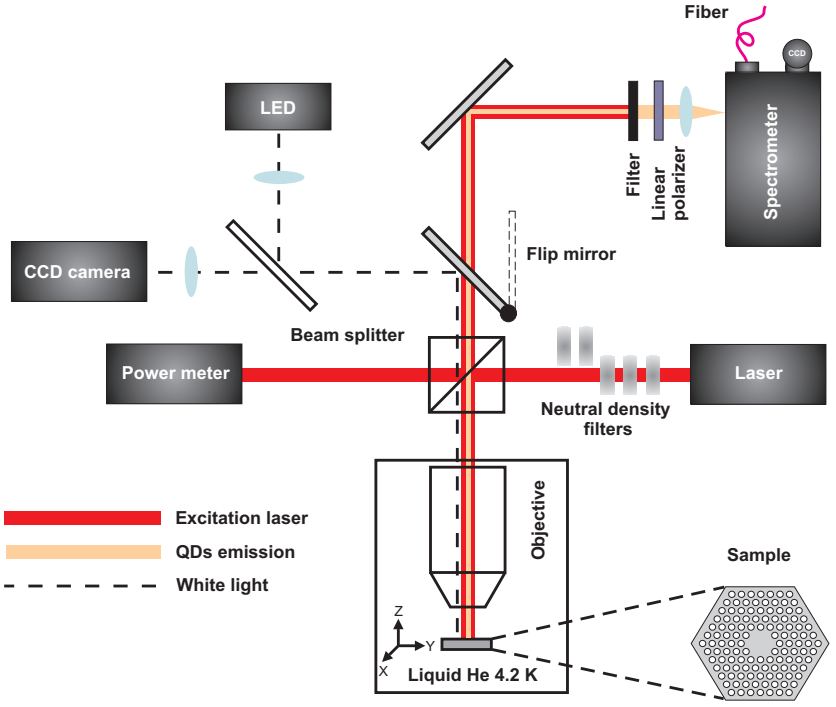

FIGURE 5.1: Schematic illustration of the experimental setup for μ-PL spectroscopy.

The intensity of the laser is controlled by a set of neutral density (ND) filters in front of the laser. For fine tuning of the laser power, a computer controlled ND filter wheel is placed just in front of the ND filters.

The wavelength resolution of the spectrometer with 1200 groove/mm is about 50 pm at $\lambda = 950$ nm. This allows for measuring high-Q cavity modes up to about 20 000. A linear polarizer is placed in the front of the spectrometer for polarization-dependent PL measurements on cavity mode (see Chapter 6).

[2] SPEC-10 400R/LN or SPEC-10 400BR/LN.

5.2 Photoluminescence Excitation Technique

In PLE experiments, the excitation energy is tuned continuously above the QD ground state, while the detection energy is kept fixed to the ground state. When the laser energy matches the resonance of higher states, an exciton is created in the QD, which relaxes rapidly into the ground state and consequently emits a photon. Thus, a peak appears in the PLE spectrum. For PLE experiments and resonant excitations of higher QD states, a commercial Ti:Sa laser[3] was used. Its wavelength is tunable in the range from 700 to 980 nm, covering the whole spectral range of the QD states studied in this work. In the pulsed mode, the system operates with a repetition rate of 80 MHz and pulse width of 1.5-4 ps.

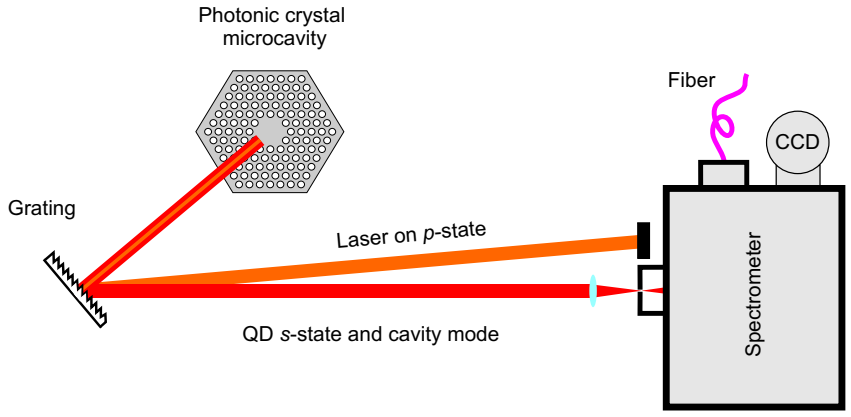

FIGURE 5.2: Schematic diagram for the PLE measurements setup. Note the extra grating placed to separate the excitation laser and the QD luminescence.

In PLE measurements, usually the energy scan range of the laser starts by few meV above the ground state and cover the higher energy states and the wetting layer. Thereby, the monochromator cannot separate the excitation laser from the PL signal efficiently, and too much stray light will be generated in the spectrometer. Therefore, an effective stray light suppression is necessary. This can be achieved by using an extra grating just before the spectrometer, as depicted in Fig. 5.2. The PLE measurements performed by using this setup will be discussed in Section 7.3.

5.3 Sample Temperature Control

As mentioned above, the sample temperature in liquid helium is 4.2 K. To perform temperature dependent measurements or to tune the energy of the QD exciton relative to a cavity mode, a heating mechanism is needed.

[3] Coherent Mira optima 900-D.

In our experiments, we used a copper plate to control the temperature of the sample. The copper is chosen due its high thermal conductivity. The sample was mounted on a ceramic plate on the top of the copper plate. The system was heated by two 22 Ω parallel SMD resistors below the copper plate, while the temperature is measured by using a silicon diode (LakeShore DT-670B-SD), as shown in Fig. 5.3. For more details see reference [112].

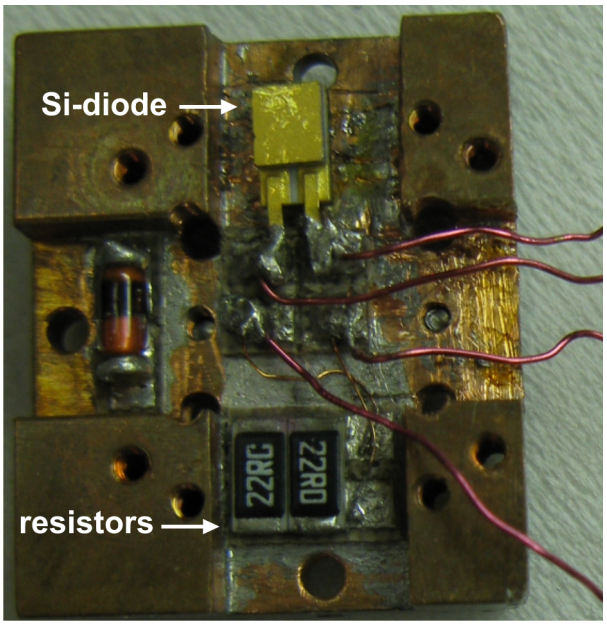

FIGURE 5.3: A backside view of the sample carrier showing the components of the heater.

Chapter 6

Characterization of H2 Photonic Crystal Nanocavities

In this chapter, the design and characterization of H2 PhC cavities are discussed. Section 6.1 includes the cavity design using the Finite-Difference Time-Domain method. In Section 6.2, the Q-factor improvement by shifting the nearest-neighbor air holes around the cavity is described. The characterization of the cavities by using photoluminescence technique is discussed in Section 6.2. Also, polarization-dependent measurements have been performed to identify the cavity modes.

6.1 Cavity design

The first step in designing PhC cavities is to calculate the photonic band structure. The photonic band gap (PBG) must match the resonance frequency of the emitters to be embedded in the cavity. For this purpose, we used the block-iterative frequency-domain method to calculate the photonic band structure of a triangular lattice PhC [113]. The result is illustrated in Fig. 6.1(Left). For our specific choice of parameters (thickness $t = 0.72a$, and $r = 0.25a$) [114], the PBG spans the spectral range between 0.24 and $0.28a/\lambda$, which corresponds to $890 - 1040$ nm. The emission spectrum of the QD ensembles used in this work extend from 910 nm to 990 nm (see Fig. 6.1(Right)), which is located completely in the PBG region.

In this work, PhC cavities with various geometries have been investigated. The cavity region of each type has been engineered to improve the Q-factor. In this chapter, we consider only H2 cavity, which is formed by omitting seven holes at the center of a triangular lattice PhC. The results of other geometries (H1, L3, and L5) are discussed briefly in Appendix A.

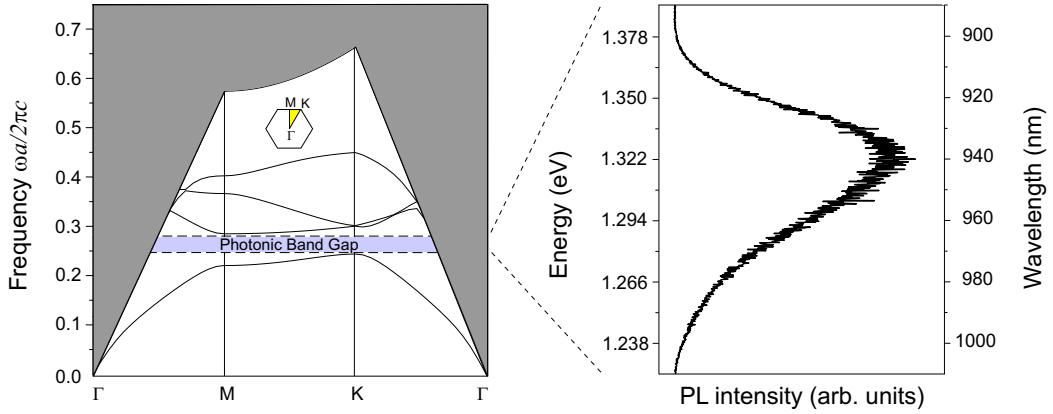

FIGURE 6.1: (Left) Photonic band structure of a PhC slab with $r = 0.25a$ and thickness $t = 0.72a$. The refractive index of GaAs was set to 3.4 [29] in the calculation. (Right) Typical PL spectrum of an InGaAs QD ensemble. The emission of the QDs overlaps spectrally with the PBG.

We chose to investigate the H2 cavity [30, 115–117], because it has the potential to offer high Q-factors for larger defect regions. This will bring more degrees of freedom for future designs of functionalized defect regions, for example with electric contact stripes to the center of the cavity region. Moreover, as we will see in the next section, this type of cavities support modes with energy difference comparable to that between p- and s-shell of a QD. Thus, using H2 would be helpful for quasi-resonant excitation of a QD exciton via p-shell which is in-resonance with a higher-order mode, while the exciton is in-resonance with a lower-order mode. Of course, this relies on chance to find such situation. Figure 6.4(b) shows an SEM image of a fully processed H2 cavity with the parameters as discussed above.

Simulations on H2 cavities were performed by a 3D Finite-Difference Time-Domain (FDTD) method, using a commercial software package (Lumerical FDTD Solutions) [118]. In the calculation, we used the following parameters: lattice constant $a = 250$ nm, the grid dimensions $\Delta x = \Delta z = a/15$ and $\Delta y = \left(\sqrt{3}/2\right)\Delta x$, simulation time $t_{sim} = 1$ ps, the dielectric constant of GaAs $\epsilon = 11.56$ ($n = 3.4$). We include a free space volume of thickness $2a$ above and below a membrane of 14 lattice periods. The simulation volume was surrounded by perfect matching layers (PML).

A number of dipole sources are positioned throughout the cavity to excite its modes. These sources are chosen to be magnetic dipoles which inject a short TE-polarized pulse, with a broadband $(850 - 1100)$ nm. Radiations with energy matching the cavity resonances will be coupled into them and decay slowly, while radiations with other frequencies will be scattered and rapidly exit the simulation volume. In order to get the time domain data, the electric field inside the cavity

is monitored as a function of time by introducing time monitors. The frequency response at each time monitor is obtained by the Fourier transform of the time domain data. After running the program and identifying the spectral position of the cavity resonances, we set the resonant frequency values into the frequency domain monitors and run the program again to calculate the mode profiles. By exploiting the symmetry in the z-direction through the middle of the simulation region, the simulation time is reduced by a factor of two.

Due to the C_{6v} symmetry of the triangular lattice, some of its cavity modes are expected to be doubly degenerate. Actually, our calculation confirms that as shown in Fig. 6.2. According to the calculations, H2 with our parameters supports eight modes. Four of them are non-degenerate and the others are degenerate modes, as depicted in Fig. 6.2. Based on their mode shape, they are called hexapole (Fig. 6.2(a)), dipole-like modes (Figs. 6.2(b, c), (e, f), (h, i), and (k, l)), whispering-gallery-like mode (Fig. 6.2(d)), and monopole-like mode (Fig. 6.2(g)).[1]

The non-degenerate and doubly-degenerate modes can be distinguished by using the symmetry boundary conditions.[2] When no symmetry is applied, the x minimum and y minimum boundaries are set to PML. Non-degenerate modes appear for only one combination of symmetry boundary, while degenerate modes appear for two combinations of symmetry boundaries. Besides that, using symmetry conditions is necessary to view the doubly-degenerate modes, since only one of the degenerated modes will be obtained when no symmetry condition is applied.

We will especially consider the mode in Fig. 6.2(g) for our investigations, as it was found to respond very well for Q-factor optimization procedures. Furthermore, this mode has energy separation with the doubly-degenerate mode (Figs. 6.2(e) and (f)) that could allow for high efficiency quasi-resonant pumping [119]. For simplicity, we call this mode as M-mode and the nearest degenerate modes as D1 and D2.

In order to experimentally test our theoretical calculation and to ensure that M-mode lies spectrally in the area of interest, we fabricated cavities with lattice constant of 250, 260, and 280 nm, while the r/a ratio was kept to 0.25. Figure 6.3 shows PL spectra for the M-mode measured at 4.2 K by using the μ-PL setup discussed in Chapter 5. By increasing the lattice constant, the M-mode redshifts from 925, to 944 and to 978 nm. The results in Fig. 6.3 demonstrate that a proper choice of the lattice constant allows for spectral mode tuning into the desired frequency.

[1] The mode in Fig. 6.2(j) has no counterpart in literature, so we call it simply mode *j*.
[2] This condition is set to symmetric or anti-symmetric.

In our case, we chose lattice constant of 250 nm for two reasons. First, it was experimentally observed that this value for lattice constant results in higher Q in comparison with $a = 260$ and 280 nm. Second, when optimizing the Q-factor (which will be discussed in the next section) the M-mode is redshifted (see Fig. 6.7(a)). Therefore, to let the mode locate spectrally at the center of the QD emission, we should start the optimization process by an unmodified cavity with a higher energy mode M. On the other hand, M-modes for lattice constant of 260 and 280 nm will be shifted far from the center of the QD emission.

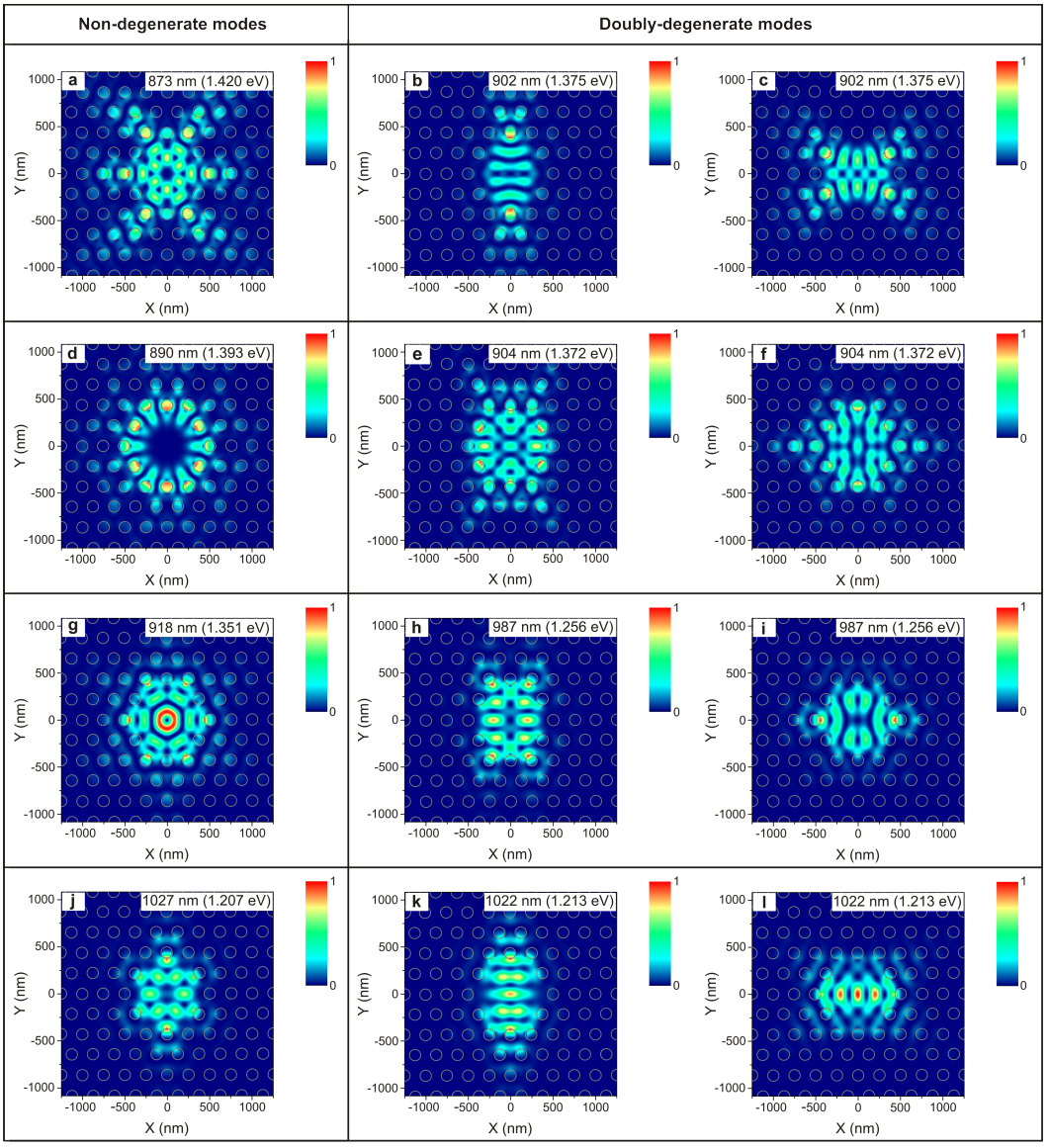

FIGURE 6.2: Calculated electric field intensity profiles of H2 cavity modes with $a = 250$ nm, $r = 0.25a$, and $t = 0.72a$.

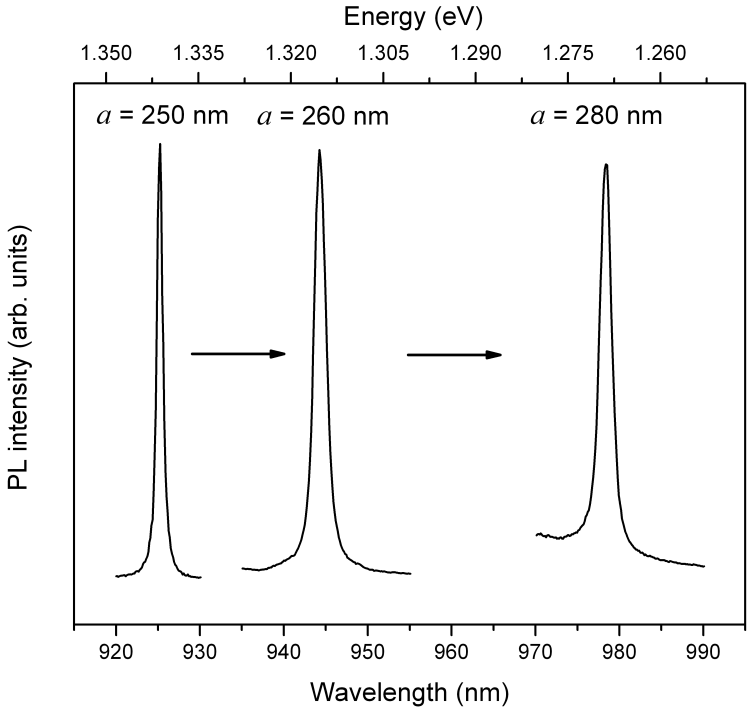

FIGURE 6.3: Measured PL spectra for H2 cavities with lattice constants 250, 260, and 280 nm. The cavity mode M redshifts from 925, to 944 and to 978 nm with increasing the lattice constant.

6.2 Improvement of the Quality Factor

In PhC cavities, Q-factor can be significantly increased without a remarkable change in the modal volume. This is desirable for example to achieve high Purcell factor as it is proportional to Q/V_m, and for high coupling strength as $g \propto Q/\sqrt{V_m}$ (see Section 2.9). In the optimization process, usually the position and/or the size of the inner air holes surrounding the cavity are modified.[3]

As discussed in Chapter 3, by increasing the number of lattice periods surrounding the cavity, the in-plane losses are drastically suppressed. Therefore, the radiation loss into the vertical direction is the main loss mechanism. In order to increase the Q-factor of PhC cavities, these radiation losses need to be suppressed. One method to improve the Q is what is called the *cancellation mechanism* [31, 101, 120]. In this method, the lowest-order term (usually the dipole term) in a multipole expansion of the far-field radiation is eliminated by an appropriate cavity design. It is important to note that the mode pattern within the slab is almost unchanged by this kind of tuning, while the far field pattern is drastically altered [22].

[3] Depending on the profile of the electric field, not only the tuning of the inner holes can increase the Q, but also the adjacent lattice periods.

Another way to improve the Q-factor by keeping the modal volume almost unchanged is called the *gentle confinement method* [25]. In this method, the abrupt decrease in the envelope of the electric field at the cavity edge is considered to generate high field components inside the light cone. Therefore, it is possible to reduce radiation losses by engineering the region around the cavity (usually the nearest-neighbor holes) such that the spatial variation of the envelope at the cavity edge is terminated smoothly. In other words, reducing the overlap between the mode and the air regions minimizes the scattering at the cavity edge.

Here, we optimize the geometry of H2 cavity to increase the Q of the M-mode. By looking carefully at the electric field profile of the M-mode (Fig. 6.2(g)), we see that it is not perfectly matching the six-fold symmetry of the triangular lattice. The field penetrates all of the inner air holes, with higher intensity for holes at $(0, \pm\frac{\pi}{3}, \pm\frac{2\pi}{3})$ with respect to the x-axis. This distribution is not preferred as it leads to high scattering at the cavity edges. In order to reduce the scattering at the cavity edge, we have to reduce the overlap with air. Our idea to improve the Q of the M-mode was to shift the position of the inner holes of the cavity outwards radially along the lines of the lattice symmetry. A scheme diagram of the holes displacement is depicted in Fig. 6.4(a).

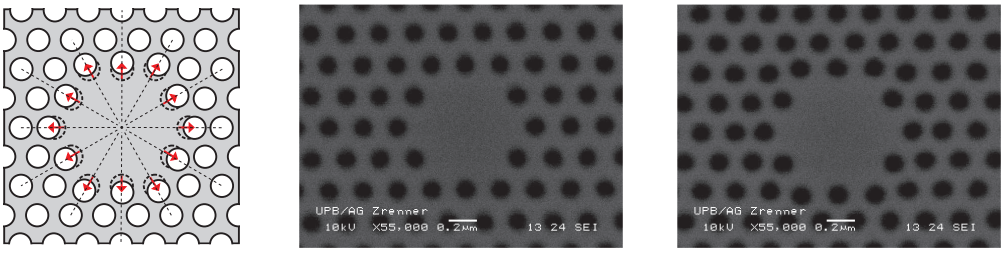

(a) (b) (c)

FIGURE 6.4: (a) Schematic diagram of a modified H2 PhC microcavity. The tuning of the cavity is achieved by shifting the position of the nearest-neighbor holes away from the cavity center radially along the lines of the lattice symmetry (in the direction of the dashed-lines). SEM images of (b) an unmodified H2 cavity and (c) a cavity with air holes shift of $s/a = 0.12$.

The effect of the shift on the field pattern is shown in Figs. 6.5(a), (c), and (e). The field intensity has less overlap with the air holes when $s/a = 0.18$ (Fig. 6.5(c)), and consequently less light scattering expected in the vertical direction. By further displacements, for example $s/a = 0.28$ (see Fig. 6.5(e)), the field penetrates into the second lattice periods. This delocalization of the mode reduces the in-plane confinement, and thus the Q drops to low values.

Another way to understand the influence of the air holes shift on the Q-factor is to investigate the electric field in Fourier space. The Fourier transform (FT)

of the electric field intensity is analyzed just above (at a distance of $t/4$ above the surface of the membrane, where t is the slab thickness) and parallel to the slab [27]. Figure 6.5 shows the electric field distribution and the corresponding FT spectra for different air holes shift. The dashed white circles at the center of the FT spectra in Figs. 6.5(b), (d), and (f) indicate the light line inside which electric field components contribute to the out-of-plane radiation. The higher the intensity of the field components inside the light line the larger the radiation loss of that mode. Thus, in order to increase the Q, those components inside the leaky region need to be minimized.

As shown in Fig. 6.5(b), the FT spectrum contains considerable field components within the light cone. This means that a large out-of-plane radiation is present, and therefore a low Q is expected. By a careful and an appropriate displacement of the air holes (as in Fig. 6.4(a)), the components in the leaky region are severely reduced when $s/a = 0.18$ (see Fig. 6.5(d)) in comparison with the unmodified case. Further shifts increase the field components in the light line, as shown in Fig. 6.5(f), and the Q is supposed to decrease again.

Now, we investigate the effect of air holes displacement on the degenerate dipole-like modes at 904 nm (D1 and D2) (Figs. 6.2(e) and (f)). Only one of the degenerate modes at 904 nm (Fig. 6.2(e)) will be considered here (D2), as the other is likely to follow the same behavior. The electric field intensity in real and Fourier space for D2 with s/a =0.0, 0.18, and 0.28 are presented in Fig. 6.6. For the unmodified case, a noticeable amount of the field components appear inside the light line. In contrast to the M-mode, shifting the inner holes by $s/a = 0.18$ has almost no remarkable influence on the field components in the leaky region (Figs. 6.6(b) and (d)). Therefore, the Q is not expected to increase significantly. On the other hand, further increase of the shift decreases slightly the field components inside the leaky region as shown for $s/a = 0.28$ in (Fig. 6.6(f)).

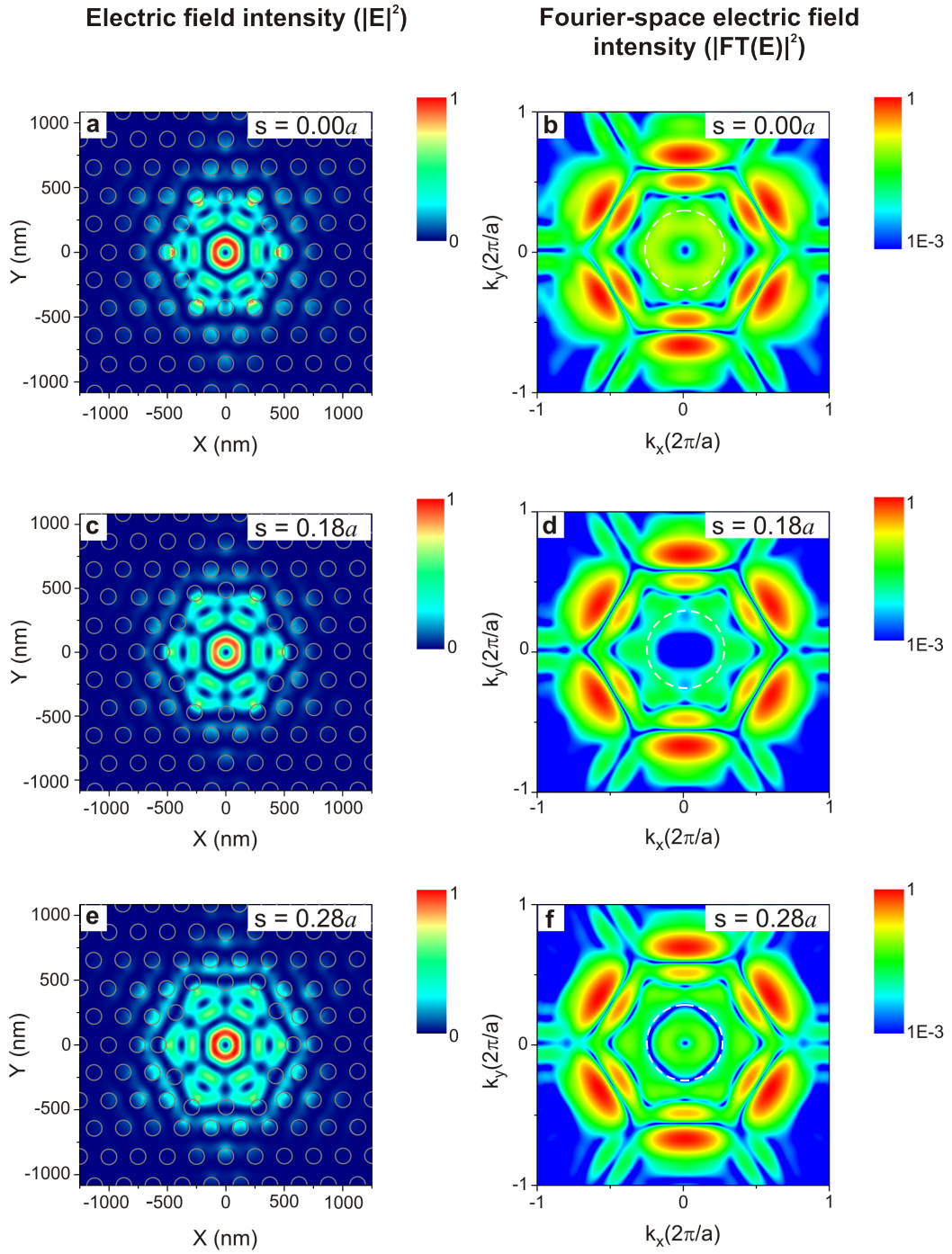

FIGURE 6.5: Electric field intensity profiles of the M-mode with air holes shift of (a) zero, (c) $0.18a$, and (e) $0.28a$. The corresponding 2D Fourier transform of the electric field intensity $\left(|FT\,(E_x)|^2 + |FT\,(E_y)|^2\right)$ is plotted in graphs (b), (d), and (f). The dashed white circles in graphs (b), (d), and (f) represent the light cone boundary (the light line), which is defined by $k_x^2 + k_y^2 = (\omega/c)^2$. Note the reduction of the wavevector components inside the light line for shift of $0.18a$ (graph (d)).

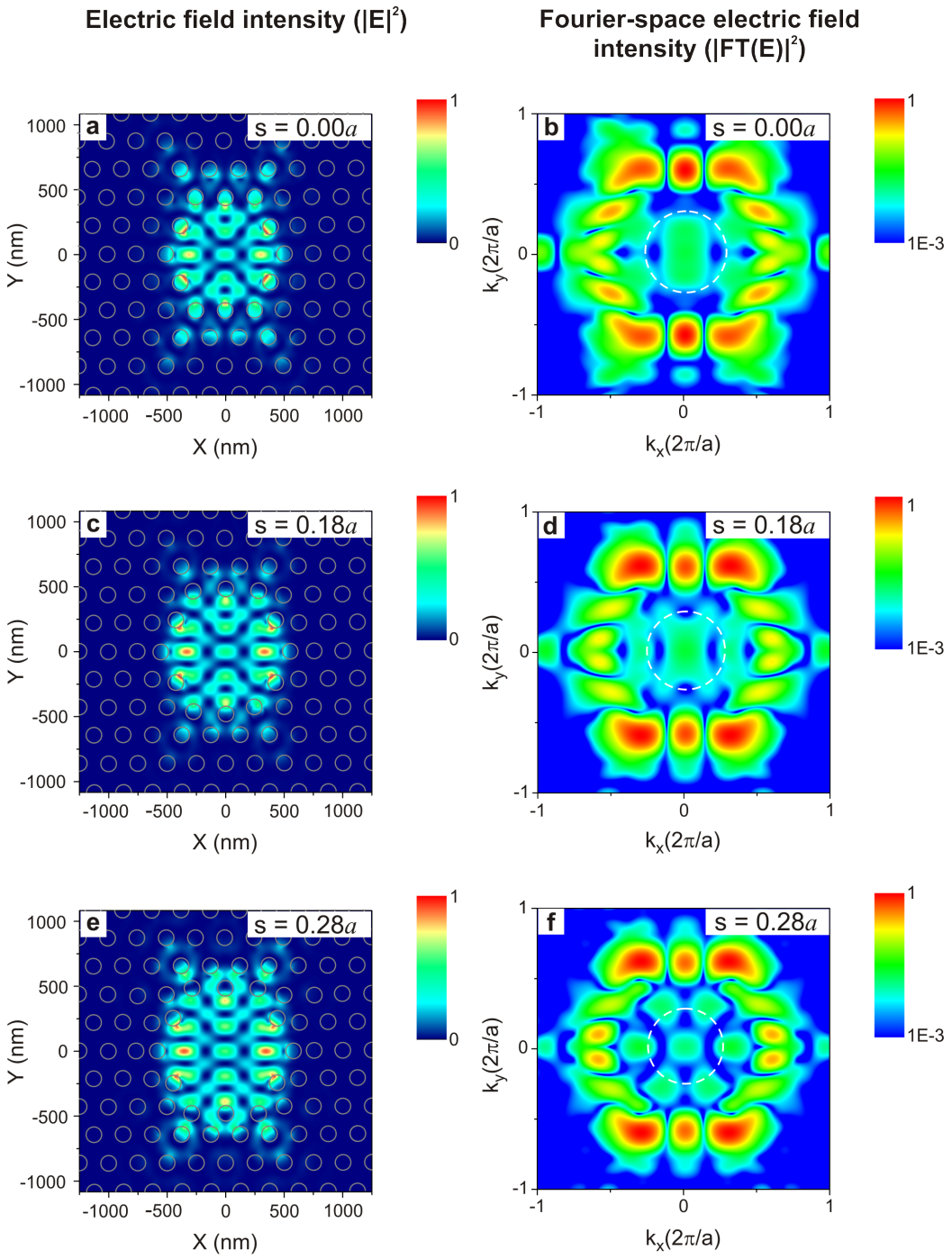

FIGURE 6.6: Electric field intensity profiles of the degenerate dipole-like mode D2 with air holes shift of (a) zero, (c) $0.18a$, and (e) $0.28a$. The corresponding 2D Fourier transform of the electric field intensity $\left(|FT\,(E_x)|^2 + |FT\,(E_y)|^2\right)$ is plotted in graphs (b), (d), and (f). The dashed white circles in graphs (b), (d), and (f) represent the light cone boundary (the light line), which is defined by $k_x^2 + k_y^2 = (\omega/c)^2$. In contrast to the M-mode, the wavevector components is still large for shift of $0.18a$ (graph (d)), while they are minimized for higher shift of $0.28a$ (graph (f)).

6.3 Experimental Results and Discussion

Based on the calculation results, we fabricated H2 cavities with various air hole shifts. The GaAs membrane structure contains a QD ensemble at the center, which serves as a broadband emitter to excite the cavity modes (see Chapter 4). Figures 6.4 (b) and (c) show typical SEM images of an unmodified H2 cavity and a modified cavity with air holes shift of $s = 0.12a$, respectively. The cavities are surrounded by 14 lattice periods (not shown here) to enhance the in-plane confinement, and consequently obtain higher Q-factor. The optical measurements were performed at 4.2 K using the μ-photoluminescence (μ-PL) setup discussed in Chapter 5. The pump power density was set to 2.5 KW/cm^2 (25 μW).

Figure 6.7(a) shows the PL spectra of H2 cavity with various air holes shift from zero to $0.28a$, with a lattice constant of 250 nm and $r = 0.25a$. The emission of the QDs is enhanced on-resonance with cavity modes and suppressed for the off-resonance case due to the Purcell effect [121]. We identified five resonance peaks for the unmodified H2. The other modes (Figs. 6.2(a), (d), (h), (i), (j), (k), and (l)) are not observed in the PL spectrum for the unmodified cavity since their spectral positions lie out of the QD emission range. We have demonstrated that these peaks are cavity modes by measuring and comparing equivalent cavities on the same sample.

The lower PL spectrum in Fig. 6.7(a) shows the mode structure for an H2 cavity. The measured spectrum agrees well with the calculated resonance frequencies (see Fig. 6.2). As mentioned above, M stands for the monopole-like mode (Fig. 6.2(g)), whereas the D1 and D2 refer to the degenerate mode at 904 nm (Figs. 6.2(e) and (f)). According to our calculation, the resonant peak at 925 nm corresponds to the M-mode (Fig. 6.2(g)), whereas the two broader peaks at 906 nm and 908 nm are identified as the degenerate modes at 904 nm (Figs. 6.2(e) and (f)).

By looking carefully at the field profiles in Fig. 6.2, D1 and D2 has an orthogonal feature, whereas M-mode shows no distinguished polarization dependence. The dipole degeneracy is broken due to slight imperfections in fabrication, which are caused by slightly different scaling of the x- and y-direction in the electron beam lithography system. This assignment is consistent with our spectroscopic data, which show that the modes D1 and D2 are orthogonally polarized with high polarization degree, whereas the mode M exhibits almost no polarization dependence (Fig. 6.8). A linear polarization degree up to 0.72 has been realized for the D2 mode, where the polarization degree is given by $(I_{max.} - I_{min.})/(I_{max.}+_{min.})$. The calculated results for the spectral position as well as the polarization behavior are in good agreement with our experimental findings.

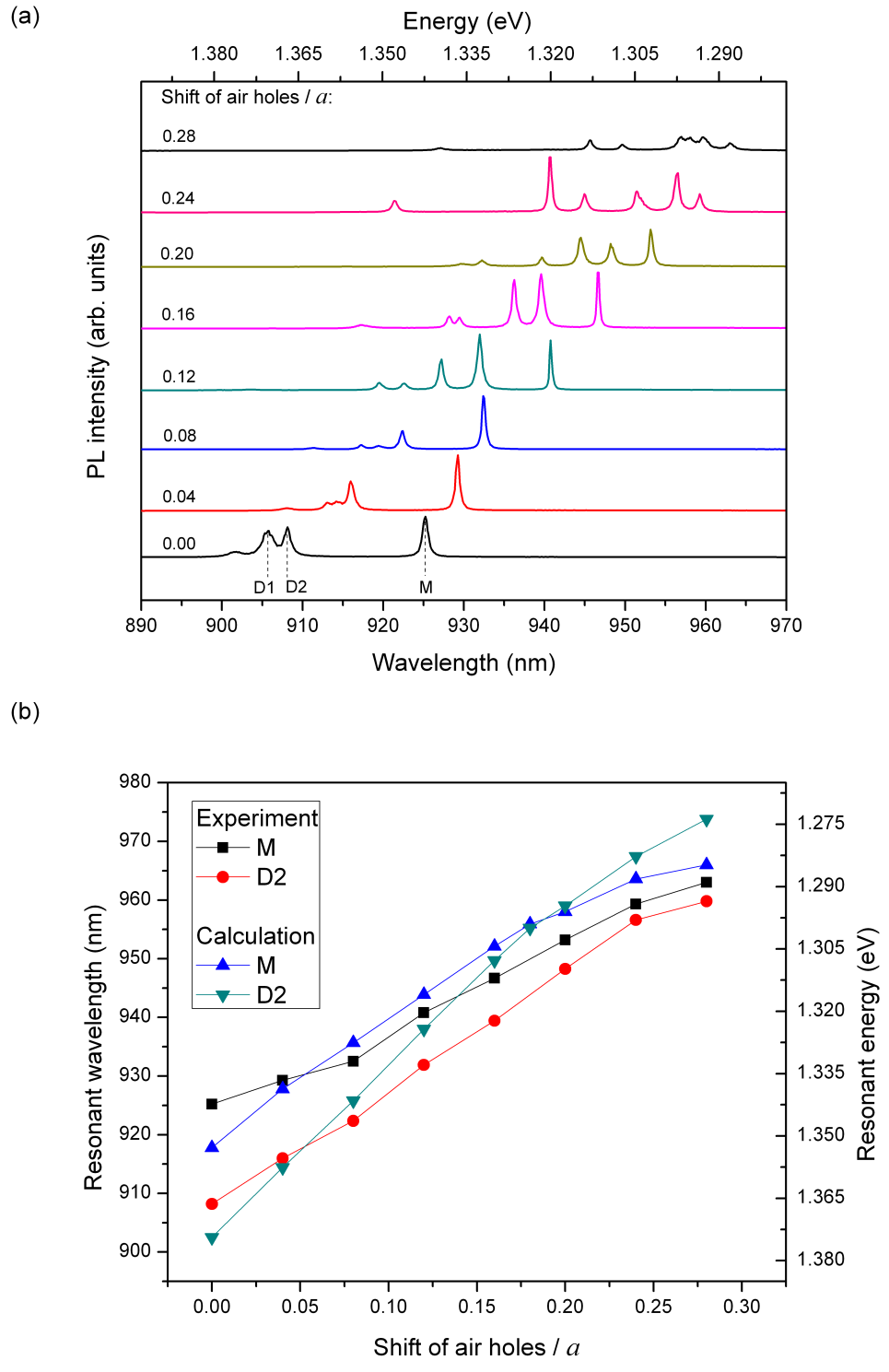

FIGURE 6.7: (a) Measured PL spectra of H2 PhC microcavities with different inner air holes shifts s, described by the parameter s/a. (b) Resonant wavelength position of the high-Q mode (M) and dipole-like mode D2 versus s/a.

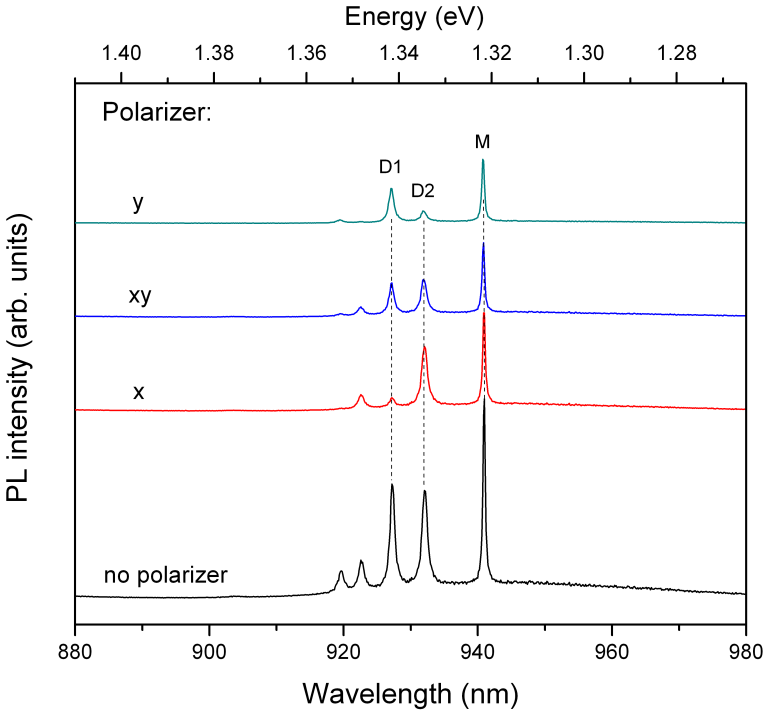

FIGURE 6.8: Polarization-dependent PL spectra of a modified H2 cavity with $s/a = 0.12$. The spectrum was taken without polarizer, and with polarizer at different orientations. D1 and D2 are dipole-like modes.

The small peak at 902 nm is one of the higher order dipole-like modes (Figs. 6.2(b) and (c)), while the other mode overlaps with D1 at 906 nm (lower spectrum of Fig. 6.7(a)). When shifting the inner holes, D1 and the other mode become separated as seen from the upper spectra, for example when $s/a = 0.12$. Therefore, since the D1 mode is more spectrally separated from the higher order dipole-like mode, the polarization dependent measurements were performed on a modified cavity ($s/a = 0.12$) and not the original H2. For displacement of $0.16a$, a new mode appears in the spectrum at 917 nm. According to our calculation, we ascribe this mode to a whispering-gallery-like mode (Fig. 6.2(d)).

With increasing the shift of the inner holes s, all resonances experience a red-shift, which can be attributed to the increase of the effective cavity size. This is an evidence that these resonances are the cavity modes. In Fig. 6.7(b), we present the calculated and measured wavelength of the cavity modes as a function of the tuning parameter s/a. The experimental results are in good agreement with our calculations. The dipole-like modes D1 and D2 show stronger shift as compared to the M-mode (only D2 is plotted here). Analyzing a large number of geometrically equivalent cavities, we found an equivalent behavior for the shifts of the different mode positions. Mode M appears to be less affected by residual imperfections

induced by processing, whereas the dipole-like modes D1 and D2 show a more pronounced scattering in spectral position. The reproducibility of the M-mode resonance position for different processing batches is ±2 nm and even less than 1 nm for cavities within one batch.

Next, we plot the calculated and measured Q-factors of H2 cavities as a function of s/a for different air holes shifts from zero to $0.28a$. The theoretical Q values obtained from the decay time of the energy stored in the cavity, while the measured Qs are given by equation (3.8) ($\omega_0/\Delta\omega$). The results are shown in Fig. 6.9.

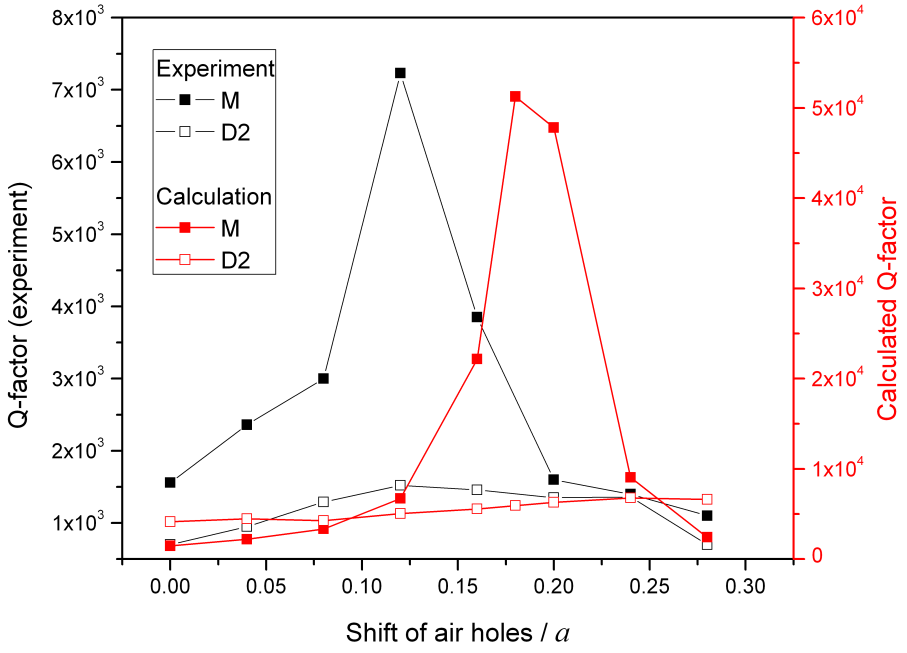

FIGURE 6.9: Calculated and measured Q-factors of the M and D2 modes as a function of the displacement of the air holes (s/a). A maximum Q value of 7230 has been realized for the M-mode. The measurements have been performed with excitation power of 6μW.

The calculations show that the Q-factors of the M-mode increase from 1500 to more than 50 000 by displacement of $s/a = 0.18$. Further displacements lead to a reduction in the Q due to the increase of the field components inside the leaky region. The measured Qs are plotted in the same figure. As the shift of the inner holes s is increased, the Q-factor gets rapidly enhanced and reaches a maximum of more than 7000 for $s/a = 0.12$ (resonance at 940 nm for this case), before it decreases again. The highest obtained Q (7230) is five times higher than that of the unmodified structure (1500).

The experimental values of the Q were lower than the calculated ones, and the highest Q occurs at lower air holes shift. The difference between the experimental

and theoretical Q-factors can be attributed to two reasons. First, the fabrication imperfections, like the slight tilt of the holes sidewalls and the surface roughness of the GaAs slab. Second, the absorption of the QD ensemble, as these cavities are embedded with high QD density [122]. Nevertheless, the experimental results follow the same behavior as the calculation.

For the D2 mode, the calculations show that the Q factor is slightly increased with increasing the holes shift. However, the experimental results show that the Q increases from around 700 to 1300 by displacement of $0.08a$. For shifts between 0.08 and $0.24a$, we observe almost no change in the Q-factor. By further displacements (i.e., $0.28a$), the Q drops again. The different behavior between the calculation and experiment at $0.28a$ is probably originates from the slight different scaling in the x- and y-direction of the lithography system, as mentioned earlier. Also, at this large shift, some holes are very close (or even connected) to the adjacent holes, and therefore interrupting the in-plane mode localization.

It is important to note that the chosen modifications affect the Q-factor (Fig. 6.9) and the resonant frequency (Fig. 6.7(a)), but not the general ordering and symmetry of the mode structure.

Chapter 7

p-Shell Rabi Oscillations of a Quantum Dot in a Cavity

When a two-level system is excited resonantly by a strong light field, a periodic oscillation in the population between these levels can occur. This oscillatory behavior is known as *Rabi oscillations* and requires coherence of the two-level system. Rabi oscillations are one of the most fundamental phenomena observed in two-level system and have no counterpart in classical physics. They have been observed in many systems like atoms [123], free-carrier transitions in bulk [124], excitonic transitions in quantum wells [125] , as well as single QDs [72, 126, 127]. Besides its importance for fundamental research, Rabi oscillations correspond to a qubit rotation in single QDs, which is important in the context of quantum information processing.

In this chapter, we investigate the p-shell Rabi oscillations of a single QD in a PhC cavity. The system was characterized by PL and PLE techniques, and the coherent experiments were performed by using a ps-pulse laser.

7.1 Sample Preparation

To perform coherent experiment on single QDs, we need a sample with low QD density (as that shown in Fig. 4.1(d) or even slightly higher). This can be achieved by wafer mapping. The wafer is scanned at 4.2 K by the PL technique, and then the desired position with only small number of peaks is chosen. A PL spectrum for the sample used in this chapter is shown in Fig. 7.1. The measurement was performed at relatively low power (0.8 μW), to avoid higher states excitation. The sharp resonance lines are attributed to single InGaAs QDs.

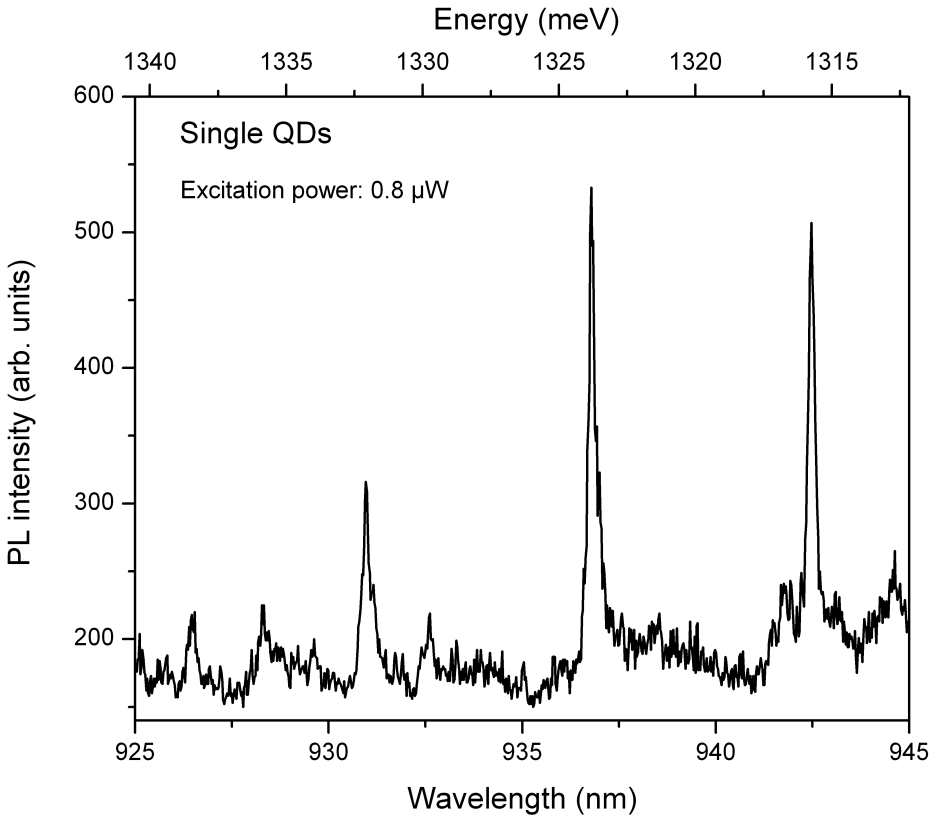

FIGURE 7.1: A PL spectrum of low density QD sample investigated in this chapter. The measurement was performed beside the photonic crystal structure (in bulk).

As it is difficult to obtain single QDs exactly on-resonance with a cavity mode, it is desirable to tune either the dot or the cavity mode to achieve the resonance condition. Cavity mode can be tuned by means of gas deposition [128] or digital etching [129]. The former was difficult to apply in our setup as the size of the sample holder is large, where the gas (nitrogen) will be mostly deposited on the walls of the metal tube and not reaching the sample. The latter is applicable when the sample contains only one PhC cavity. When more PhC cavities are present on the same sample different tunings are needed, which is not possible in this method. Moreover, this method is impractical as one has to take the sample out of the sample holder, and it is irreversible process.

Alternatively, the QD emission line is usually tuned. One way to shift the QD exciton energy is by utilizing the QCSE [130], as discussed in Section 2.6. Other methods include Zeeman shift [131], strain tuning [132], and temperature tuning [83]. In this work, the latter was used for tuning the QD relative to the cavity mode. In this method, the resonance energy of the QD exciton is spectrally shifted to lower energies as a consequence of the temperature dependence of the

semiconductor energy gap. The temperature of the sample was controlled and measured as discussed in Section 5.3.

For bulk $In_{1-x}Ga_xAs$, the Varshni relation can be written as a function of T and x as [133]:

$$E_g(x,T) = 0.42 + 0.625x - \left(\frac{5.8}{T+300} - \frac{4.19}{T+271}\right) 10^{-4} T^2 x - \frac{4.19 \times 10^{-4}}{T+271} T^2 + 0.475x^2, \tag{7.1}$$

where x is the percentage of the Ga in the $In_{1-x}Ga_xAs$ alloy. Figure 7.2 shows the behaviuor of a single InGaAs QD exciton as a function of the sample temperature between 4.2 and 32.4 K. The measured data were fitted by using equation (7.1), and show a good agreement. According to the fit, the content of the Galium is 86%, while it is 14% for the Indium.

By increasing the temperature, the QD emission was redshifted. We were able to tune the QD by $\sim$ 0.6 nm ($\sim$ 0.9 meV), while the linewidth broadened from 0.19 to 0.53 nm (0.25 to 0.75 meV). Further increase in temperature to 32.4 shifted the QD by $\sim$ 1 nm (1.4 meV), but the PL intensity was washed out. This can be attributed to a low confinement energy in this sample. The broadening of the linewidth[1] can be explained according to equation (2.15). By raising the temperature, the dephasing of the QD exciton is increased (T_2 is reduced) due to the increased interaction with phonons, and consequently the linewidth gets broader.

In order to investigate the effect of temperature on the cavity modes, we measured the spectral position of one of the modes as a function of temperature. A high QD density sample was used for this purpose. The data are presented in Fig. 7.3. The cavity mode is also redshifted by increasing the temperature, with a similar behavior (quadratic) like the QD exciton, but with slower rate. This shift is attributed to the increase in the index of refraction with temperature [134].

[1] Please note that these data were measured by using optical fiber and with the spectrometer grating set to 300 line/mm. Thus, the real values for the linewidths are expected to be much smaller.

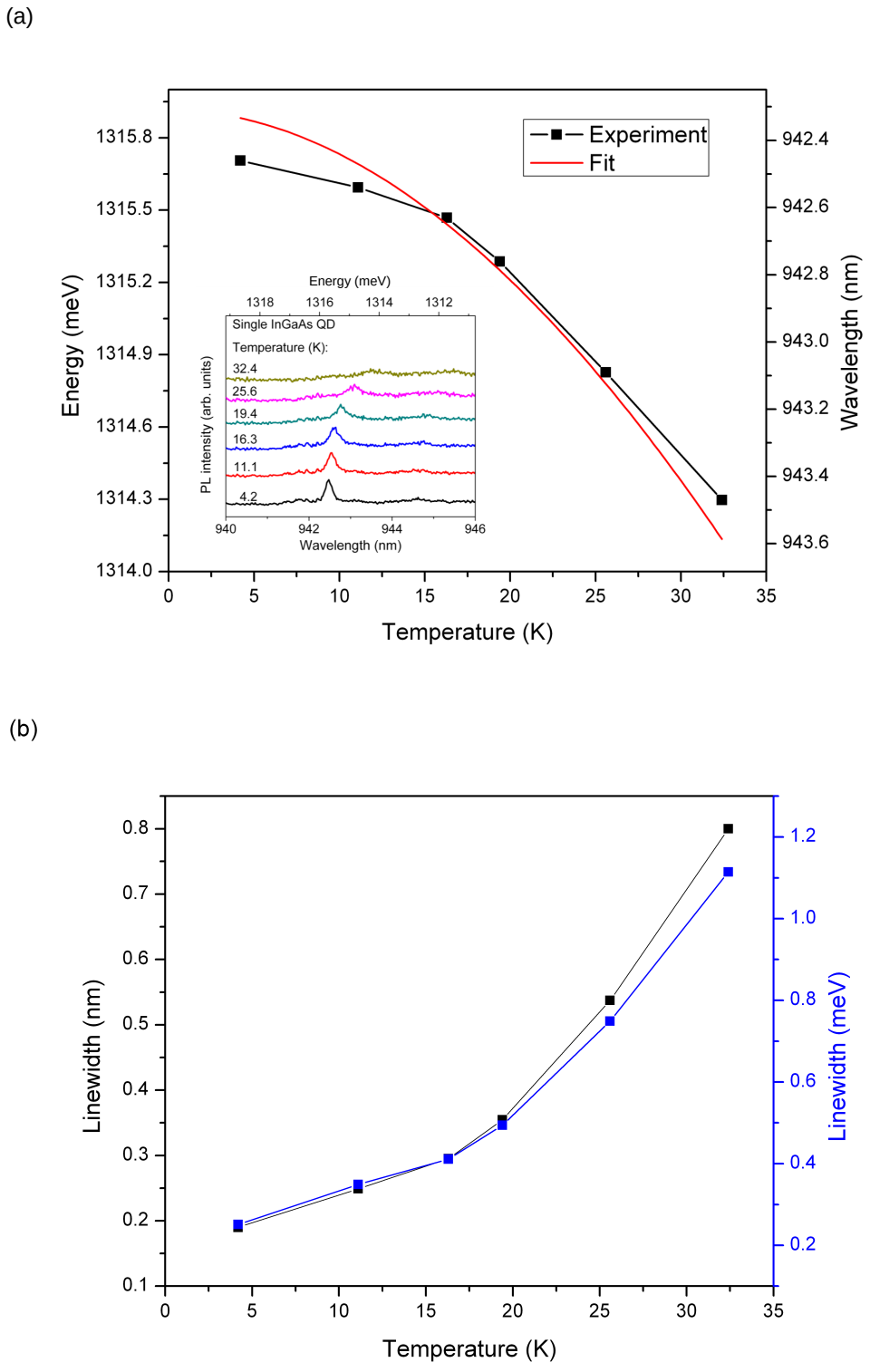

FIGURE 7.2: (a) Position of a QD exciton energy as a function of temperature, with fit to data using the Varshni functional form. The inset shows the measured spectra. (b) The linewidth of the QD exciton as a function of temperature.

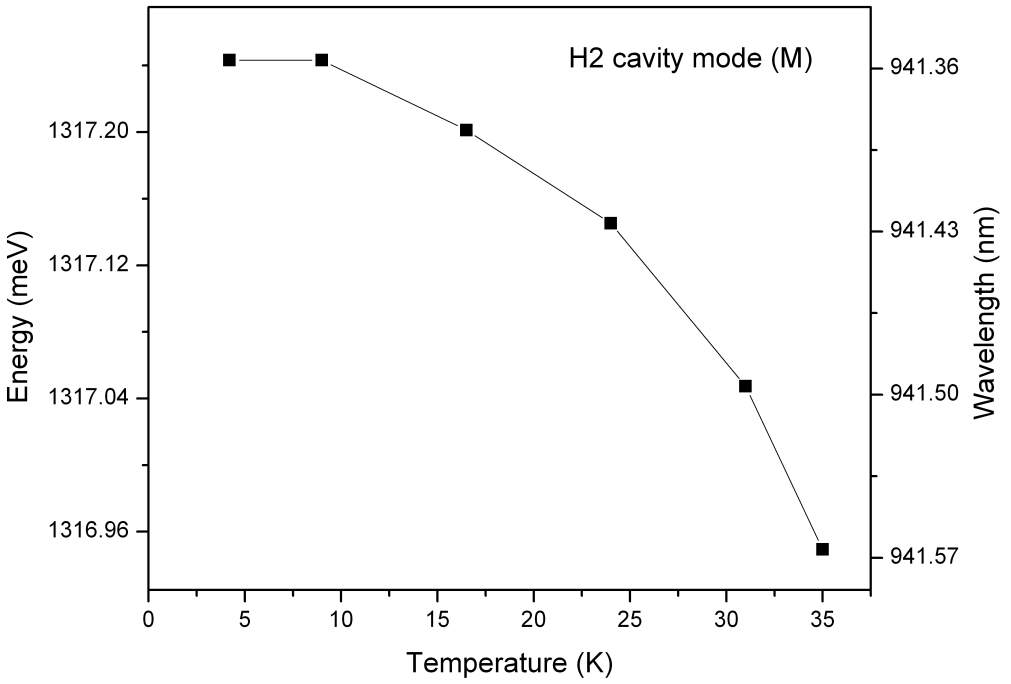

FIGURE 7.3: Temperature dependence of an H2 cavity mode (M).

7.2 Photoluminescence Measurements

With our facilities, we were able to prepare PhC cavities with mode spectral accuracy as low as some nanometers. As the QD used in this work are grown by MBE, the dots are randomly distributed over the sample. Therefore, finding a QD on (or close to) resonance with a cavity mode is not an easy task and relies on coincidence.

In this part, a modified H2 cavity with $s/a = 0.12$ was used, which supports a high-Q cavity mode at around 940 nm (1.319 eV), as discussed in Chapter 6. Figure 7.4 shows a measured PL spectrum for the modified cavity with low QD density at 4.2 K. The system was excited by a HeNe laser with excitation power of 3.7 μW. Thus, the ground and excited states of the QDs as well as the cavity modes can be observed. The PL exhibits two pronounced lines at about 907 nm (1.367 eV) and 940 nm (1.319 eV). The former can be attributed to the whispering-gallery-like mode, whereas the mode at 940 nm is ascribed to the monopole-like mode (M).

The four peaks between 924 nm (1.342 eV) and 934 nm (1.328 eV) are the dipole-like modes, and have weak intensities as they are probably uncoupled to

QDs. The inset in Fig. 7.4 is a zoom of the resonance at around 940 nm, which shows two resonances. We identify them as the ground-state exciton of a single QD and the cavity mode M. The cavity mode is identified to be the lower energy peak as it exhibits slower tuning with respect to temperature. The Q-factor of the caviy mode is around 2100, i.e., the QD-cavity system is in the weak coupling regime.

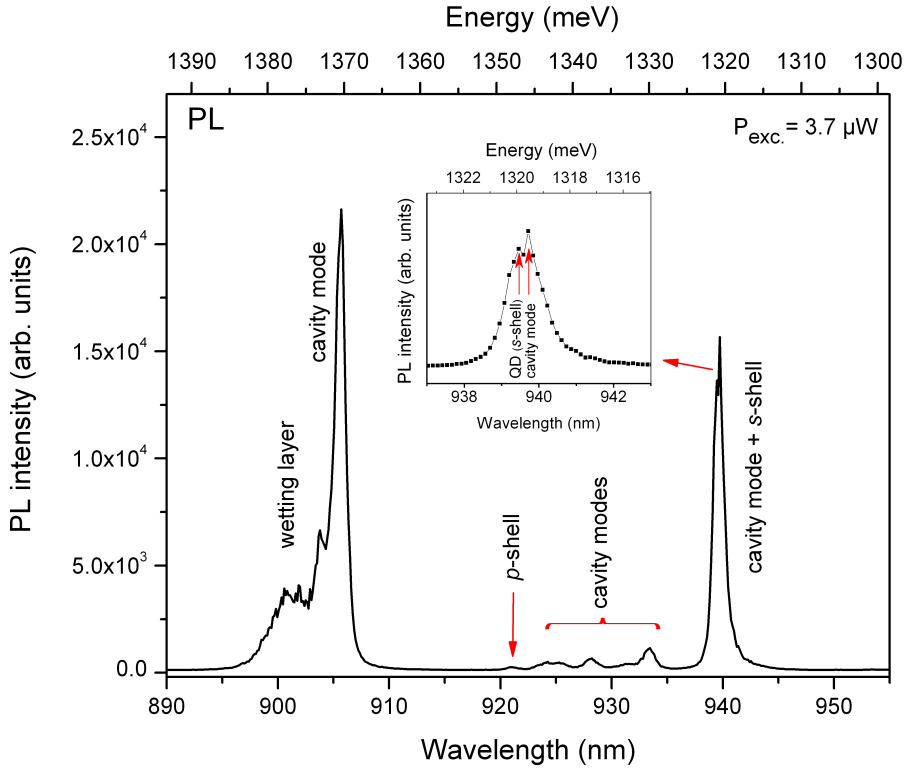

FIGURE 7.4: A detailed PL spectrum of a modified H2 PhC cavity embedded with low density InGaAs QDs at 4.2 K. The inset is a zoom of the peak at around 940 nm (1.319 eV).

In order to reach the resonant case, temperature tuning has been used (see Fig. 7.5). The different energy shifts of the exciton transition and the cavity mode with temperature give rise to a crossing of the two resonances. As these spectra were measured with the spectrometer set to 300 line/mm grating, we can see only one peak. The highest PL intensity corresponding to the crossing, as shown in Fig. 7.5(a). The enhancement of the luminescence, which is an evidence for the weak coupling, is a consequence of the Purcell effect (see equation (2.23)). Figure 7.5(b) shows the intensity of the cavity mode as a function of temperature. The resonance condition, which corresponds to the highest PL intensity, is achieved at 21.3 K and the PL intensity of the system is increased by a factor of 3.7 compared to its value at 4.2 K.

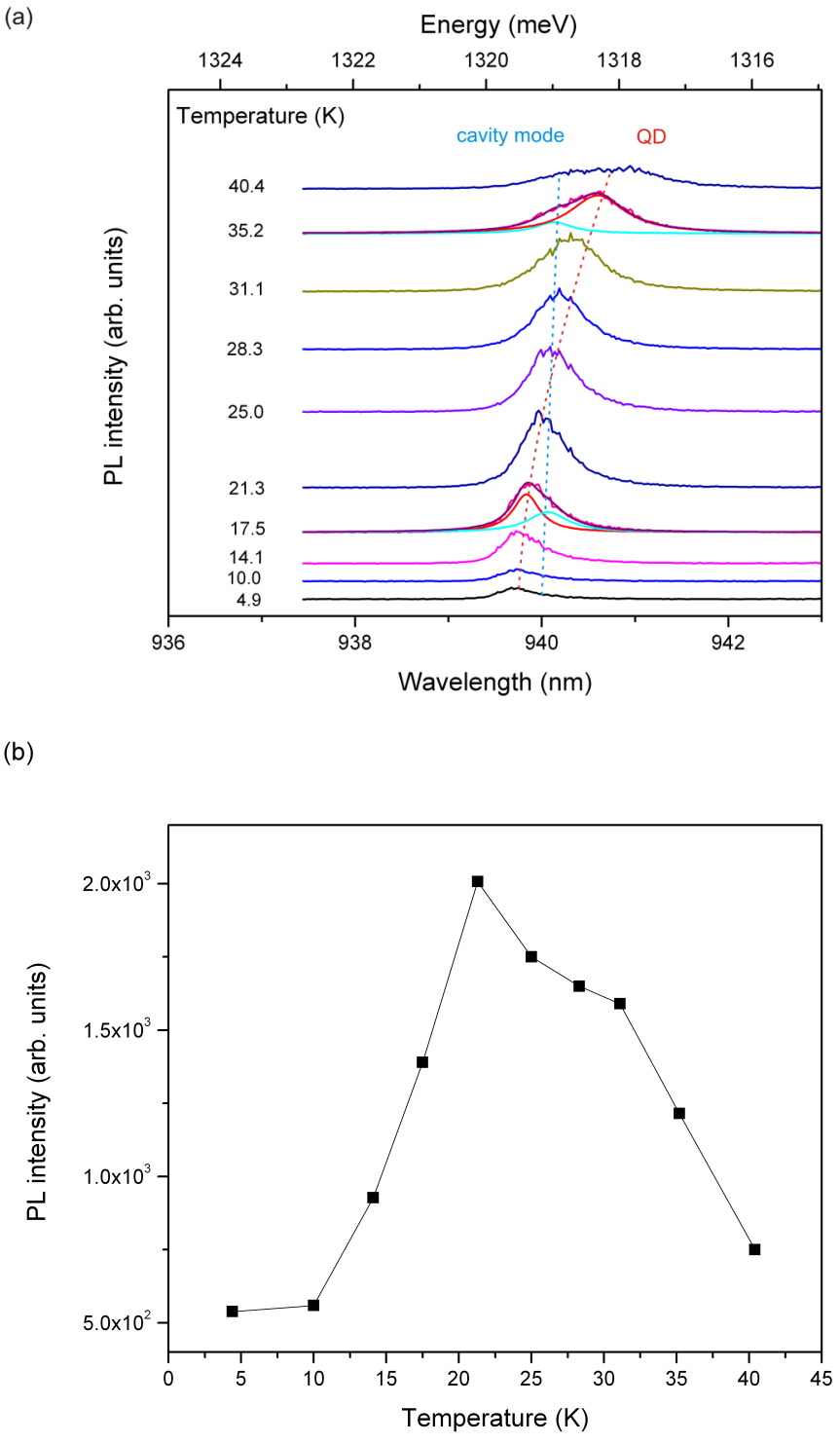

FIGURE 7.5: (a) PL spectra of the QD-cavity system at different temperature values. The enhancement of the PL signal at 21.3 K is due to the QD-cavity crossing. The red and blue dashed lines are given as guides to the eye. (b) Change in the PL intensity of the cavity mode with temperature tuning ($P_{exc.} = 0.8\ \mu$W).

7.3 Photoluminescence Excitation Measurements

In our approach for investigating Rabi oscillations, the ground state exciton is close to resonance with a cavity mode (Section 7.5). Due to the spectral overlap between the excitation laser and the emission of the QD exciton, it is difficult to perform resonant excitation. Some methods have been introduced to overcome this situation, like cross-polarized optical setup [135] and PL detection vertically to the excitation direction [136]. Anyway, these methods are not yet implemented in our setup. Therefore, for coherent state preparation we chose to perform quasi-resonant excitation in the *p*-shell. As discussed in Section 2.5, the *p*-shell exciton relaxes rapidly to the *s*-shell in a ps time scale, where it can interact with the cavity mode in our case (see the inset of Fig. 7.4). Therefore, the spectral position of the *p*-shell has to be identified. For this purpose, we performed photoluminescence excitation (PLE) measurements to investigate the excited states.

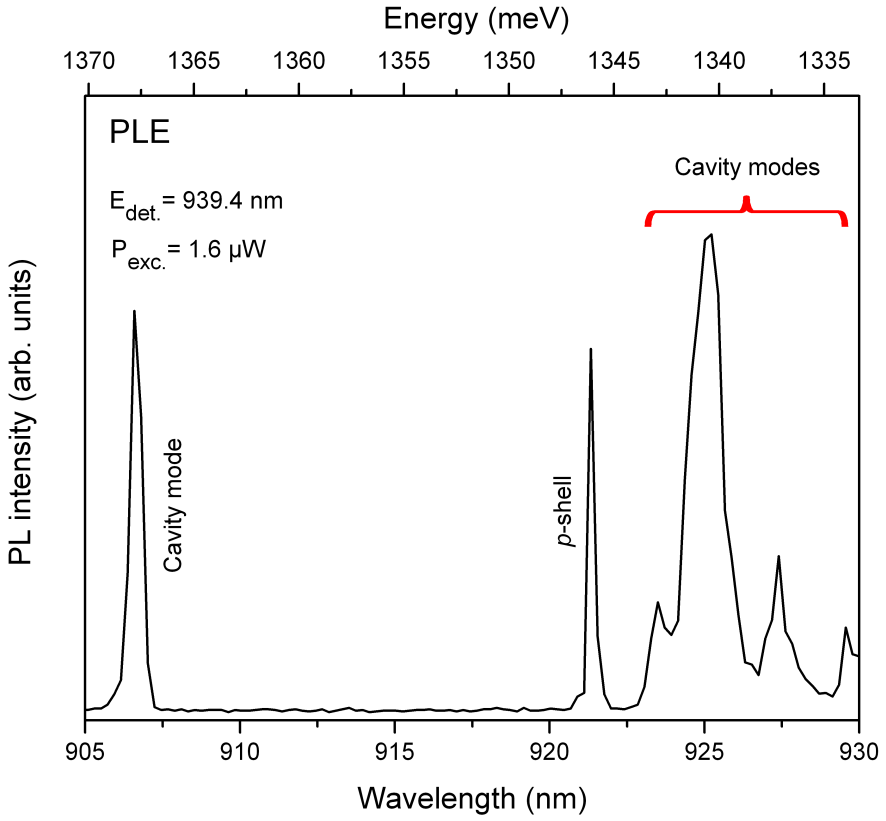

FIGURE 7.6: PLE spectrum of the QD-cavity system. The sharp peak at around 921.3 nm (1345.9 meV) is assigned to the *p*-shell absorption and the other resonances correspond to absorption via higher order modes.

The experimental setup discussed in Section 5.2 was used to avoid the stray light from the laser. A tunable Ti:Sa laser in the cw mode was used to scan the

energy region from 9.4 nm (13.3 meV) to 34.4 nm (50.2 meV) above the ground state exciton, while the detection energy was kept fixed at the ground state energy (939.4 nm (1.320 eV)).

Figure 7.6 shows the PLE spectrum of the investigated QD-cavity system (see the inset of Fig. 7.4). The spectrum contains many resonance peaks. The sharp peak at 921.3 nm (1.346 eV) locates spectrally 18.1 nm (26 meV) above the ground state and is attributed to the p-shell. Other peaks at 907 nm (1.367 eV) and around 925 nm (1.341 eV) are assigned to the absorption via higher order cavity modes [119, 137]. This assignment is based on their spectral position, which coincide with the data presented in Chapter 6 (Fig. 6.7). Also, pulse experiments on-resonant with these modes confirm our assignment, as we will see in the Section 7.5.

One important feature in the PLE spectrum is the absence of phonon absorption, which is usually observed at around 36 and 32 meV above the ground state exciton, for GaAs and InAs LO phonons, respectively [57, 138]. This could be a consequence of the photonic band gap.

7.4 *p*-Shell Saturation

The saturation behavior is an intrinsic property of a two-level system. In our approach to study Rabi oscillations in a cavity, we treat the p-shell transition as a two-level system. To confirm this, we investigated the power dependence of the p-shell excitation detected via the s-shell emission.

Figure 7.7(a) shows the behavior of the QD-cavity system as a function of the p-shell excitation power. The excitation power was gradually increased from 0.3−20 μW at 4.2 K. The power dependence measurements show a nonlinear character for both the QD and the cavity mode. The QD exciton exhibit a clear saturation behavior, which can be described by the fitcurve $I = I_{sat}P/(P + 1)$, where I denotes the PL intensity, I_{sat} its saturation value, and P corresponds to a normalized excitation power.

The saturation behavior of the s-shell emission with increasing p-shell excitation can be understood as follows. If the dot is occupied by one exciton, no further absorption occurs due to the renormalization of the energy levels as a result of a few particle interactions. At low power, the pump rate is so low that each captured p-shell exciton relaxes to the s-shell and recombines before the capture of another exciton. In this limit, the PL intensity is proportional to the excitation power. By increasing the pump power, the pump rate becomes high enough so that the QD is already occupied by one exciton. Thus, the PL intensity saturates at relatively high power due to the state filling [139].

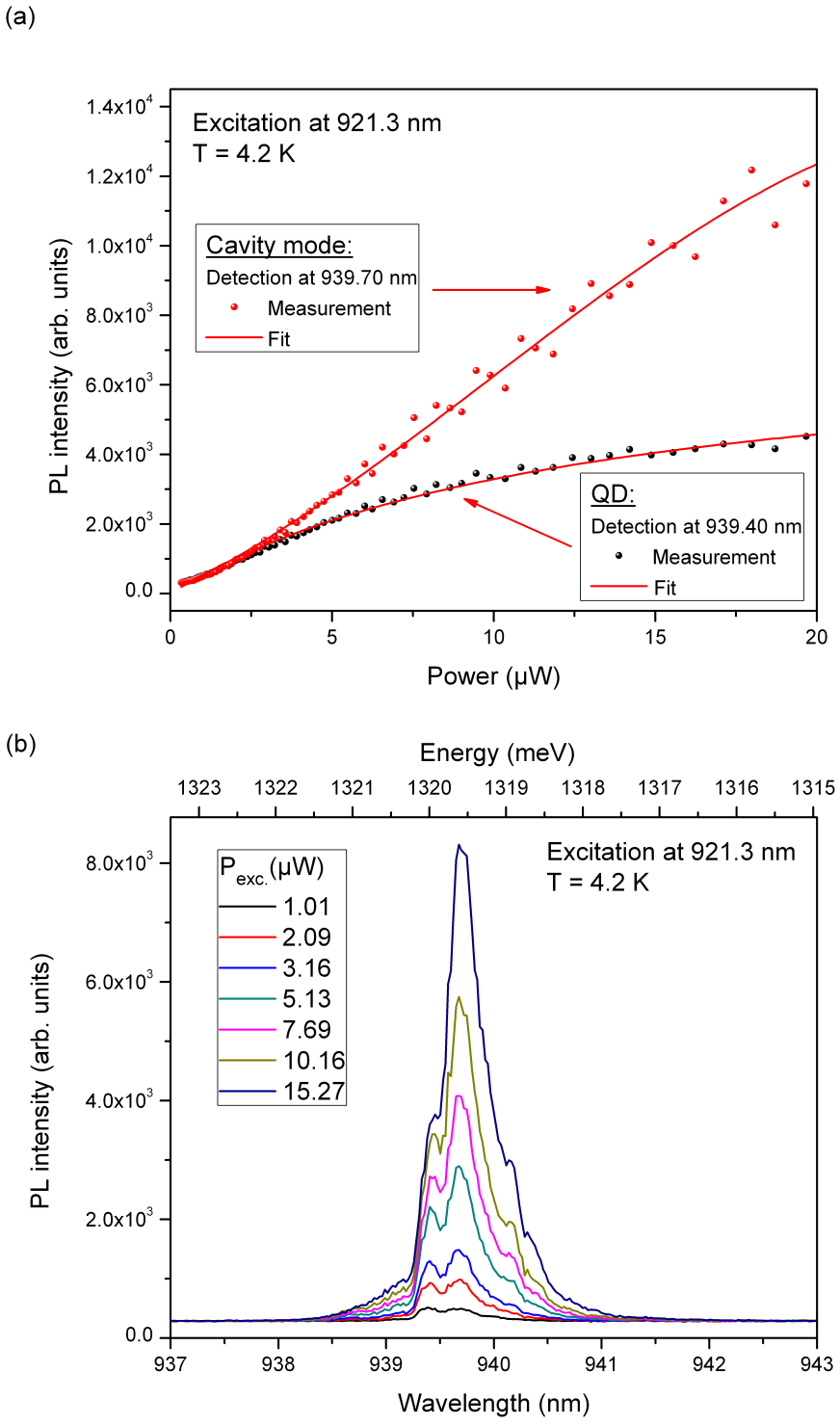

FIGURE 7.7: (a) Power dependence of the PL intensity from the QD ground state and the cavity mode for the resonant p-shell excitation. Both of the QD and the cavity mode show a clear saturation behavior. The QD reaches saturation level at lower power and has a lower PL intensity. The measured PL signal from the QD ground state is well described by the formula $I = I_{sat}P/(P+1)$, as expected for a two-level system. (b) PL spectra of the QD-cavity system at different power values.

In comparison with the cavity mode which saturates at about 35 μW (not shown here), the QD saturates at a lower power with a smaller PL intensity. This could be assigned probably either to the feeding of the mode by the emission of the off-resonance QDs near to the cavity mode [136] or to the contribution of higher states (biexciton and charged excitons).

7.5 Rabi Oscillations

As discussed in the last section, the p-shell transition can be treated as a two-level system. By exploiting this property, P. Ester *et al.* [57] have reported a clean single photon emission based on quasi-resonant excitation of the p-shell, and Rabi oscillations were also observed. Here, we investigate the Rabi oscillations of the p-shell exciton by probing the s-shell emission which is close to resonance with a cavity mode (see the inset of Fig. 7.4).

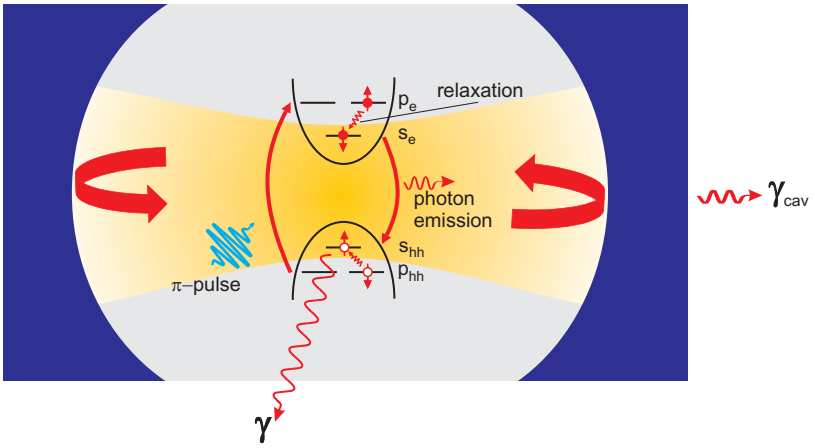

FIGURE 7.8: A schematic representation of the p-shell Rabi oscillations experiment in a cavity. A ps laser pulse is used for the p-shell excitation, followed by a relaxation of the exciton into the s-shell which is near to resonance with the cavity mode. Subsequently, a single photon is emitted and detected in the s-shell PL.

Figure 7.8 shows a schematic diagram of the experiment. Our system consists of a single QD embedded in a modified H2 cavity with $r/a = 0.12$. The ground state exciton is near to resonance with the cavity mode M. ps laser pulses ($\sim$ 3 ps) have been used for the excitation. First, an exciton is created in the p-shell by a π-pulse excitation. This is followed by a fast relaxation into the s-shell, which is spectrally near to resonance with the cavity mode, followed by a single photon emission. The pulse amplitude can be tuned by a neutral density filter wheel to obtain the desired pulse area.

In order to examine the peaks at around 925 nm (Fig. 7.6), we have performed pulsed resonant excitation. The p-shell Rabi oscillations can be observed for only the resonance condition. If the pulsed excitation is in resonance with one of the higher order cavity mode (which are here off-resonant with the p-shell), no oscillations can be observed due to the incoherent excitation.

Figure 7.9 (green curve) shows the Rabi oscillations of the p-state at 921.3 nm (1.346 eV) detected in the ground state PL. A clear first maximum in the PL, which corresponds to a π-pulse, is observed at around 2 $(\mu W)^{1/2}$. Only the first Rabi flop was observed due to the high damping, as it was reported by P. Ester *et al.* [57]. The main dephasing mechanism is the relaxation to the s-shell.

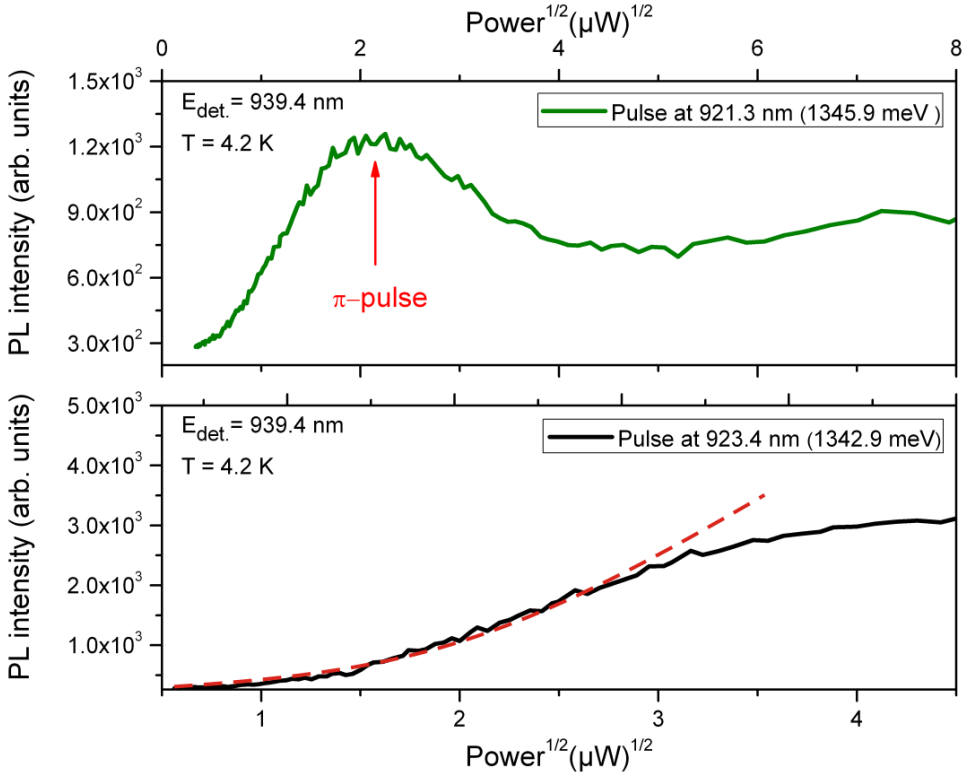

FIGURE 7.9: (Upper) p-shell Rabi oscillation of a QD exciton in a cavity measured in the s-shell. A clear maximum is observed, which corresponds to a π-pulse. (Lower) Pulse excitation resonant with the cavity mode at 923.4 nm (1.343 eV).

We also performed pulsed resonant excitation at the peaks which are attributed to the cavity modes around 925 nm (1.341 eV). Unlike the p-shell, they exhibit no oscillatory behavior, which confirms our assignment. The black curve in Fig. 7.9 shows the measured data for pulse excitation via the cavity mode at 923.4 nm (1.343 eV). The PL intensity is first proportional to the power before it saturates. This is a characteristic behavior for an incoherent excitation, which is in this case (923.4 nm) also non-resonant with the p-shell.

We have performed pulsed excitation at the *p*-shell (921.3 nm) at different temperatures and detected the PL emission in the *s*-shell. Heating of the sample for energy tunings was achieved as discussed in Section 7.1. Data for this experiment are shown in Fig. 7.10(a). They show signatures for temperature dependent damping, PL intensity changes, and shift of the Rabi frequency. Raising the temperature leads to a redshift of the *p*-shell relative to the laser[2], and decreases the detuning between the *s*-shell and the cavity mode. Therefore, we should distinguish here between effects which regard the *p*-shell and others which are important for the *s*-shell. By increasing the temperature, we observe a change in the *p*-shell Rabi frequency and the PL intensity of the *s*-shell. First, we discuss the origin of the increase of the Rabi frequency. Then, propositions for the change of the PL intensity are given.

The first observation was that the Rabi frequency increases with temperature, i.e., lower pulse area is required for a Rabi flop. As discussed in Section 2.8, the detuning from the resonant case gives rise to an increase of the Rabi frequency and a reduction in the occupation probability [73]. Therefore, a possible reason for the increase of the Rabi frequency could be the detuning between the laser and the *p*-shell. In our experiment, the increase of the Rabi frequency manifests itself in a decrease of the excitation amplitude required for Rabi flopping. At 17.3 K, the Rabi oscillation is drastically damped, and no oscillation behavior can be observed for higher detunings. This could be attributed to the higher dephasing rates at higher temperatures.

By increasing the temperature, the PL emission of the *s*-shell is first increased before it decreases at higher temperatures. Figure 7.10(b) shows a PL spectrum of the *s*-shell for *p*-shell resonant excitation. The lines under the spectrum indicate the spectral position of the QD exciton with respect to temperature, which is inferred from Fig. 7.2(a). At 4.2 K, the QD-cavity system is detuned by ~ 0.3 nm (~ 0.4 meV) and a clear Rabi flop is observed at 2.05 $(\mu\mathrm{W})^{1/2}$ with a specific PL intensity (~ 1200 counts/s), as shown in Fig. 7.10(a).

[2] The Ti:Sa laser can be tuned by ~ 0.3 nm wavelength steps. Therefore, the laser wavelength was kept at 921.3 nm when slightly raising the temperature.

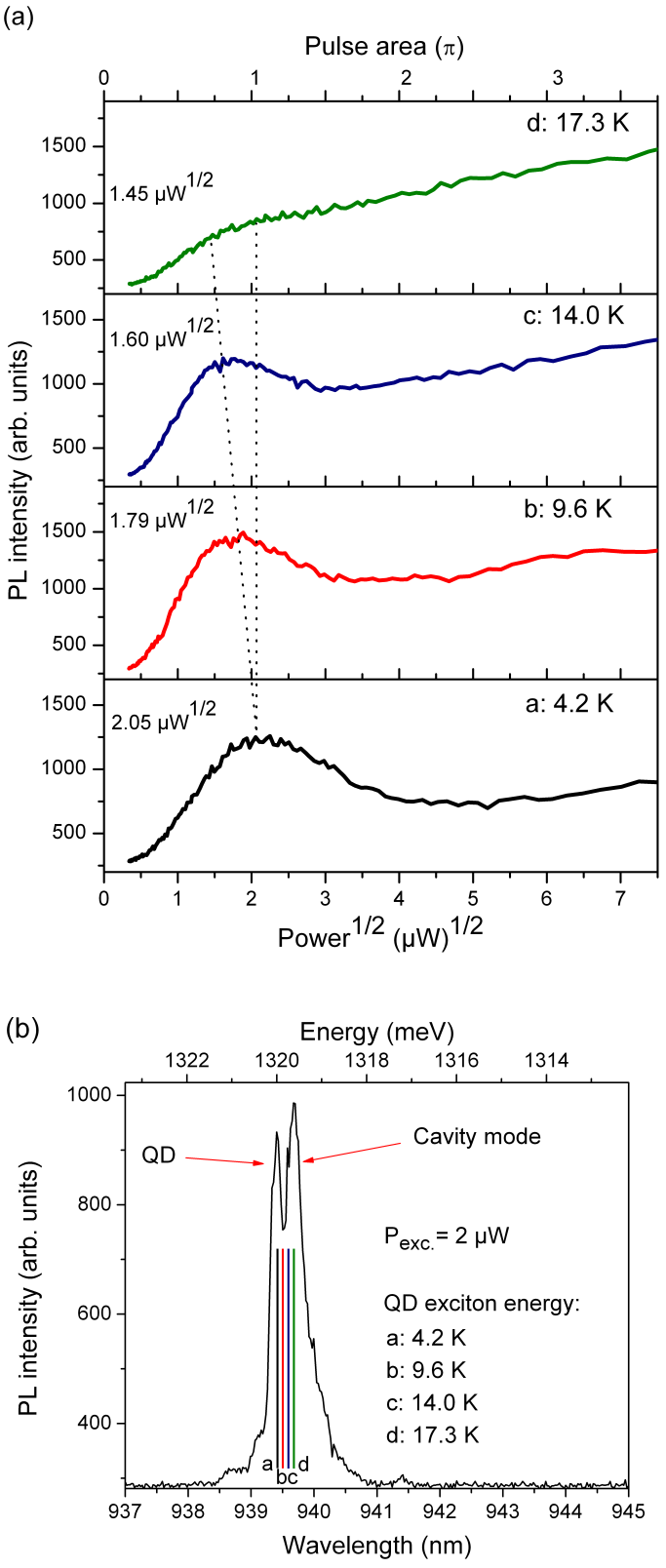

FIGURE 7.10: (a) *p*-shell Rabi oscillation for different detuning energies. The black dashed lines serve as guides to the eye. (b) PL spectrum of the QD-cavity system excited in the *p*-shell at 4.2 K with detuning of $\sim$ 0.3 nm ($\sim$ 0.4 meV). The lines under the spectrum indicate the spectral position of the QD exciton with respect to temperature.

In a bare system without PhC cavity, the maximum PL intensity is expected to decrease with increasing temperature as a result of the detuning between the *p*-shell and the laser. However, when the *s*-shell is first slightly blue-shifted with respect to the cavity mode, we observe the opposite. By tuning the temperature from 4.2 K to 9.6 K, which corresponds to a tuning of the dot by 0.07 nm (0.1 meV) (red curve in Fig. 7.10(a)), the maximum PL intensity is increased by $\sim$ 20%. This can be explained by a resonance effect: when the detuning between the QD exciton and the cavity mode is reduced, the system is tuned toward the resonance condition, and therefore the PL intensity increases. By further raising the temperature to 14.0 K, the PL intensity decreases again and reaches a value close to the 4.2 K case. Further increase of temperature results in suppression of the PL signal. This can be assigned to the rather high exciton line broadening with temperature of this sample, as the data in Fig. 7.2 show.

The analyses of our system have shown that our approach for observation of the *p*-shell Rabi oscillations in a cavity, where the *s*-shell is close to resonance with a cavity mode, is complicated. For further suggestions see Chapter 8 (Conclusion and Outlook).

Chapter 8

Conclusion and Outlook

The work in this PhD thesis has been focused on the study of GaAs photonic crystal (PhC) cavities with embedded InGaAs quantum dots (QDs). We achieved a significant progress in developing the fabrication process to obtain high quality samples. The effect of modifying the air holes surrounding the cavity on the quality factor (Q) has been systematically investigated. Moreover, coherent experiments have been performed on a QD exciton in a PhC cavity.

The Finite-Difference Time-Domain (FDTD) method was used in the calculation of the properties of resonant modes, including electric field distributions, resonant frequencies, and Q-factors. The fabrication process of PhC cavities by electron beam lithography and etching technique was developed. The optical properties of these cavities were investigated by micro-photoluminescence technique, and the cavity modes were identified by polarization-dependent measurements. The obtained results were in good agreement with the theoretical calculations performed by using the FDTD method.

Different geometries of PhC cavities with have been investigated (see the Appendix), with focus particularly on H2 cavity. The large size of the H2 cavity, in comparison with H1 and L3, offers more flexibility for future designs of functionalized defect regions, for example when introducing electrical contact to the center of the defect region, or adopting a post beneath the cavity region. The cavity region was optimized to increase the Q-factor of the monopole-like mode. By radially shifting the nearest neighbor air holes around the cavity, it was possible to increase the Q-factor significantly (from 1500 to more than 7000), while keeping the effective mode volume almost unchanged.

The p-shell Rabi oscillations have been investigated in a modified H2 cavity. Pulsed laser excitation on-resonance with the p-shell have been used for state preparation, while detecting the PL intensity in the s-shell which is close to resonance with a cavity mode. We were able to observe the first p-shell Rabi flop of

a QD exciton in PhC cavity. We have performed pulsed excitation at the p-shell at different temperatures. The results show signatures for temperature dependent damping, PL intensity changes, and shift of the Rabi frequency. The increase in the Rabi frequency was attributed to the detuning between the laser and the p-shell, while the change in the PL intensity of the s-shell was assigned to a resonant effect.

For further confirmation of change in the PL amplitude, it would be better either to tune the QD exciton electrically to avoid the high dephasing rate or to tune the cavity mode by gas deposition. Concerning the Rabi frequency, it would be preferred to have the p-shell in resonance with a cavity mode. But it could be difficult to observe the Rabi oscillations as the dephasing rate is quite high in the p-shell. Alternatively, resonant excitation is preferred from physical point of view. For example, it was shown that incoherent excitation via an excited state (p-shell) cannot simultaneously provide single photons with high degree of indistinguishability and quantum efficiency [140]. The reason in this is the time-jitter which is induced by the relaxation from the p-shell to the s-shell of the QD. Therefore, resonant pumping of a QD in a cavity would be an advantageous.

Recently, many research groups have been able to perform resonance fluorescence experiments in single QDs in cavities, allowing coherent manipulation of the ground state excitons [136, 141]. However, the integration of QD-cavity system into an electrically driven circuit is more advantageous from a practical point of view. By exploiting the well established photocurrent spectroscopy [72], resonant pumping of QDs in cavity can be performed, allowing coherent control and state preparation. Moreover, electrical contacts allow fast QD tuning.

Very recently, A. Faraon *et al.* [142] have reported fast electrical control of strongly coupled QDs in PhC cavities. In their work, they introduced Schottky contact electrode in the close vicinity to the cavity (750 nm from the center of the cavity). We believe that utilizing thin stripes on the top of the cavity could control the QD-cavity system more effectively. This will enable coherent electrical experiments in cavities like s-shell Rabi oscillations, Ramsey fringes, and exciton phase manipulation [143]. In our approach, a thin metal stripe is introduced on the top of the cavity, forming an n-i-schottky contact.

Figure 8.1(a) shows primary results of an electrically contacted PhC cavity. The photocurrent measurements were performed as discussed in Section 2.7.2. Both the photoluminescence and photocurrent spectra are plotted for comparison. The Q-factor of the mode at 938.5 nm is ~ 1000, while it is ~ 1800 for a non-contacted cavity on the same sample (not shown here). Also, the spectral position of the cavity mode is redshifted by a few nm when the metal stripe is introduced. Figure

8.1(b) shows a typical SEM image of the system, where the stripe lies nicely over the cavity.

To minimize the optical losses induced by the stripe, some issues have to be considered. For example, the thickness, the width, and the material of the stripe have to be investigated in this context. Also, by carefully considering the field distribution in the cavity, it is possible to design a stripe in certain direction to reduce the optical losses.

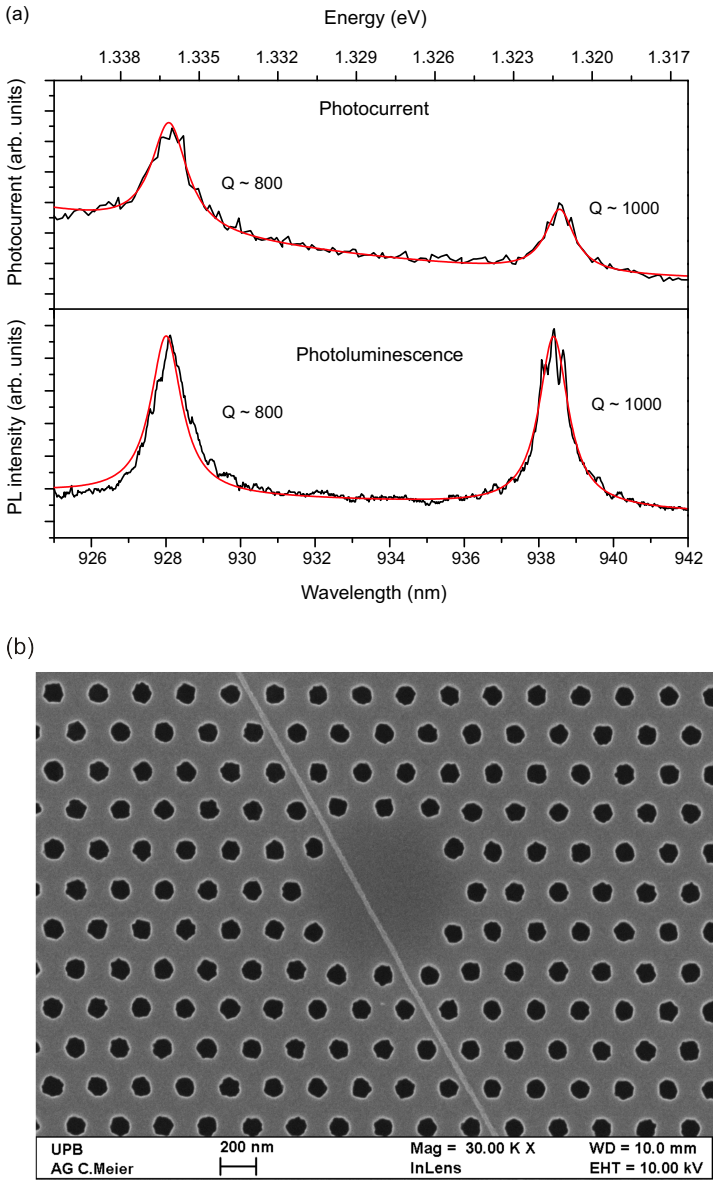

FIGURE 8.1: (a) Photocurrent and photoluminescence spectra of an electrically contacted H2 PhC cavity. (b) Typical SEM image of a contacted cavity showing the metal stripe. These data have been provided by Wadim Quiring.

Appendix A

Cavities With Different Geometries

This appendix summarizes the characteristics of H1, L3, and L5 PhC cavities. For Q-factor optimization, these cavities are investigated by shifting the air holes surrounding the cavity systematically. Both theoretical calculations and experimental results are given here. Also, polarization-dependent measurements are provided. We have used the same lattice parameters as discussed in Section 6.1 (a = 250 nm, $r = 0.25a$, thickness $t = 0.72a$).

A.1 H1

This type of cavities (H1) is formed by omitting a single hole in a triangular PhC lattice, as shown in Fig. A.1(a). It can support a number of modes depending on its design [144]. Figures A.1(b) and (c) show typical SEM images of an unmodified H1 cavity and a modified cavity, respectively.

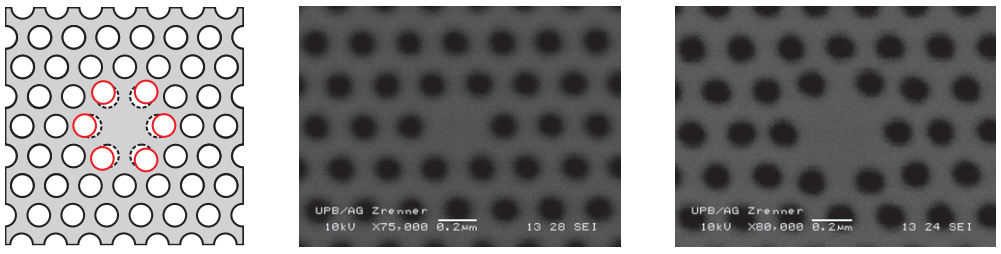

(a) (b) (c)

FIGURE A.1: (a) Modified H1 cavity structure. SEM images of (b) an H1 cavity and (c) a modified cavity with air holes shift of $s/a = 0.12$.

For our parameters, only the degenerate dipole modes are exist within the photonic band gap (at 940 nm (1.319 eV)). As the nearest-neighbor air holes are

shifted away from the cavity, the hexapole mode appears at higher energy (near to the band gap edge). In order to improve the Q-factor, the air holes surrounding the cavity were shifted radially away from the center of the cavity, as depicted in the red colored circles in Fig. A.1(a).

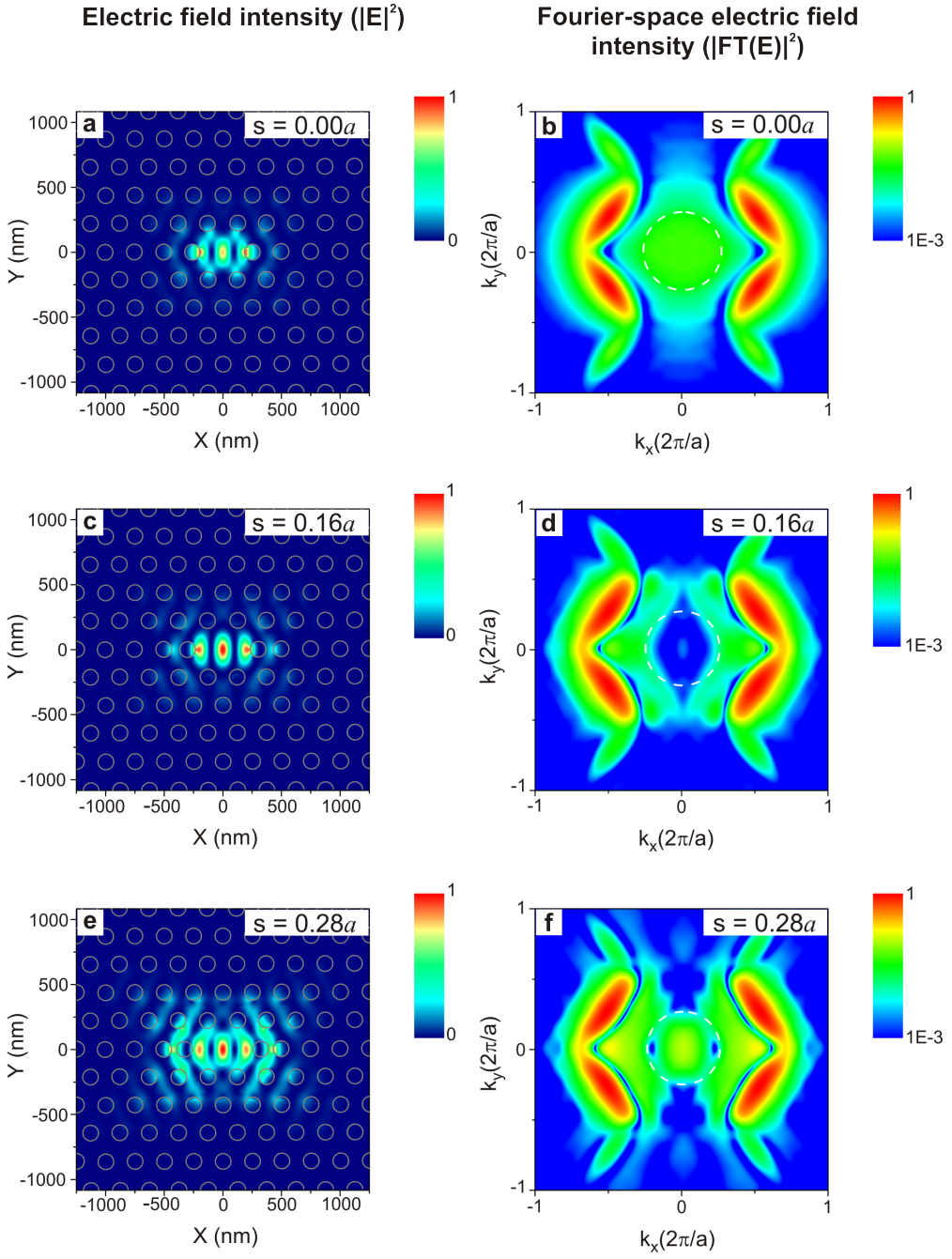

FIGURE A.2: Electric field intensity profiles of the degenerate dipole mode (D1) with air holes shift of (a) zero, (c) $0.16a$, and (e) $0.28a$. The corresponding 2D Fourier transform of the electric field intensity $\left(|FT\,(E_x)|^2 + |FT\,(E_y)|^2\right)$ is plotted in graphs (b), (d), and (f). The dashed white circles in graphs (b), (d), and (f) represent the light cone boundary (the light line), which is defined by $k_x^2 + k_y^2 = (\omega/c)^2$. Note the reduction of the wavevector components inside the light line for shift of $0.16a$ (graph (d)).

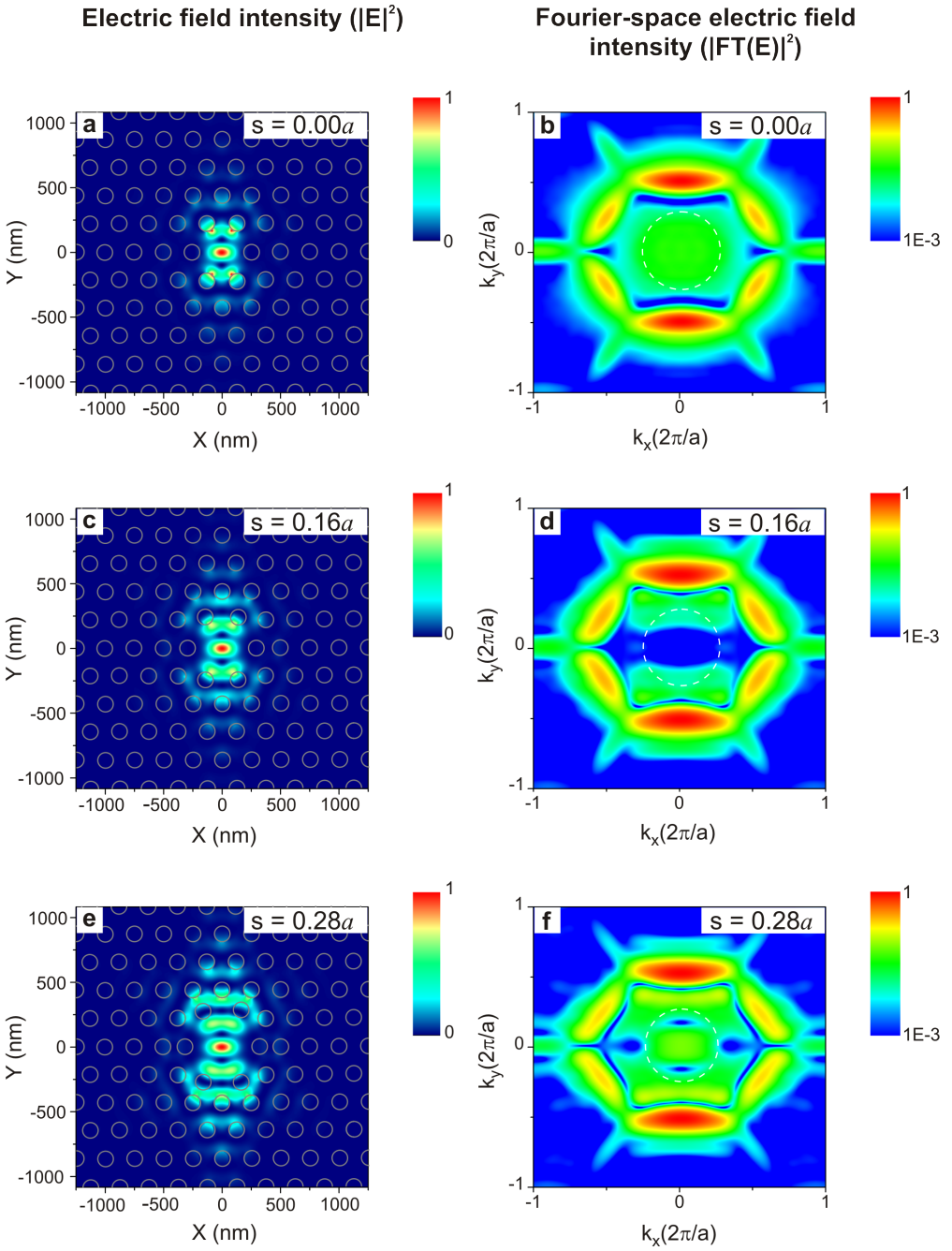

FIGURE A.3: Electric field intensity profiles of the degenerate dipole mode (D2) with air holes shift of (a) zero, (c) $0.16a$, and (e) $0.28a$. The corresponding 2D Fourier transform of the electric field intensity $\left(|FT\,(E_x)|^2 + |FT\,(E_y)|^2\right)$ is plotted in graphs (b), (d), and (f). The dashed white circles in graphs (b), (d), and (f) represent the light cone boundary (the light line), which is defined by $k_x^2 + k_y^2 = (\omega/c)^2$. Note the reduction of the wavevector components inside the light line for shift of $0.16a$ (graph (d)).

In the same way as discussed in Section 6.1, we investigate the effect of the air holes displacement on the electric field components inside the light cone. Figures A.2(a), (c), and (e) show the distribution of the electric field intensity and the corresponding FT spectra for different air holes shift for one of the degenerate

dipole modes (D1). It is clearly seen that the field components are minimized at shift of $0.16a$, and consequently a maximum Q is expected. The second dipole mode (D2) follows the same behavior, as shown in Fig. A.3.

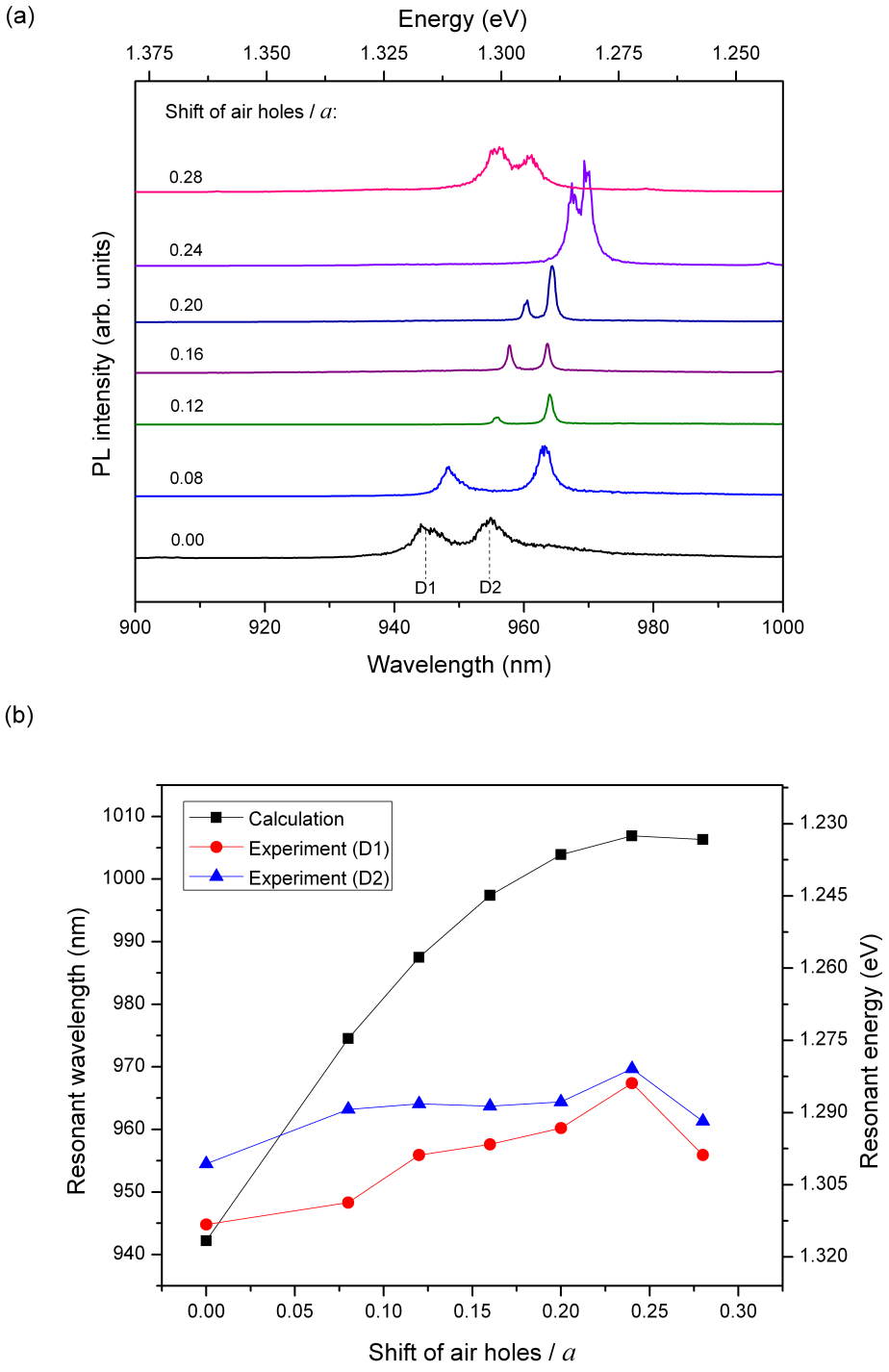

FIGURE A.4: (a) Measured PL spectra of H1 PhC microcavities with different air holes shifts s, described by the parameter s/a. (b) The spectral position of the resonant wavelength of the D1 and D2 dipole modes as a function of the air holes shift s.

Figure A.4(a) presents the experimental measurements on H1 cavities with various air holes shifts. The two peaks are attributed to the degenerate dipole mode, where the dipole degeneracy is broken due to the imperfections. With increasing the shift of the inner holes, the resonance peaks are redshifted due to the increase of the effective cavity size. The wavelengths of the cavity modes as a function of the air holes shift are plotted in Fig. A.4(b).

Figure A.5 shows polarization-dependent PL measurements on an H1 cavity. This figure reflects the orthogonality of the dipole modes. High linear polarization degree up to 0.92 has been achieved for the lower energy mode. Finally, Fig. A.6 includes the calculated and measured Q-factors of H1 cavities as a function of s/a for various air holes shifts from zero to $0.28a$. A maximum Q value of 2800 has been achieved for displacement of $0.12a$.

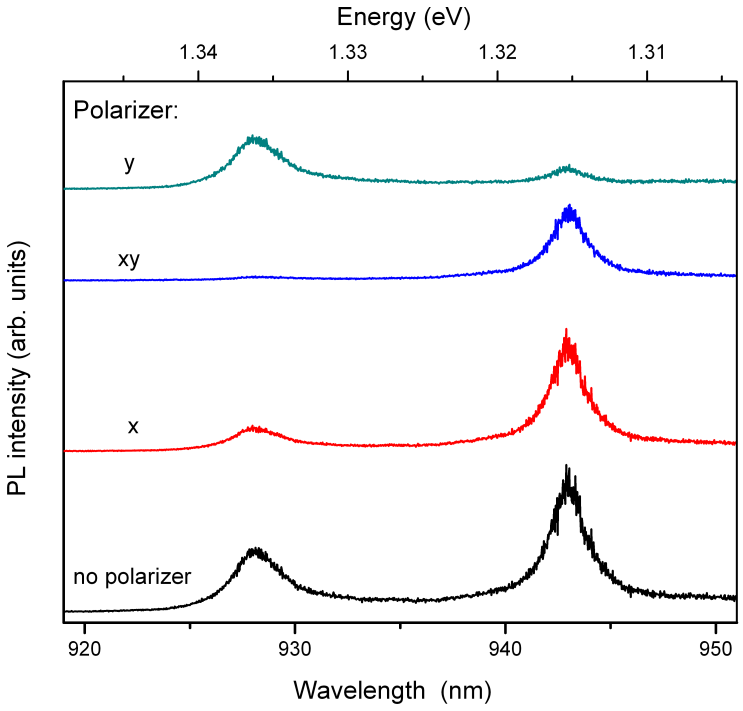

FIGURE A.5: Polarization-dependent PL spectra of an unmodified H1 cavity.

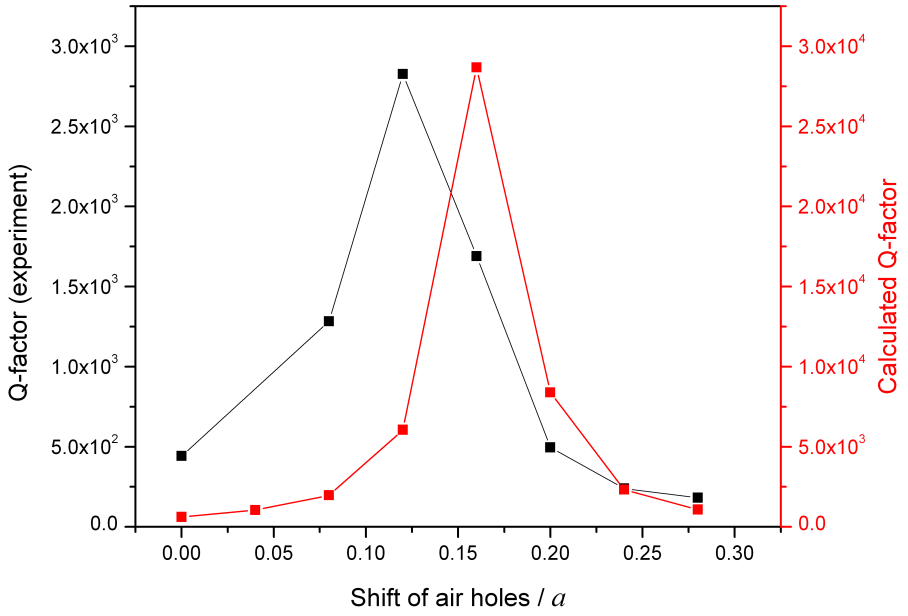

FIGURE A.6: Calculated and measured Q-factors of the D2 modes as a function of the displacement of the air holes (s/a). A maximum Q value of 2800 has been achieved for $s/a = 0.12$.

A.2 L3

The L3 PhC cavities are formed by omitting three holes in triangular PhC lattice, as shown in Fig. A.7(a). Typical SEM images of an unmodified L3 cavity and a modified cavity with $s/a = 0.12$ are depicted in Figs. A.7(b) and (c), respectively. For our parameters, four modes are present where one is degenerate mode, as shown in Fig. A.8.

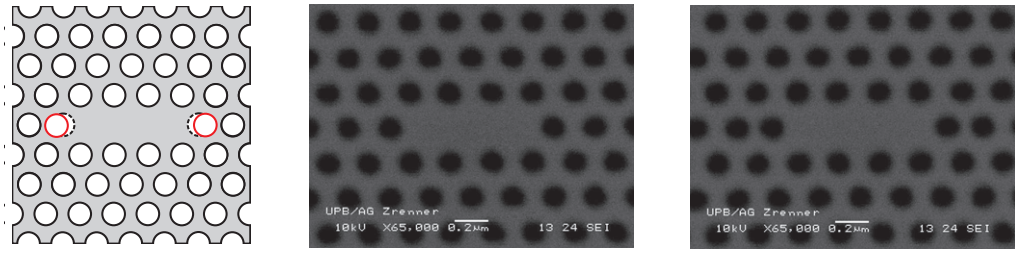

FIGURE A.7: (a) Modified L3 cavity structure. SEM images of (b) an L3 cavity and (c) a modified cavity with air holes shift of $s/a = 0.12$.

The Q-factor of the fundamental mode (Fig. A.8(e)) can be improved by shifting the air holes at both edges of the cavity, as illustrated in the red colored circles in Fig. A.7(a).

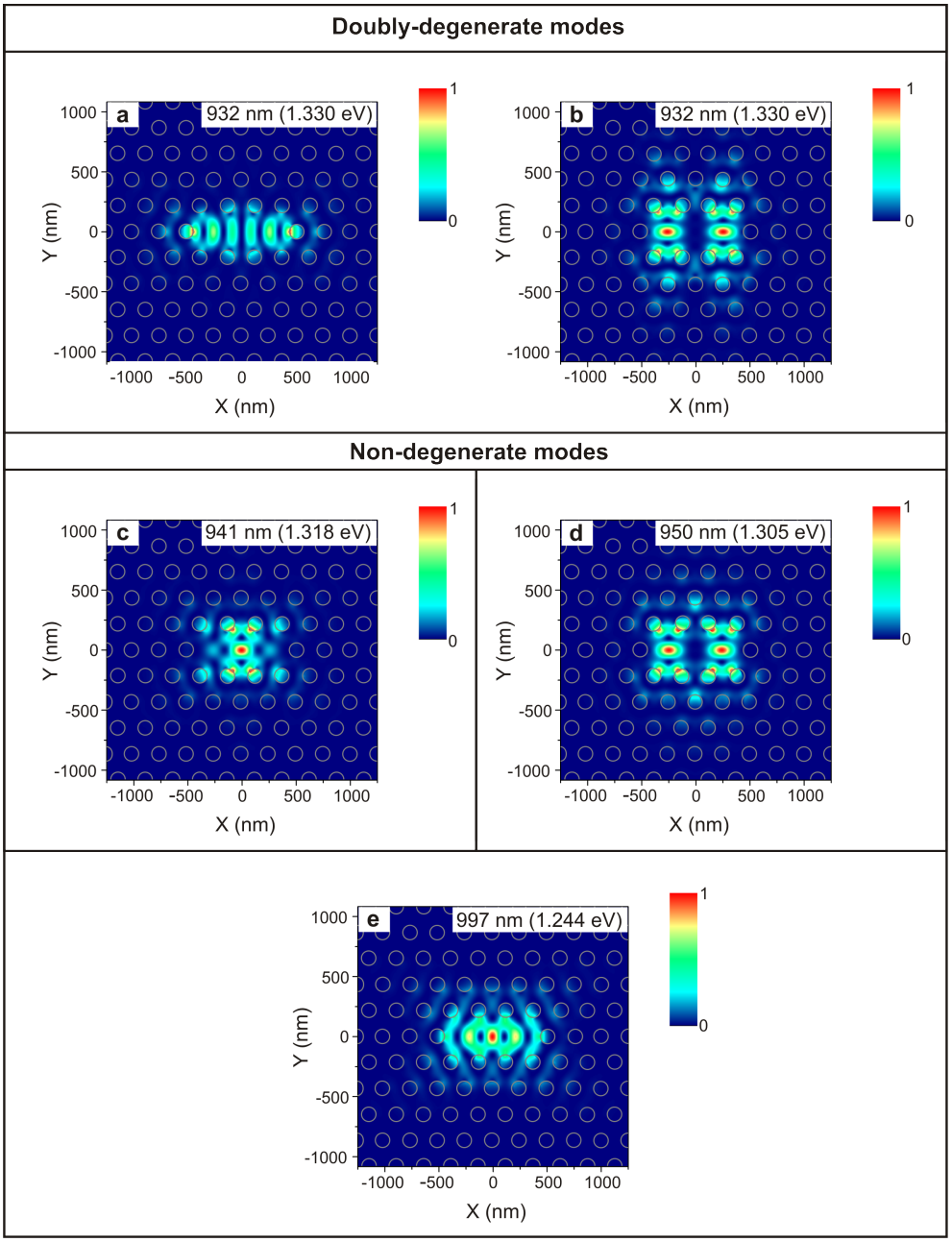

FIGURE A.8: Calculated electric field intensity profiles of L3 cavity modes with $a = 250$ nm, $r = 0.25a$, and $t = 0.72a$.

Figures A.9(a), (c), and (e) show the distribution of the electric field intensity and the corresponding FT spectra for different air holes shift for the fundamental mode. The same behavior as in H1 cavity is also observed here. The field components are minimized at shift of $0.20a$, and consequently a maximum Q is expected. The experimental measurements on L3 cavities with different air holes

shifts are plotted in Fig. A.10(a), where only the fundamental mode is shown. With increasing the shift of the inner holes, the resonance peak is redshifted due to the increase of the effiective cavity length. Figure A.10(b) shows the wavelength of the cavity mode as a function of the displacement.

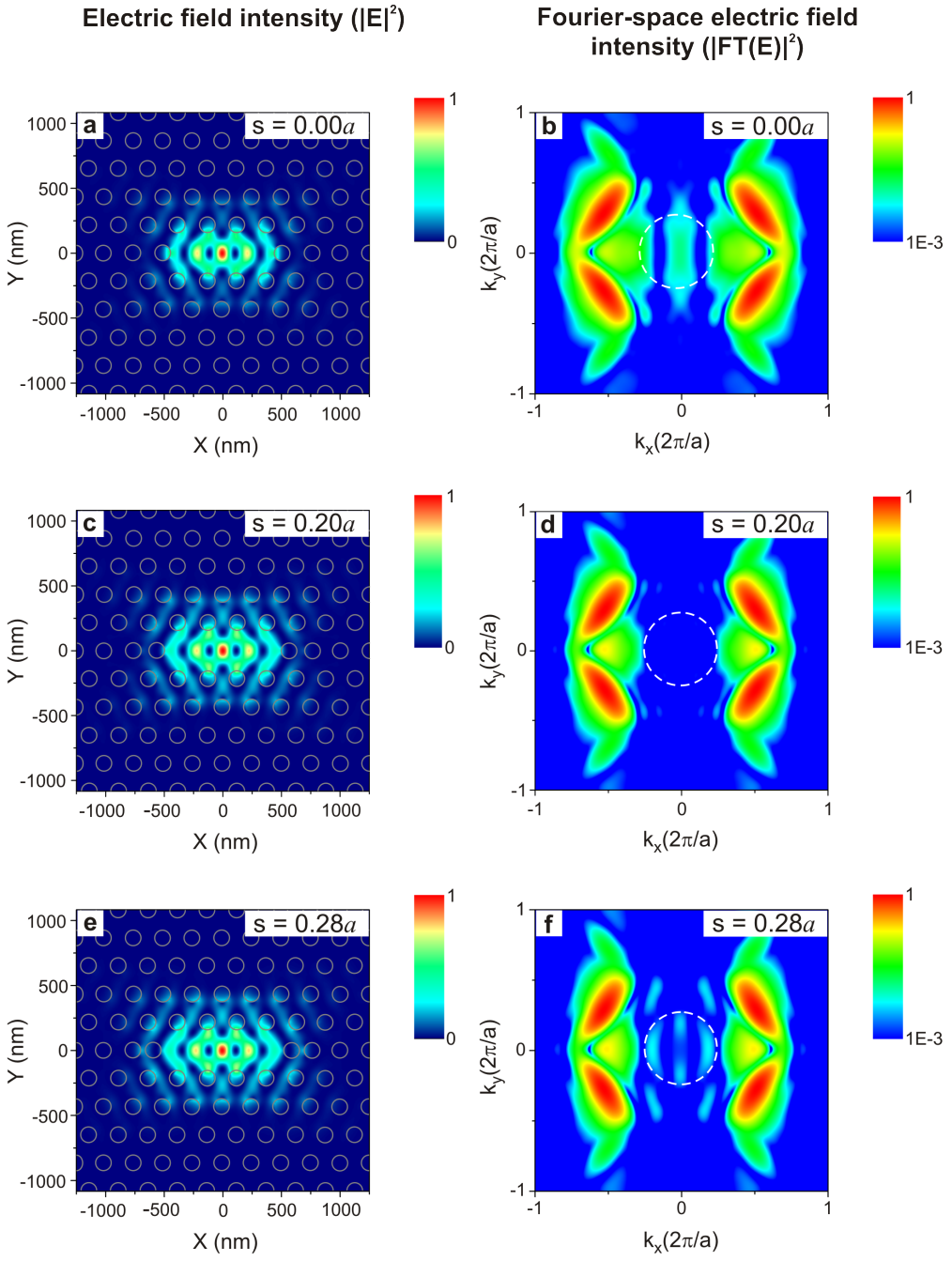

FIGURE A.9: Electric field intensity profiles of the fundamental mode of L3 PhC cavities with air holes shift of (a) zero, (c) $0.20a$, and (e) $0.28a$. The corresponding 2D Fourier transform of the electric field intensity $\left(|FT\,(E_x)|^2 + |FT\,(E_y)|^2\right)$ is plotted in graphs (b), (d), and (f). The dashed white circles in graphs (b), (d), and (f) represent the light cone boundary (the light line), which is defined by $k_x^2 + k_y^2 = (\omega/c)^2$. Note the reduction of the wavevector components inside the light line for shift of $0.20a$ (graph (d)).

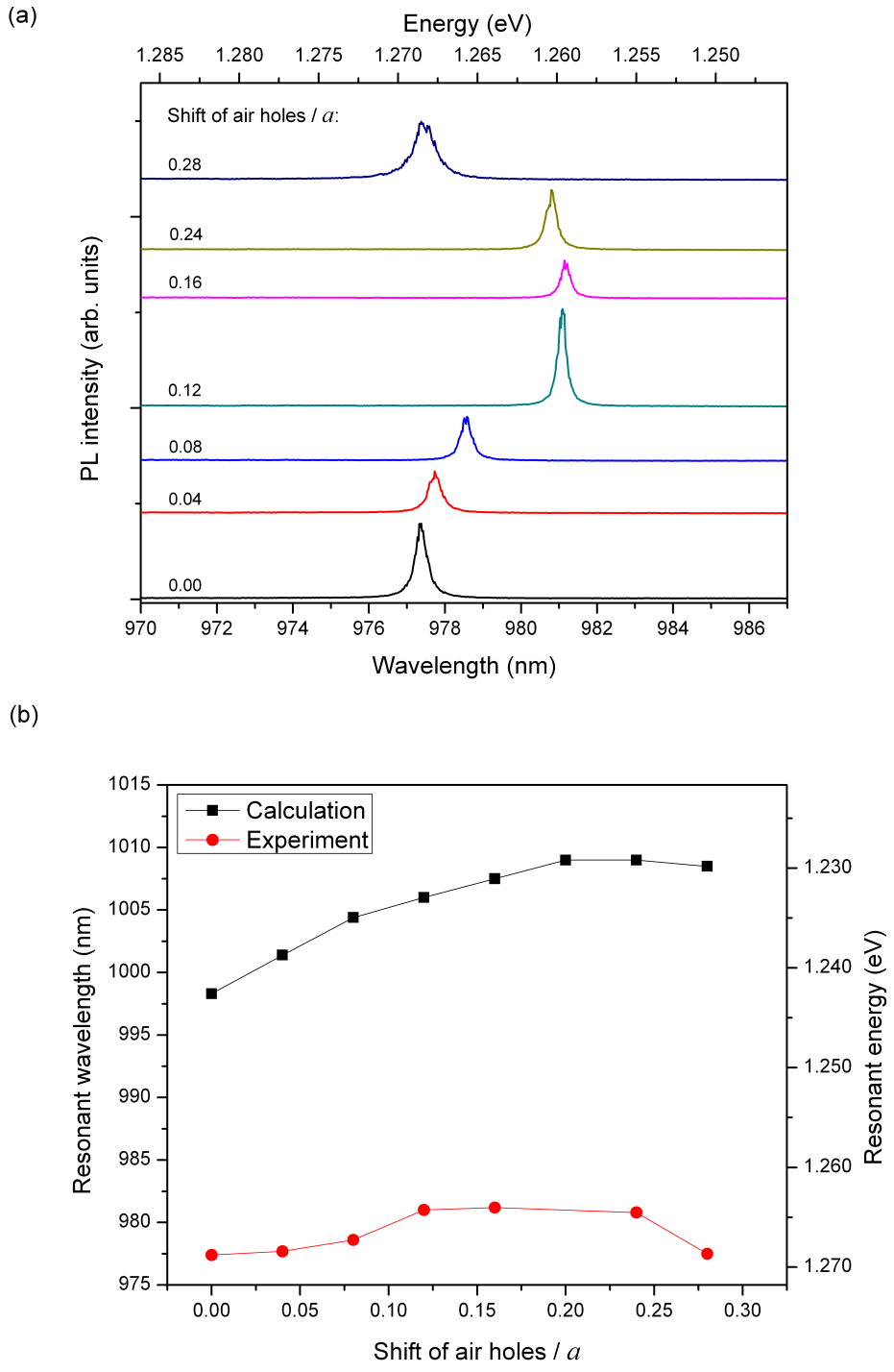

FIGURE A.10: (a) Measured PL spectra showing the fundamental mode of L3 PhC microcavities with different air holes shifts s. (b) The spectral position of the resonant wavelength of the fundamental mode as a function of the air holes shift.

Figure A.11 shows polarization-dependent PL measurements on an L3 cavity. High linear polarization degree up to 0.68 has been achieved. Finally, Fig. A.12 includes the calculated and measured Q-factors of H1 cavities as a function of s/a

for different displacement from zero to $0.28a$. A maximum Q value of 5000 has been realized for shift of $0.12a$.

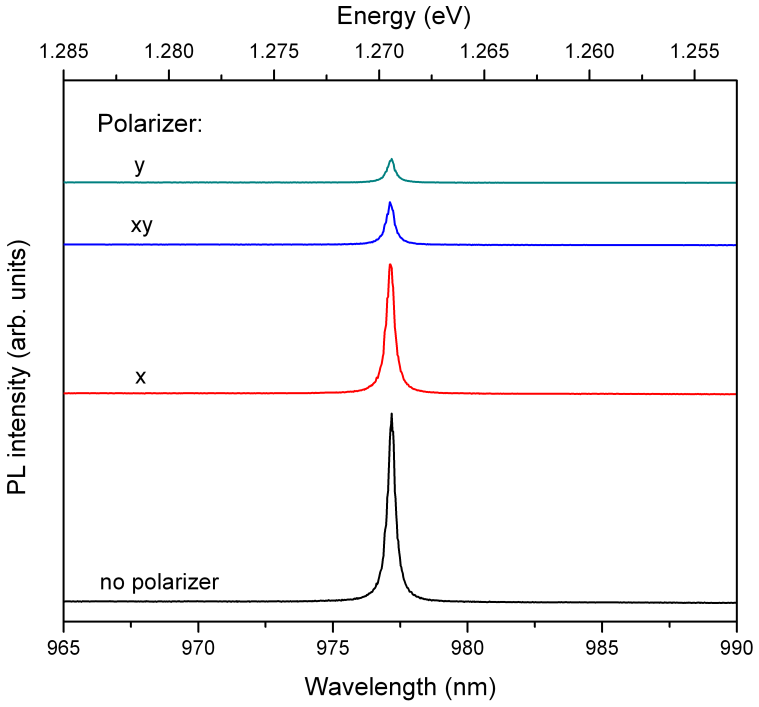

FIGURE A.11: PL spectra showing the polarization-dependent of the fundamental mode of an unmodified L3 cavity.

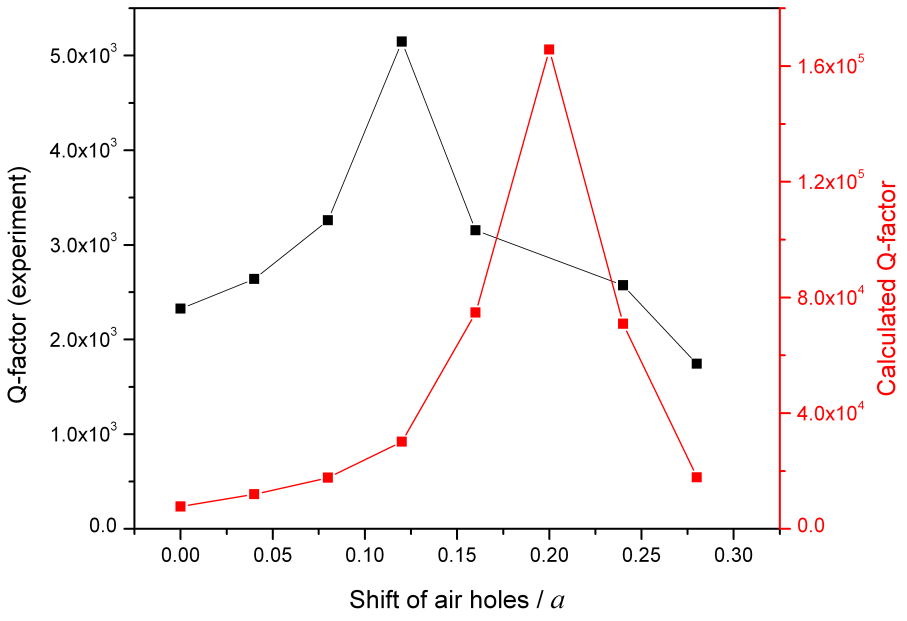

FIGURE A.12: Calculated and measured Q-factors of the fundamental mode of L3 cavity as a function of the displacement of the air holes (s/a). A maximum Q value of 5000 has been achieved for $s/a = 0.12$.

A.3 L5

The L5 PhC cavities are formed by omitting five holes in triangular PhC lattice (Fig. A.13(a)). Figures A.13(b) and c) show typical SEM images of an L5 cavity and a modified cavity with $s/a = 0.16$ are depicted in Figs. A.13(b) and (c), respectively. Owing to the large length of this type of cavities, electrically gated structures can be introduced, for example, for coupling of two quantum dot spins [145]. For our parameters, seven modes are present with one degenerate mode, as depicted in Fig. A.14.

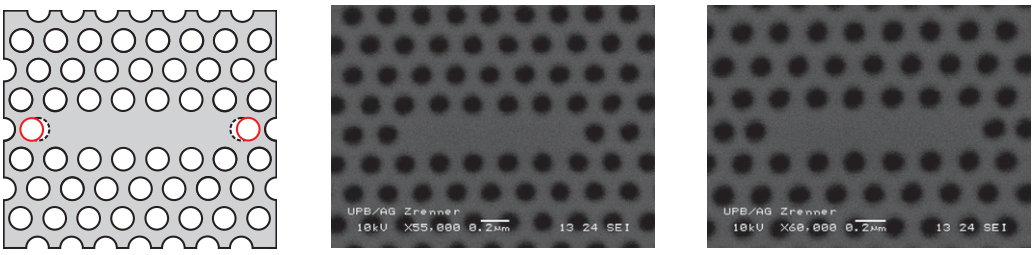

FIGURE A.13: (a) Modified L5 cavity structure. SEM images of (b) an L5 cavity and (c) a modified cavity with air holes shift of $s/a = 0.16$.

The Q-factor optimization of the fundamental mode (Fig. A.14(h)) can be achieved by shifting the air holes at both edges of the cavity, as illustrated in the red colored circles in Fig. A.13(a).

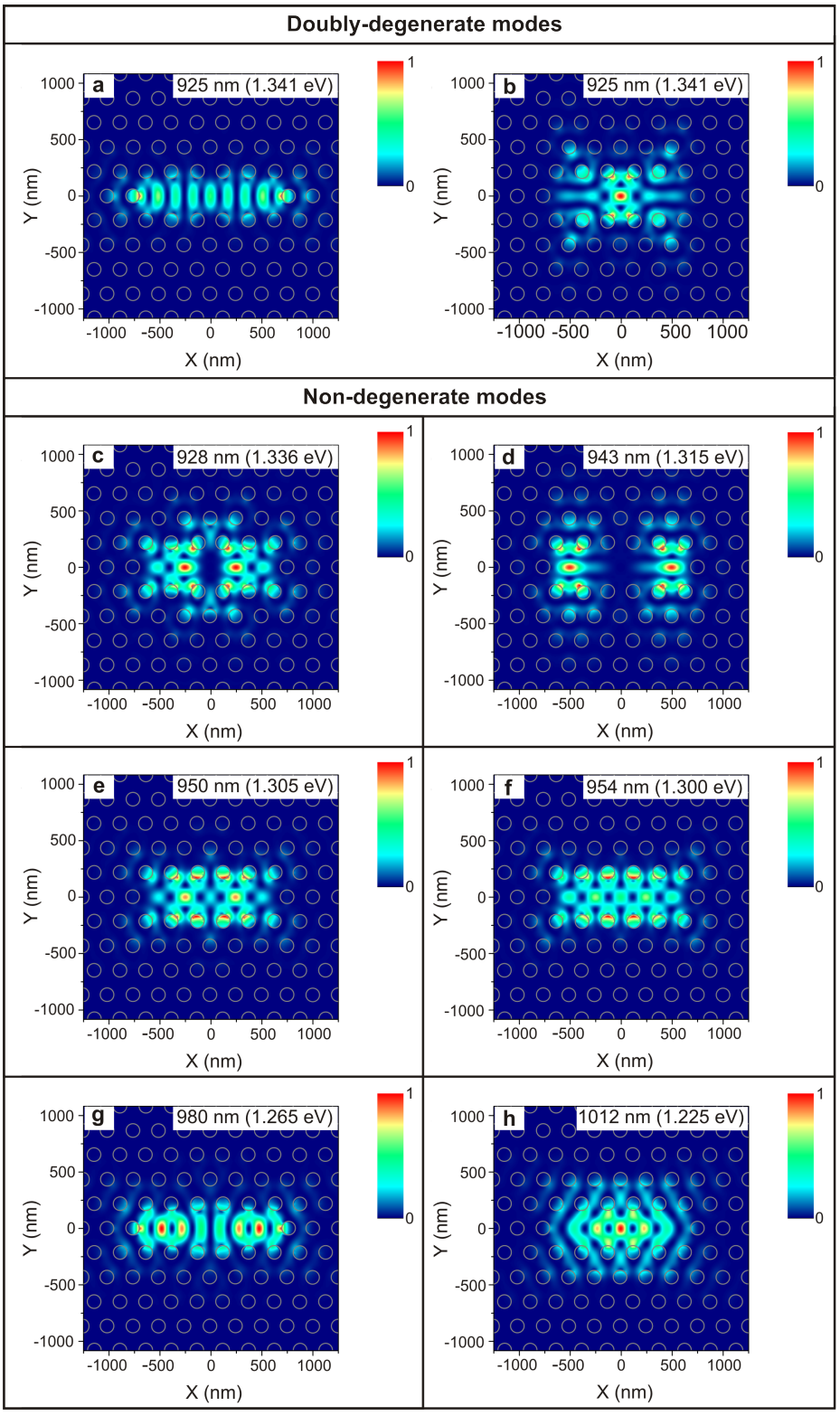

FIGURE A.14: Calculated electric field intensity profiles of L5 cavity modes with $a = 250$ nm, $r = 0.25a$, and $t = 0.72a$.

Figures A.15(a), (c), and (e) show the distribution of the electric field intensity and the corresponding FT spectra for different air holes shift for the fundamental mode. As the other types of cavities, the same behavior is also observed here. The field components are minimized at shift of $0.24a$, and consequently a maximum Q is expected.

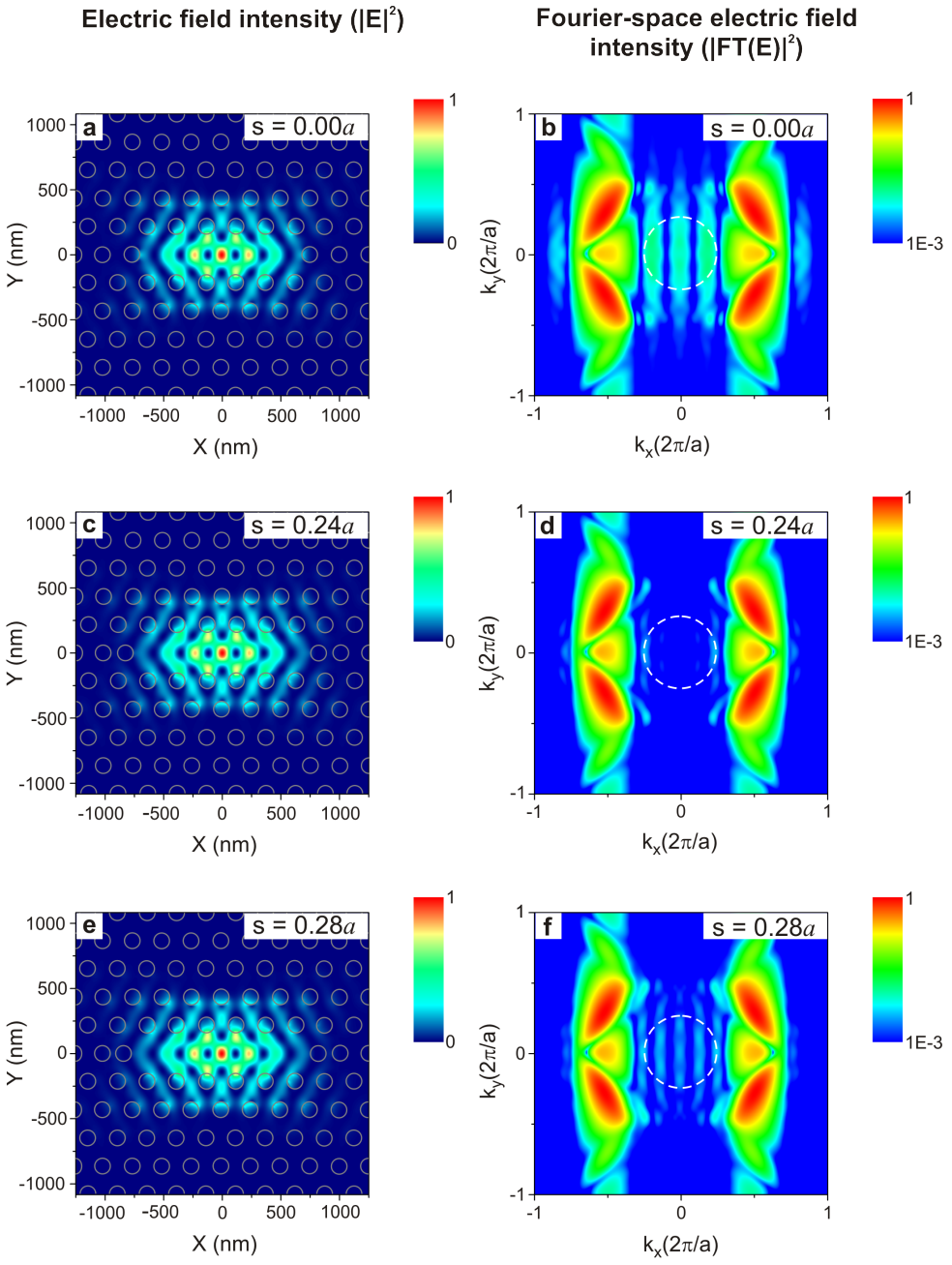

FIGURE A.15: Electric field intensity profiles of the fundamental mode of L5 PhC cavities with air holes shift of (a) zero, (c) $0.24a$, and (e) $0.28a$. The corresponding 2D Fourier transform of the electric field intensity $\left(|FT\,(E_x)|^2 + |FT\,(E_y)|^2\right)$ is plotted in graphs (b), (d), and (f). The dashed white circles in graphs (b), (d), and (f) represent the light cone boundary (the light line), which is defined by $k_x^2 + k_y^2 = (\omega/c)^2$. Note the reduction of the wavevector components inside the light line for shift of $0.24a$ (graph(d)).

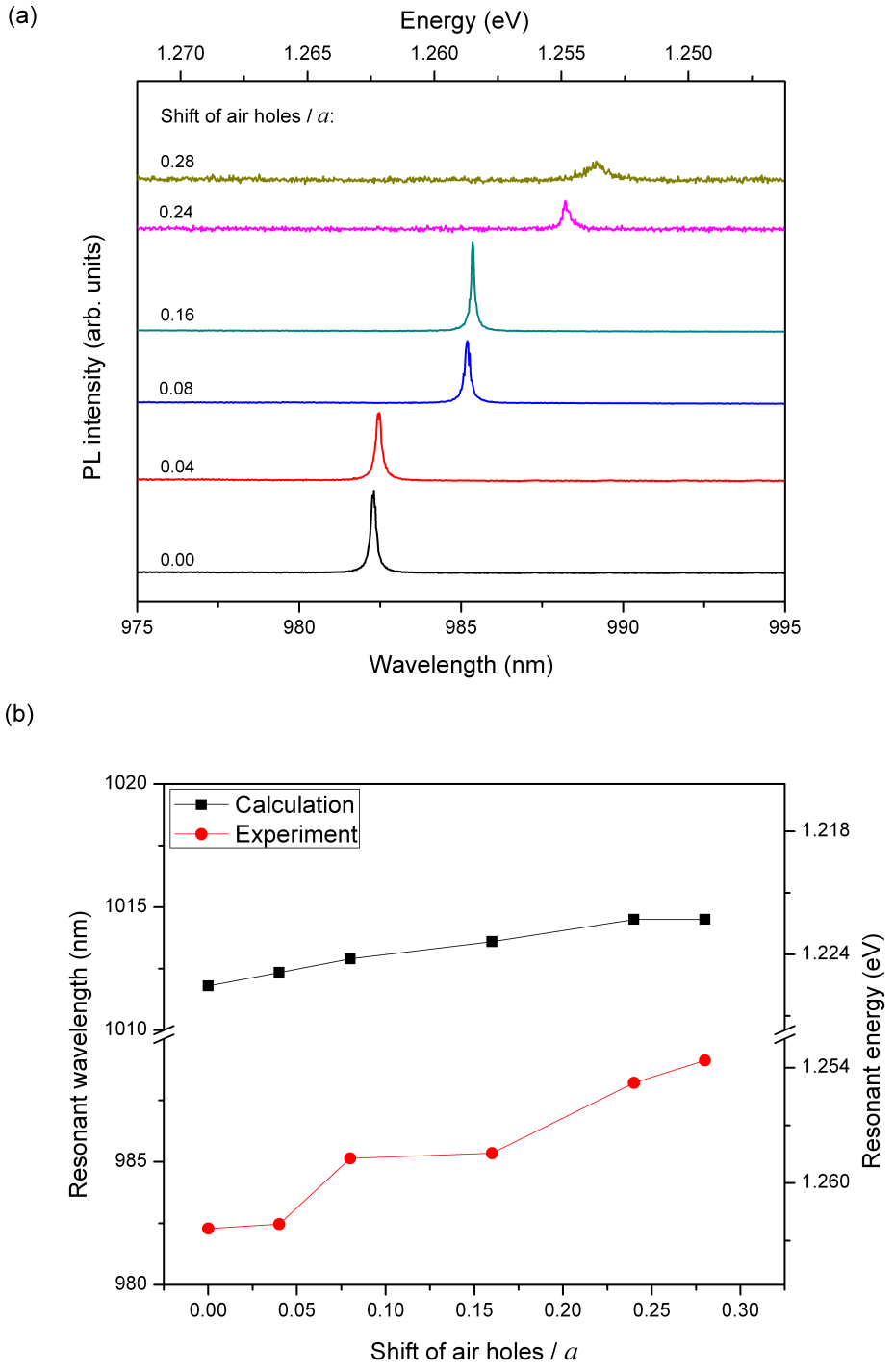

FIGURE A.16: (a) Measured PL spectra showing the fundamental mode of L5 PhC microcavities with different air holes displacements. (b) The spectral position of the resonant wavelength of the fundamental mode as a function of the air holes displacement.

The experimental measurements on L5 cavities with various air holes shifts are shown in Fig. A.16(a), where only the fundamental mode is shown. With increasing the shift of the inner holes, the resonance peak is redshifted due to the increase of the effiective cavity length. The wavelength of the cavity mode is plotted as a function of the displacement in Fig. A.16(b).

Figure A.17 shows polarization-dependent PL measurements on an L5 cavity. High linear polarization degree up to 0.6 has been realized. Finally, Fig. A.12 includes the calculated and measured Q-factors of L5 cavities as a function of s/a for different displacement from zero to $0.28a$. A maximum Q value of 9000 has been realized for shift of $0.16a$.

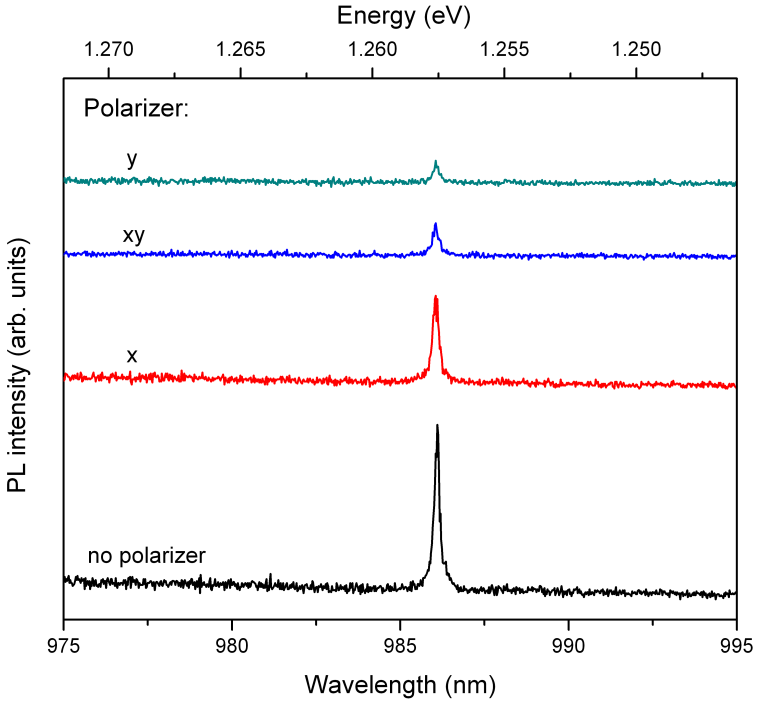

FIGURE A.17: Polarization-dependent PL spectra of the fundamental mode of a modified L5 PhC cavity with $s/a = 0.16$.

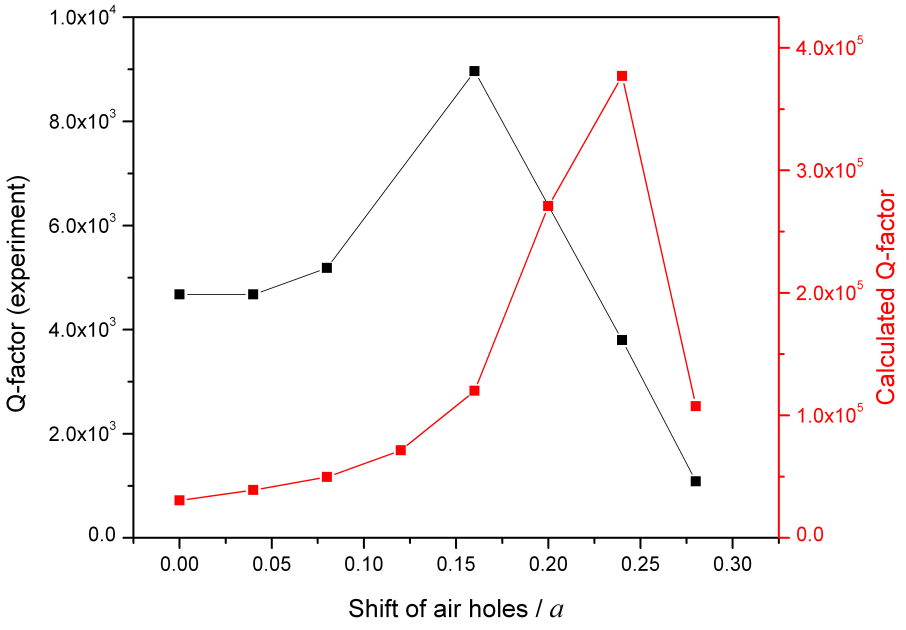

FIGURE A.18: Calculated and measured Q-factors of the fundamental mode of L5 cavity as a function of the displacement of the air holes (s/a). A maximum experimental Q value of 9000 has been achieved for $s/a = 0.16$.

Bibliography

[1] R. Dingle, W. Wiegmann, and C. H. Henry, *Quantum States of Confined Carriers in Very Thin $Al_xGa_{1-x}As$-GaAs-$Al_xGa_{1-x}As$ Heterostructures*, Phys. Rev. Lett. **33**, 827 (1974)

[2] K. v. Klitzing, G. Dorda, and M. Pepper, *New Method for High-Accuracy Determination of the Fine-Structure Constant Based on Quantized Hall Resistance*, Phys. Rev. Lett. **45**, 494 (1980)

[3] Y. Arakawa and H. Sakaki, *Multidimensional quantum well laser and temperature dependence of its threshold current*, Appl. Phys. Lett. **40**, 939 (1982)

[4] P. Michler, A. Kiraz, C. Becher,W. V. Schoenfeld, P.M. Petroff, L. Zhang, E. Hu, and A. Imamoğlu, *A quantum dot single-photon turnstile device*, Science **290**, 2282 (2000)

[5] Z. Yuan, B.E. Kardynal, R.M. Stevenson, A.J. Shields, C.J. Lobo, K. Cooper, N.S. Beattie, D.A. Ritchie, and M. Pepper, *Electrically Driven Single-Photon Source*, Science **295**, 102 (2002)

[6] H. Kamada and H. Gotoh, *Quantum computation with quantum dot excitons*, Semicond. Sci. Technol. **19**, S392 (2004)

[7] E. Waks, K. Inoue, C. Santori, D. Fattal, J. Vučković, G.S. Solomon, and Y. Yamamoto, *Secure communication: Quantum cryptography with a photon turnstile*, Nature **420**, 762 (2002)

[8] D. Fattal, E. Diamanti, K. Inoue, and Y. Yamamoto, *Quantum Teleportation with a Quantum Dot Single Photon Source*, Phys. Rev. Lett. **92**, 037904 (2004)

[9] J. Claudon, J. Bleuse, N. S. Malik, M. Bazin, P. Jaffrennou, N. Gregersen, C. Sauvan, P. Lalanne, and J. M. Gérard, *A highly efficient single-photon source based on a quantum dot in a photonic nanowire*, Nature Photon. **4**, 174 (2010)

[10] K. J. Vahala, *Optical microcavities*, Nature **424**, 839 (2003)

[11] J. M. Gérard, B. Sermage, B.Gayral, E. Costard, and V. Thierry-Mieg, *Enhanced Spontaneous Emission by Quantum Boxes in a Monolithic Optical Microcavity*, Phys. Rev. Lett. **81**, 1110 (1998)

[12] O. Gazzano, S. Michaelis de Vasconcellos, C. Arnold, A. Nowak, E. Galopin, I. Sagnes, L. Lanco, A. Lemaître, and P. Senellart, *Bright solid-state sources of indistinguishable single photons*, Nat. Commun. **4**, 1425 (2013)

[13] W. H. Chang, W. Y. Chen, H. S. Chang, T. P. Hsieh, J. I. Chyi, and T. M. Hsu, *Efficient single-photon sources based on low-density quantum dots in photonic-crystal nanocavities*, Phys. Rev. Lett. **96**, 117401 (2006)

[14] M. Kaniber, A. Kress, A. Laucht, M. Bichler, R. Meyer, M.-C. Amann, and J. J. Finley, *Efficient spatial redistribution of quantum dot spontaneous emission from two-dimensional photonic crystals*, Appl. Phys. Lett. **91**, 061106 (2007)

[15] A. Faraon, E. Waks, D. Englund, I. Fushman, and J. Vučković, *Efficient photonic crystal cavity-waveguide couplers*, Appl. Phys. Lett. **90**, 073102 (2007)

[16] K. Nozaki, H. Watanabe, and T. Baba, *Photonic crystal nanolaser monolithically integrated with passive waveguide for effective light extraction*, Appl. Phys. Lett. **92**, 021108 (2008)

[17] L. Lu, A. Mock, and J. O'Brien, *Efficient coupling between a photonic crystal nanocavity and a waveguide with directional end-facet emission*, J. Opt. **14** 055502 (2012)

[18] A. Laucht, F. Hofbauer, N. Hauke, J. Angele, S. Stobbe, M. Kaniber, G. Bühm, P. Lodahl, M. C. Amann, and Finley, *Electrical control of spontaneous emission and strong coupling for a single quantum dot*, New J. Phys. **11**, 023034 (2009)

[19] H. Kim, S. M. Thon, P. M. Petroff, and D. Bouwmeester, *Independent tuning of quantum dots in a photonic crystal cavity*, Appl. Phys. Lett. **95**, 243107 (2009)

[20] E. Yablonovitch, *Inhibited Spontaneous Emission in Solid-State Physics and Electronics*, Phys. Rev. Lett. **58**, 2059 (1987)

[21] S. John, *Strong localization of photons in certain disordered dielectric superlattices*, Phys. Rev. Lett. **58**, 2486 (1987)

[22] J. D. Joannopoulos, S. G. Johnson, J. N. Winn, and R. D. Meade, *Photonic Crystals: Molding the Flow of Light*, Princeton University Press, Second Edition (2008)

[23] J. M. Lourtioz, H. Benisty, V. Berger, J. M. Gérard, D. Maystre, and A. Tchelnokov, *Photonic Crystals: Towards Nanoscale Photonic Devices*, Springer, Second Edition (2008)

[24] S. Noda, K. Tomoda, N. Yamamoto, and A. Chutinan, *Full Three-Dimensional Photonic Bandgap Crystals at Near-Infrared Wavelengths*, Science **289**, 604 (2000)

[25] Y. Akahane, T. Asano, B.-S. Song, and S. Noda, *High-Q photonic nanocavity in a two-dimensional photonic crystal*, Nature **425**, 944 (2003)

[26] J. Vučković, M. Lončar, H. Mabuchi, and A. Scherer, *Design of photonic crystal microcavities for cavity QED*, Phys. Rev. E **65**, 016608 (2001)

[27] J. Vučković, M. Lončar, H. Mabuchi, and A. Scherer, *Optimization of the Q factor in photonic crystal microcavities*, IEEE J. Quantum Electron. **38**, 850 (2002)

[28] J. Vučković and Y. Yamamoto, *Photonic crystal microcavities for cavity quantum electrodynamics with a single quantum dot*, Appl. Phys. Lett. **82**, 2374 (2003)

[29] S.-H. Kim, S.-K. Kim, and Y.-H. Lee, *Vertical beaming of wavelength-scale photonic crystal resonators*, Phys. Rev. B **73**, 235117 (2006)

[30] H.-Y. Ryu, M. Notomi, G.-H. Kim, and Y.-H. Lee, *High quality-factor whispering-gallery mode in the photonic crystal hexagonal disk cavity*, Opt. Express **12**, 1708 (2004)

[31] H.-Y. Ryu, M. Notomi, and Y.-H. Lee, *High-quality-factor and small-mode-volume hexapole modes in photonic-crystal-slab nanocavities*, Appl. Phys. Lett. **83**, 4294 (2003)

[32] T. Yoshie, A. Scherer, J. Hendrickson, G. Khitrova, H. M. Gibbs, G. Rupper, C. Ell, O. B. Shchekin, and D. G. Deppe, *Vacuum Rabi splitting with a single quantum dot in a photonic crystal nanocavity*, Nature **432**, 200 (2004)

[33] L. Jacak, P. Hawrylak, and A.Wojs, *Quantum Dots,* Springer (1998)

[34] D. Bimberg, *Semiconductor Nanostructures*, Springer (2008)

[35] A. Zrenner, *A close look on single quantum dots*, J. Chem. Phys. **112**, 7790 (2000)

[36] P. Michler, *Single Semiconductor Quantum Dots*, Springer (2009)

[37] M. A. Reed, R. T. Bate, K. Bradshaw, W. M. Duncan, W. R. Frensley, J. W. Lee, and H. D. Shih, *Spatial quantization in GaAs-AlGaAs multiple quantum dots*, J. Vac. Sci. Technol. B **4**, 358 (1986)

[38] A. Zrenner, L. V. Butov, M. Hagn, G. Abstreiter, G. Böhm, and G. Weimann, *Quantum dots formed by interface fluctuations in AlAs/GaAs coupled quantum well structures*, Phys. Rev. Lett. **72**, 3382 (1994)

[39] C. B. Murray, D. J. Norris, and M. G. Bawendi, *Synthesis and characterization of nearly monodisperse CdE (E = S, Se, Te) semiconductor nanocrystallites*, J. Amer. Chem. Soc. **115**, 8706 (1993)

[40] R. Hanson, L. P. Kouwenhoven, J. R. Petta, S. Tarucha, and L. M. K. Vandersypen, *Spins in few-electron quantum dots*, Rev. Mod. Phys. **79**, 1217 (2007)

[41] D. Leonard, M. Krishnamurthy, C. M. Reeves, S. P. Denbaars, and P. M. Petroff, *Direct formation of quantum-sized dots from uniform coherent islands of InGaAs on GaAs surfaces*, Appl. Phys. Lett. **63**, 3203 (1993)

[42] J.-Y. Marzin, J.-M. Gérard, A. Izral, D. Barrier, and G. Bastard, *Photoluminescence of Single InAs Quantum Dots Obtained by Self-Organized Growth on GaAs*, Phys. Rev. Lett. **73**, 716 (1994)

[43] Q. Xie, A. Madhukar, P. Chen, and N. P. Kobayashi, *Vertically Self-Organized InAs Quantum Box Islands on GaAs(100)*, Phys. Rev. Lett. **75**, 2542 (1995)

[44] F. Findeis, *Optical Spectroscopy on Single Self-assembled Quantum Dots*, PhD thesis, TU München (2001)

[45] B.D. Gerardot, G. Subramanian, S. Minvielle, H. Lee, J.A. Johnson, W.V. Schoenfeld, D. Pine, J.S. Speck and P.M. Petroff, *Self-assembling quantum dot lattices through nucleation site engineering*, J. Cryst. Growth **236**, 647 (2002)

[46] I. N. Stranski and L. Krastanov, *Zur Theorie der orientierten Ausscheidung von Ionenkristallen aufeinander*, Sitzungsber. Akad. Wiss. Wien, Math.-naturwiss. Kl. IIb **146**, 797 (1938)

[47] M. Grundmann, N. N. Ledentsov, R. Heitz, L. Eckey, J. Christen, J. Böhrer, D. Bimberg, S. S. Ruvimov, P. Werner, U. Richter, J. Heydenreich, V. M. Ustinov, A. Y. Egorov, A. E. Zhukov, P. S. Kopev, and Z. I. Alferov, *InAs/GaAs quantum dots radiative recombination from zero-dimensional states*, Phys. Status Solidi B **188**, 249 (1995)

[48] R. Notzel, J. Temmyo, A. Kozen, T. Tamamura, T. Fukui, and H. Hasegawa, *Self-organization of strained GaInAs microstructures on InP (311) substrates grown by metalorganic vapor-phase epitaxy*, Appl. Phys. Lett. **66**, 2525 (1995)

[49] A. Wojs, P. Hawrylak, S. Fafard, and L. Jacak, *Electronic structure and magneto-optics of self-assembled quantum dots*, Phys. Rev. B, **54**, 5604 (1996)

[50] M. Mehta, D. Reuter, A. Melnikov, A. D. Wieck, and A. Remhof, *Focused ion beam implantation induced site-selective growth of InAs quantum dots*, Appl. Phys. Lett. **91**, 123108 (2007)

[51] N. Kirstaedter, N.N. Ledentsov, M. Grundmann, D. Bimberg, V.M. Ustinov, S.S. Ruvimov, M.V. Maximov, P.S. Kop'ev, Zh.I. Alferov, U. Richter, P. Werner, U. Gösele, and J. Heydenreich, *Low threshold, large T_0 injection laser emission from (InGa)As quantum dots*, Electron. Lett. **30**, 1416 (1994)

[52] U. Hohenester and E. Molinari, *Role of Coulomb Correlations in the Optical Spectra of Semiconductor Quantum Dots*, Phys. Status Solidi B **221**, 19 (2000)

[53] P. Hawrylak, *Excitonic artificial atoms: Engineering optical properties of quantum dots*, Phys. Rev. B **60**, 5597 (1999)

[54] S. Reimann and M. Manninen, *Electronic structure of quantum dots*, Rev. Mod. Phys. **74**, 1283 (2002)

[55] M. Bayer, S. N. Walck, T. L. Reinecke, and A. Forchel, *Exciton binding energies and diamagnetic shifts in semiconductor quantum wires and quantum dots*, Phys. Rev. B, **57** 6584 (1998)

[56] H.J. Krenner, S. Stufler, M. Sabathil, E.C. Clark, P. Ester, M. Bichler, G. Abstreiter, J.J. Finley, and A. Zrenner, *Recent advances in exciton-based quantum information processing in quantum dot nanostructures*, New J. Phys. **7**, 184 (2005)

[57] P. Ester, L. Lackmann, S. M. de Vasconcellos, M. C. Hübner, A. Zrenner, and M. Bichler, *Single photon emission based on coherent state preparation*, Appl. Phys. Lett. **91**, 111110 (2007)

[58] T. Meier, P. Thomas, and S. W. Koch, *Coherent Semiconductor Optics: From Basic Concepts to Nanostructure Applications*, Springer (2006)

[59] D. Miller, D. Chemla, T. Damen, T.Wood, C. Burrus, A. Gossard, and W.Wiegmann, *Band-edge electroabsorption in quantum well structures:The quantum-confined Stark effect*, Phys. Rev. Lett. **53**, 2173 (1984)

[60] D. Miller, D. Chemla, T. Damen, A. Gossard, W. Wiegmann, T. Wood, and C. Burrus, *Electric field dependence of optical absorption near the band gap of quantum-well structures*, Phys. Rev. B **32**, 1043 (1985)

[61] S. Benner and H. Haug, *Influence of external electric and magnetic fields on the excitonic absorption spectra of quantum-well wires*, Phys. Rev. B **47**, 15750 (1993)

[62] T. Arakawa, Y. Kato, F. Sogawa, and Y. Arakawa, *Photoluminescence studies of GaAs quantum wires with quantum confined Stark effect*, Appl. Phys. Lett. **70**, 646 (1997)

[63] W. Heller, U. Bockelmann, and G. Abstreiter, *Electric-field effects on excitons in quantum dots*, Phys. Rev. B **57**, 6270 (1998)

[64] S. A. Empedocles and M. G. Bawendi, *Quantum-Confined Stark Effect in Single CdSe Nanocrystallite Quantum Dots*, Science **278**, 2114 (1997)

[65] S. Raymond, J. P. Reynolds, J. L. Merz, S. Fafard, Y. Feng, and S. Charbonneau, *Asymmetric Stark shift in* $Al_xIn_{1-x}As/Al_yGa_{1-y}As$ *self-assembled dots*, Phys. Rev. B **58**, R13415 (1998)

[66] P. W. Fry, I. E. Itskevich, D. J. Mowbray, M. S. Skolnick, J. J. Finley, J. A. Barker, E. P. O'Reilly, L. R. Wilson, I. A. Larkin, P. A. Maksym, M. Hopkinson, M. Al- Khafaji, J. P. R. David, A. G. Cullis, G. Hill, and J. C. Clark, *Inverted Electron-Hole Alignment in InAs-GaAs Self-Assembled Quantum Dots*, Phys. Rev. Lett. **84**, 722 (2000)

[67] F. Findeis, M. Baier, E. Beham, A. Zrenner, and G. Abstreiter, *Photocurrent and photoluminescence of a single self-assembled quantum dot in electric fields*, Appl. Phys. Lett. **78**, 2958 (2001)

[68] Q. Xie, J. Brown, R. Jones, J. V. Nostrand, and K. Leedy, *Growth of vertically self-organized InGaAs quantum dots with narrow inhomogeneous broadening*, Appl. Phys. Lett. **76**, 3082 (2000)

[69] A. Zrenner, M. Markmann, A. Paassen, A. L. Efros, M. Bichler, W. Wegscheider, G. Böhm, and G. Abstreiter, *Spatially resolved magneto-optics on confined systems*, Physica B **256**, 300 (1998)

[70] L. Chu, M. Arzberger, A. Zrenner, G. Böhm, and G. Abstreiter, *Polarization dependent photocurrent spectroscopy of InAs/GaAs quantum dots*, Appl. Phys. Lett. **75**, 2247 (1999)

[71] W.-H. Chang, T. M. Hsu, C. C. Huang, S. L. Hsu, C. Y. Lai, N. T. Yeh, T. E. Nee, and J. -I. Chyi, *Photocurrent studies of the carrier escape process from InAs self-assembled quantum dots*, Phys. Rev. B **62**, 6959 (2000)

[72] A. Zrenner, E. Beham, S. Stufler, F. Findeis, M. Bichler, and G. Abstreiter, *Coherent properties of a two-level system based on a quantum-dot photodiode*, Nature **418**, 612 (2002)

[73] L. Allen and J. H. Eberly, *Optical Resonance and Two-Level Atoms*, Dover Publications, New York (1987)

[74] M. Fox, *Quantum Optics: An Introduction*, Oxford University Press (2006)

[75] P. Ester, *Coherent Properties of Singe Quantum Dot Transitions and Single Photon Emission*, PhD thesis, Universität Paderborn (2008)

[76] S. Stufler, P. Ester, A. Zrenner, and M. Bichler, *Ramsey Fringes in an Electric-Field-Tunable Quantum Dot System*, Phys. Rev. Lett. **96**, 037402 (2006)

[77] S. Stufler, P. Ester, A. Zrenner, and M. Bichler, *Quantum optical properties of a single $In_xGa_{1-x}As$-GaAs quantum dot two-level system*, Phys. Rev. B **72**, 121301 (2005)

[78] P. Borri and W. Langbein, *Four-wave mixing dynamics of excitons in InGaAs self-assembled quantum dots*, J. Phys.: Condens. Matter **19**, 295201 (2007)

[79] V. Zwiller, T. Aichele, and O. Benson, *Quantum optics with single quantum dot devices*, New J. Phys. **6**, 96 (2004)

[80] S. Noda, *Seeking the ultimate nanolaser*, Science **314**, 260 (2006)

[81] P. Michler, *Single Quantum Dots: Fundamentals, Application, and New Concepts*, Springer Series in Topics in Applied Physics Vol. **90**, Springer (2003)

[82] L. Andreani, G. Panzarini, and J. M. Gérard, *Strong-coupling regime for quantum boxes in pillar microcavities: Theory*, Phys. Rev. B. **60**, 13267 (1999)

[83] A. Kiraz, P. Michler, C. Becher, B. Gayral, A. Imamoğlu, L. Zhang, E. Hu, W. V. Schoenfeld, and P. M. Petroff, *Cavity-quantum electrodynamics using a single InAs quantum dot in a microdisk structure*, Appl. Phys. Lett. **78**, 3932 (2001)

[84] C. Santori, D. Fattal, J. Vučković, G. S. Solomon, and Y.Yamamoto, *Indistinguishable photons from a single-photon device*, Nature **419**, 594 (2002)

[85] S. Strauf, K. Hennessy, M.T. Rakher, Y.-S. Choi, A. Badolato, L.C. Andreani, E.L. Hu, P.M. Petroff, and D. Bouwmeester, *Self-tuned quantum dot gain in photonic crystal lasers*, Phys. Rev. Lett. **96**, 127404 (2006)

[86] C. Weisbuch, M. Nishioka, A. Ishikawa, and Y. Arakawa, *Observation of the coupled exciton-photon mode splitting in a semiconductor quantum microcavity*, Phys. Rev. Lett. **69**, 3314 (1992)

[87] A. Tredicucci, Y. Chen, V. Pellegrini V, M. Börger, L. Sorba, F. Beltram, and F. Bassani, *Controlled Exciton-Photon Interaction in Semiconductor Bulk Microcavities*, Phys. Rev. Lett. **75**, 3906 (1995)

[88] J. P. Reithmaier, G. Sek, A. Löffler, C. Hofmann, S. Kuhn, S. Reitzenstein, L. V. Keldysh, V. D. Kulakovskii, T. L. Reinecke, and A. Forchel, *Strong coupling in a single quantum dot semiconductor microcavity system*, Nature **432**, 197 (2004)

[89] D. Englund, A. Faraon, I. Fushman, N. Stoltz, P. Petroff, and J. Vučković, *Controlling cavity reflectivity with a single quantum dot*, Nature **450**, 857 (2007)

[90] S. Rudin, and T. L. Reinecke, *Oscillator model for vacuum Rabi splitting in microcavities*, Phys. Rev. B **59**, 10227 (1999)

[91] J.P. Reithmaier, G. Sek, A. Löffler, C. Hofmann, S. Kuhn, S. Reitzenstein, L.V. Keldysh, V.D. Kulakovskii, T.L. Reinecke, and A. Forchel, *Strong coupling in a single quantum dot-semiconductor microcavity system*, Nature **432**, 197 (2004)

[92] J. P. Reithmaier, *Strong exciton-photon coupling in semiconductor quantum dot systems*, Semicond. Sci. Technol. **23**, 123001 (2008)

[93] D. Sanvitto, A. Daraei, A. Tahraoui, M. Hopkinson, P. W. Fry, D. M. Whittaker, and M. S. Skolnick, *Observation of ultrahigh quality factor in a semiconductor microcavity*, Appl. Phys. Lett. **86**, 191109 (2005)

[94] K. Srinivasan and O. Painter, *Linear and nonlinear optical spectroscopy of a strongly coupled microdisk-quantum dot system*, Nature, **450**, 862 (2007)

[95] S. Reitzenstein, C. Hofmann, A. Gorbunov, M. Strau, S. H. Kwon, C. Schneider, A. Löffler, S. Höfling, M. Kamp, and A. Forchel, *AlAs/GaAs micropillar cavities with quality factors exceeding 150.000*, Appl. Phys. Lett. **90**, 251109 (2007)

[96] Y. Ota, M. Shirane, M. Nomura, N. Kumagai, S. Ishida, S. Iwamoto, S. Yorozu, and Y. Arakawa, *Vacuum Rabi splitting with a single quantum dot embedded in a H1 photonic crystal nanocavity*, Appl. Phys. Lett. **94**, 033102 (2009)

[97] D. Englund, A. Faraon, B. Zhang, Y. Yamamoto, and J. Vučković, *Generation and transfer of single photons on a photonic crystal chip*, Opt. Express **15**, 5550 (2007)

[98] H. Y. Ryu, S. H. Kwon, Y. J. Lee, Y. H. Lee, and J. S. Kim, *Very-low-threshold photonic band-edge lasers from free-standing triangular photonic crystal slabs*, Appl. Phys. Lett. **80**, 3476 (2002)

[99] S. G. Johnson, S. Fan, P. R. Villeneuve, J. D. Joannopoulos, and L. A. Kolodziejski, *Guided modes in photonic crystal slabs*, Phys. Rev. B **60**, 5751 (1999)

[100] E. Yablonovitch, T. J. Gmitter, R. D. Meade, A. M. Rappe, K. D. Brommer, and J. D. Joannopoulos, *Donor and acceptor modes in photonic band-structure*, Phys. Rev. Lett. **67**, 3380 (1991)

[101] K. Srinivasan and O. Painter, *Momentum space design of high-Q photonic crystal optical cavities*, Opt. Express **10**, 670 (2002)

[102] A. Korkin and F. Rosei, *Nanoelectronics and Photonics*, Springer (2008)

[103] K. S. Yee, *Numerical solution of initial boundary value problems involving Maxwell's equations in isotropic media*, IEEE Trans. Antennas Propag. **14**, 302 (1966)

[104] A. Taflove and S. C. Hagness, *Computational Electrodynamics: The finite-difference time-domain method*, Third Edition, Artech House, (2005)

[105] T. Asano, B. Song, and S. Noda, *Analysis of the experimental Q factors (∼ 1 million) of photonic crystal nanocavities*, Opt. Express **14**, 1996 (2006)

[106] M-K. Kim, J-K. Yang, Y-H. Lee, and I-K Hwang, *Influence of etching slope on two-dimensional photonic crystal slab resonators*, J. Korean Phys. Soc. **50**, 1027 (2007)

[107] K. Srinivasan, P. E. Barclay, O. Painter, J. Chen, and A. Y. Cho, *Fabrication of high-quality-factor photonic crystal microcavities in InAsP/InGaAsP membranes*, J. Vac. Sci. Technol. B **22**, 875 (2004).

[108] K. Hennessy, C. Reese, A. Badolato, C. F. Wang, A. Imamoğlu, P. M. Petroff, and E. Hu, *Fabrication of high Q square-lattice photonic crystal microcavities*, J. Vac. Sci. Technol. B **21**, 2918 (2003)

[109] J. D. Chinn, I. Adesida, E. D. Wolf, and R. C. Tiberio, *Reactive ion etching for submicron structures*, J. Vac. Sci. Technol. **19**, 1418 (1981)

[110] S. J. Pearton, U. K. Chakrabarti, W. S. Hobson, and A. P. Kinsella, *Reactive ion etching of GaAs, AlGaAs, and GaSb in Cl_2 and $SiCl_4$*, J. Vac. Sci. Technol. B **8**, 607 (1990)

[111] E. Yablonovitch, T. Gmitter, J. P. Harbison, and R. Bhat, *Extreme selectivity in the lift-off of epitaxial gaas films*, Appl. Phys. Lett. **51**, 2222 (1987)

[112] M. C. Hübner, *Temperaturabhängige Eigenschaften einzelner Halbleiter-Quantenpunkte im kohärenten Regime*, PhD Dissertation, Universität Paderborn (2009)

[113] S. G. Johnson and J. D. Joannopoulos, *Block-iterative frequency-domain methods for Maxwell's equations in a planewave basis*, Opt. Express **8**, 173-190 (2001)

[114] C. Reese, B. Gayral, B. D. Gerardot, A. Imamoğlu, P. M. Petroff, and E. Hu, *High-Q photonic crystal microcavities fabricated in a thin GaAs membrane*, J. Vac. S. Tech. B **19**, 2749 (2001)

[115] T. D. Happ, I. I. Tartakovskii, V. D. Kulakovskii, J.-P. Reithmaier, M. Kamp, and A. Forchel, *Enhanced light emission of $In_xGa_{1-x}As$ quantum dots in a two-dimensional photonic-crystal defect microcavity*, Phys. Rev. B **66**, 041303(R) (2002)

[116] C. Reese, B. Gayral, B. D. Gerardot, A. Imamoğlu, P. M. Petroff, and E. Hu, *High-Q photonic crystal microcavities fabricated in a thin GaAs membrane*, J. Vac. Sci. Technol. B **19**, 2749 (2001)

[117] A. Kress, F. Hofbauer, N. Reinelt, H. J. Krenner, M. Bichler, D. Schuh, R. Meyer, G. Abstreiter, and J. J. Finley, *Investigation of cavity modes and direct observation of Purcell enhancement in 2Dphotonic crystal defect microcavities*, Physica E **26**, 351 (2005)

[118] Lumerical Solutions, Inc., *FDTD Solutions*, http://www.lumerical.com

[119] M. Nomura, S. Iwamoto, T. Nakaoka, S. Ishida, and Y. Arakawa, *Localized excitation of InGaAs quantum dots by utilizing a photonic crystal nanocavity*, Appl. Phys. Lett. **88**, 141108 (2006)

[120] S. G. Johnson, S. Fan, A. Mekis, and J. D. Joannopoulos, *Multipole-cancellation mechanism for high-Q cavities in the absence of a complete photonic band gap*, Appl. Phys. Lett. **78**, 3388 (2001)

[121] E. Purcell, *Spontaneous emission probabilities at radio frequencies*, Phys. Rev. **69**, 681 (1946)

[122] J. Hendrickson, B. C. Richards, J. Sweet, S.Mosor, C. Christenson, D. Lam, G. Khitrova, H. M. Gibbs, T. Yoshie, A. Scherer, O. B.Shchekin, and D. G. Deppe, *Quantum dot photonic-crystal-slab nanocavities: Quality factors and lasing*, Phys. Rev. B **72**, 193303 (2005).

[123] G. B. Hocker and C. L. Tang, *Observation of the optical transient nutation effect*, Phys. Rev. Lett. **21**, 591 (1968)

[124] C. Fürst, A. Leitenstorfer, A. Nutch, G. Tränkle, and A. Zrenner, *Ultrafast Rabi Oscillations of Free-Carrier Transitions in InP*, Phys. Stat. Sol. B **204**, 20 (1997)

[125] S. T. Cundiff, A. Knorr, J. Feldmann, S. W. Koch, E. O. Göbel, and H. Nickel, *Rabi flopping in semiconductors*, Phys. Rev. Lett. **73**, 1178 (1994)

[126] T. H. Stievater, X. Li, D. G. Steel, D. Gammon, D. S. Katzer, D. Park, C. Piermarocchi, and L. J. Sham, *Rabi oscillations of excitons in single quantum dots*, Phys. Rev. Lett. **87**, 133603 (2001)

[127] P. Borri, W. Langbein, S. Schneider, U. Woggon, R. L. Sellin, D. Ouyang, and D. Bimberg, *Rabi oscillations in the excitonic ground-state transition of InGaAs quantum dots*, Phys. Rev. B **66**, 081306(R) (2002)

[128] S. Mosor, J. Hendrickson, B. C. Richards, J. Sweet, G. Khitrova, H. M. Gibbs, T. Yoshie, A. Scherer, O. B. Shchekin, and D. G. Deppe, *Scanning a photonic crystal slab nanocavity by condensation of xenon*, Appl. Phys. Lett. **87**, 141105 (2005)

[129] A. Badolato, K. Hennessy, M. Atatüre, J. Dreiser, E. Hu, P. M. Petroff, and A. Imamoğlu, *Deterministic Coupling of Single Quantum Dots to Single Nanocavity Modes*, Science **308**, 1158 (2005)

[130] A. Högele, S. Seidl, M. Kroner, K. Karrai, R. J. Warburton, B. D. Gerardot, and P. M. Petroff, *Voltage-Controlled Optics of a Quantum Dot*, Phys. Rev. Lett. **93**, 217401 (2004)

[131] D. Haft, C. Schulhauser, A. Q. Govorov, R. J. Warburton, K. Karrai, J. M. Garcia, W. Schoedfeld, and P. M. Petroff, *Magneto-optical properties of ring-shaped self-assembled InGaAs quantum dots*, Physica E **13**, 165 (2002)

[132] S. Seidl, M. Kroner, A. Högele, K. Karrai, R. J. Warburton, A. Badolato, and P. M. Petroff, *Effect of uniaxial stress on excitons in a self-assembled quantum dot*, Appl. Phys. Lett. **88**, 203113 (2006)

[133] S. Paul, J. B. Roy, and P. K. Basu, *Empirical expressions for the alloy composition and temperature dependence of the band gap and intrinsic carrier density in* $Ga_xIn_{1-x}As$, J. Appl. Phys. **69**, 827 (1991)

[134] S. Vignolinia, F. Intontia, F. Ribolia, M. Zania, A. Vinattieria, D. S. Wiersma, M. Colocci, L. Balet, L. Li, M. Francardi, A. Gerardino, A. Fiore, and M. Gurioli, *Sub-wavelength probing and modification of photonic crystal nano-cavities*, Photonics and Nanostructures - Fundamentals and Applications **8**, 78 (2010)

[135] D. Englund, A. Faraon, I. Fushman, N. Stoltz, P. Petroff, and J. Vučković, *Controlling cavity reflectivity with a single quantum dot*, Nature **450**, 857 (2007)

[136] S. Ates, S. M. Ulrich, A. Ulhaq, S. Reitzenstein, A. Löffler, S. Höfling, A. Forchel, and P. Michler, *Non-resonant dot-cavity coupling and its potential for resonant single-quantum-dot spectroscopy*, Nature Photon. **3**, 724 (2009)

[137] M. Kaniber, A. Neumann, A. Laucht, M. F. Huck, M. Bichler, M.-C. Amann, and J. J. Finley, *Efficient and selective cavity-resonant excitation for single photon generation*, New J. Phys. **11**, 013031 (2009)

[138] F. Findeis, A. Zrenner, G. Böhm, and G. Abstreiter, *Phonon-assisted biexciton generation in a single quantum dot*, Phys. Rev. B **61**, R10579 (2000)

[139] M. Bayer, O. Stern, P. Hawrylak, S. Fafard, and A. Forchel, *Hidden symmetries in the energy levels of excitonic 'artificial atoms'*, Nature **405**, 923 (2000)

[140] A. Kiraz, M. Atatüre, and A. Imamoğlu, *Quantum-dot single-photon sources: Prospects for applications in linear optics quantum-information processing*, Phys. Rev. A **69**, 032305 (2004)

[141] A. Muller, E. B. Flagg, P. Bianucci, X. Wang, D. G. Deppe, W. Ma, J. Zhang, G. J. Salamo, M. Xiao, and C. K. Shih, *Resonance Fluorescence from a Coherently Driven Semiconductor Quantum Dot in a Cavity*, Phys. Rev. Lett. **99**, 187402 (2007)

[142] A. Faraon, A. Majumdar, H. Kim, P. Petroff, and J. Vučković, *Fast Electrical Control of a Quantum Dot Strongly Coupled to a Photonic-Crystal Cavity*, Phys. Rev. Lett. **104**, 047402 (2010)

[143] S. Michaelis de Vasconcellos, S. Gordon, M. Bichler, T. Meier, and A. Zrenner, *Coherent control of a single exciton qubit by optoelectronic manipulation*, Nature Photon. **4**, 548 (2010)

[144] M. Shirane, S. Kono, J. Ushida, S. Ohkouchi, N. Ikeda, Y. Sugimoto, and A. Tomita, *Mode identification of high-quality-factor single-defect nanocavities in quantum dot-embedded photonic crystals*, J. Appl. Phys. **101**, 073107 (2007)

[145] A. Imamoğlu, S. Fält, J. Dreiser, G. Fernandez, M. Atatüre, K. Hennessy, A. Badolato, and D. Gerace, *Coupling quantum dot spins to a photonic crystal nanocavity*, J. Appl. Phys. **101**, 081602 (2007)

Acknowledgements

I would like to express my gratitude to those people who made this thesis possible. First of all, I would like to gratefully acknowledge my supervisor, Prof. Dr. Artur Zrenner, for his friendly guidance and continuous support throughout my thesis work.

I would also like to thank all the members of our group for fruitful scientific discussion: Wadim Quiring, Simon Gordon, Dirk Mantei, Yves Alexander Leier, Konstantin Weißgerber, Janina Woitkowski, Dr. Steffen Michaelis de Vasconcellos, Dr. Gerhard Berth, Dr. Volker Wiedemeier, Dr. Thomas Hangleiter, Klaus-Peter Hüsch, and Peter Olenburger. Thanks to Reiner Schneider, Rüdiger Schulte, Janik Mühe, and Daria Wilke for their technical support.

Furthermore, I would like to thank the group of Prof. Dr. Cedrik Meier for using their RIE-ICP machine and SEM. I am grateful to Prof. Dirk Reuter for providing the QD samples. Also, I thank the group of Prof. Dr. Torsten Meier and Dr. Jens Förstner, espicially Dr. Stefan Declair, for the helpful theoretical discussion.

I acknowledge the financial support of the German Research Foundation (DFG) via the Research Training Group GRK 1464 M*icro- and nanostructures in optoelectronics and photonics*.

Finally, I would express a deep sense of gratitude to my parents and siblings for their support and encouragement over the years. Also, I appreciate the encouragement and the patience of my wife during my PhD work.